POLITECNICO DI TORINO

Master's degree course in Aerospace Engineering
Academic Year 2022/2023
Graduation Session December

Study and Analysis of a Nanosatellite Configuration

Supervisor: **Defended by:**
Prof. Sabrina Corpino   Luca Bartolucci

I

Abstract

The work of this thesis concerns the development of the structural subsystem and the realization of the internal configuration of the SPEISAT spacecraft, developed as part of the Spei Satelles mission, carried out by a team of Politecnico di Torino for the Italian Space Agency, on behalf of Vatican City.

Such task has been conducted in a time span of 4 months through an iterative process based on the concurrent engineering philosophy, with the goal of achieving the realization of a shell capable of housing the different subsystems while withstanding the loads caused by the launch and the harsh conditions of the space environment.
After the identification of the design drivers and the applicable documents, it has been possible to determine the requirements that would have led to the design of the structure and the internal configuration. The work has been carried out in the *Solidworks* environment through a series of iterations defined by the various inputs received by the different subsystems' groups regarding their area of expertise. With the approaching of the conclusion of the design phase, a validation of the model has been performed, and here presented, through Finite Element Analysis in the *MSC Apex* and *MSC Patran* environment using the *MSC Nastran* solver.

Subsequently, the Assembly, Integration, Verification and Test (AIV&T) activities have been carried out, in parallel with the finalization of minor configuration aspects, such as the refinement of the cable management.
The major tasks have lastly reached a conclusion with the environmental tests. In the matter of this thesis the results derived from the random vibration test are analysed, also to assess the validity of the Finite Element Model used for the analysis.

Finally, an assessment of the configuration is provided through the review of the AIV&T activity, as well as thanks to the telemetries correctly sent by the spacecraft, launched on June 12th 2023. The latter, in particular, allowed to determine whether the adopted configuration choices have proven to be effective, specifically regarding the thermal aspects.

In conclusion, it can be said that the structural design and the configuration layout developed for SPEISAT have proven to be satisfactory, as all requirements are met and the satellite is executing its intended mission as expected.

Table of Contents

List of Figures

4

List of Tables

List of Acronyms

ACS	Attitude Control System
ADCS	Attitude and Determination Control System
AIV&T	Assembly Integration Verification & Testing
ARI	Associazione Radioamatori Italiani
ASD	Acceleration Spectral Density
ASI	Agenzia Spaziale Italiana
AVUM	Attitude & Vernier Upper Module
C&DH	Command & Data Handling
CDS	CubeSat Design Specification
CFRP	Carbon Fiber Reinforced Polymer
CNR	Consiglio Nazionale della Ricerca
CoG	Centre of Gravity
COTS	Commercial Off The Shelf
CVCM	Collected Volatile Condensable Materials
DET	Direct Energy Transfer
DMM	Dummy Mass Model
DOF	Degree Of Freedom
ESA	European Space Agency
FEA	Finite Element Analysis
FEM	Finite Element Method
ICD	Interface Control Document
IMU	Inertia Measurement Unit
IPA	IsoPropyl Alcohol
LEO	Low Earth Orbit
LV	Launch Vehicle
MEW	Modal Effective Weight
MLI	Multi-Layer Insulator
MPC	Multi Point Constraint
PFM	Proto Flight Model

PTFE	Polytetrafluoroethylene
RML	Recovered Mass Loss
RSS	Root Sum Squared
SPC	Single Point Constraint
SSO	Sun Synchronous Orbit
TEMF	Total Effective Mass Fraction
TML	Total Mass Loss
UHF	Ultra-High Frequency

List of Symbols

X	Displacement
K	Stiffness
F	Load
ζ	Damping ratio
Ω	Base vibration frequency
ω_n	Natural angular frequency
[I]	Identity matrix
φ	Mode shape
ξ	Modal displacement
C	Damping
f_n	Natural frequency
H	Transfer function
E	Elastic modulus
G	Shear modulus
v	Poisson ratio
ρ	Density

1 Introduction

The following chapter serves as an introduction to the CubeSat standard and the SPEI SATELLES mission itself, as well as to present the thesis outline.

1.1 The CubeSat standard

The CubeSat is a nanosatellite class introduced in 1999 by professor Jordi Puig-Suari of California Polytechnic State University and professor Bob Twiggs of Stanford University Space Systems Development Laboratory. Their goal was to produce a spacecraft standard to support and facilitate the study of small satellites intended for the LEO to serve as a platform for testing new space technologies and to perform scientific research.

To achieve such a result, it was defined a new standard based on fixed sizes and form factors. The CubeSats are founded on the concept of unit 'U': as per the *CubeSat Design Specification* [1] the single unit shall have a maximum dimension of 100x100x113.5 mm with a maximum mass of 2 kg.
Starting from it, it's possible to use this standard "block" to increment the size of the spacecraft, reaching higher form factors, such as the 6U or the 12U, most recently used in the majority of space missions conducted by companies.
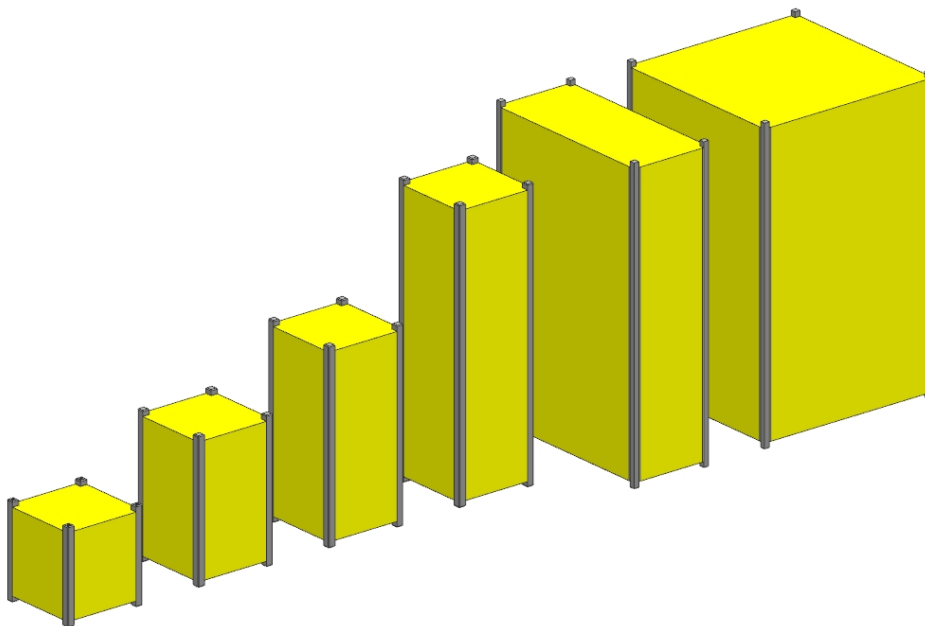
Figure 1.1 The CubeSat family form factor

Thanks to this standardization, it's been possible to reduce the costs of spacecraft development, also due to the possibility of acquiring the subsystems components as COTS products.
Moreover, the fixed form factors led to the development of standardized deployer design specifically for CubeSats, allowing further reduction of the launch costs, a minimization of

flight issues and an easier accommodation of the spacecraft inside the launcher, as the satellite manufacturer didn't need to take in account the mechanical interface with the vector itself anymore.

Given such premises it's safe to assume that in the early 2000s, when the first CubeSats started to be launched, they were mainly developed in an academic environment by universities. In was only half a decade later that the potential of CubeSats was noticed by both government agencies and commercial groups that began to take interests in these nanosatellites for technological development and scientific applications.

Finally, from the start of the 10s, there has been an exponential increase in the number of CubeSats launched, which started to be exploited for remote sensing thanks to further development in the field [2].
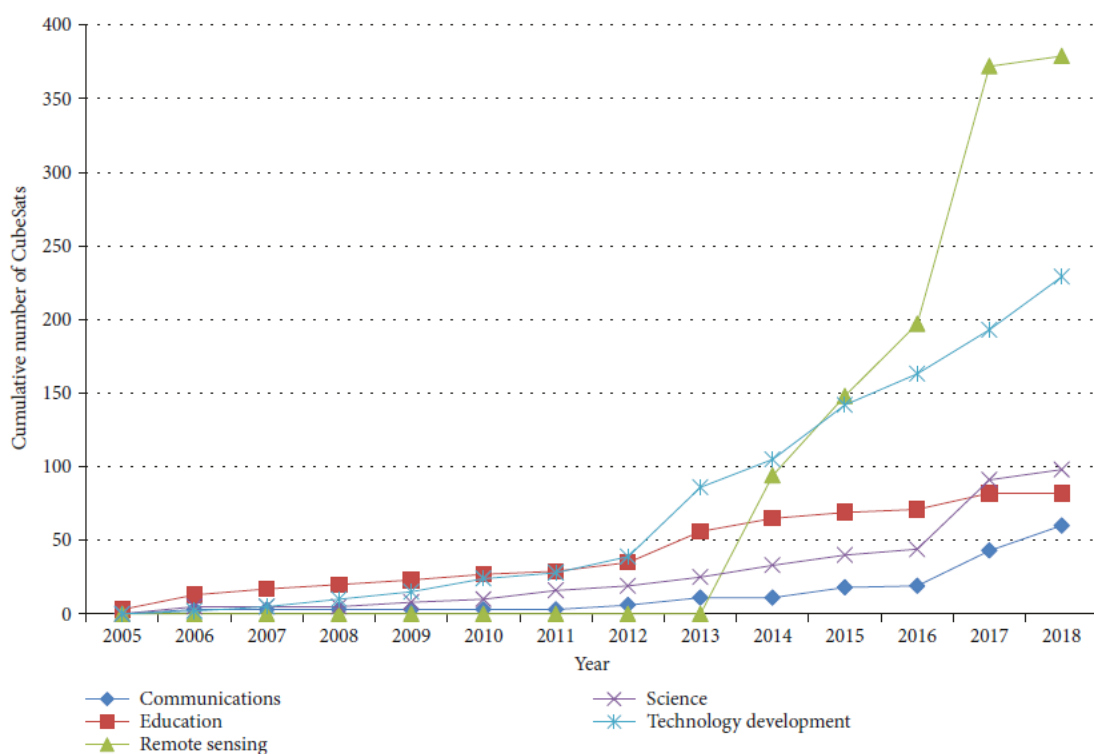
Figure 1.2 Number of CubeSats launched in the years, credits: [2]

Taking ESA as an example, nowadays CubeSat can be used for a wide range of application [3]:

- Driving the miniaturization of systems and new approaches to subsystems packaging and integration.
- Affordable demonstrator for new technologies and techniques such as formation flying, proximity operations or rendezvous and docking.
- Carry-out multiple in-situ measurement.
- Deploy small payloads whose number would compensate for the lower performances, for examples thanks to the usage of a constellation.
- Solar system exploration.

1.2 The Spei Satelles Mission

Spei Satelles (literally "Guardian of Hope") is a space mission coordinated by ASI and promoted by the Dicastery for Communication on behalf of Vatican City. It was created from the will to diffuse a message of hope from Pope Francis to all the people in the world.

This message, also known as *Statio Orbis*, was first shared March 27th 2020 during the Covid pandemic and was transcribed in a Nano-book, realized by the Institute of Photonics and Nanotechnology of the CNR, in binary language, with 1 and 0 respectively represented by a hole and an empty space.
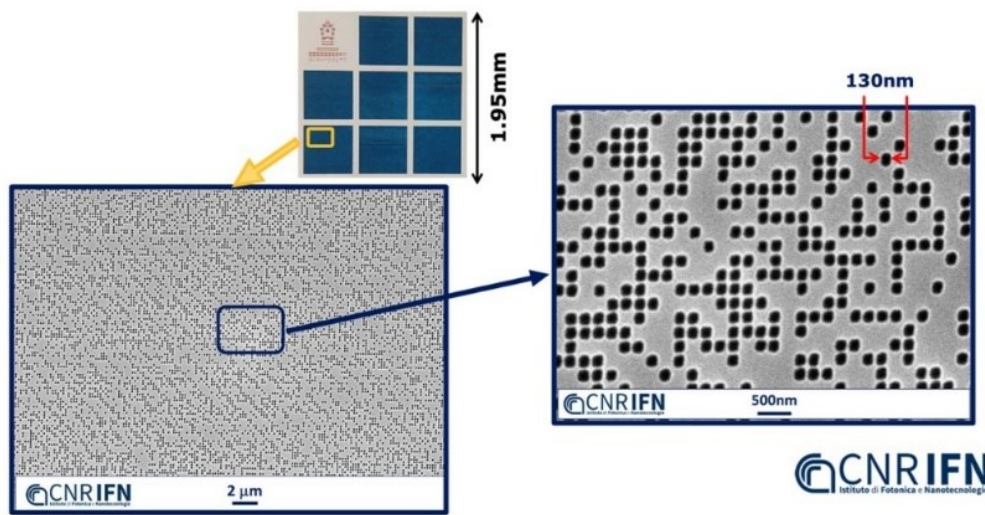
Figure 1.3 The Nano-book, credits: CNR IFN [4]

To carry this payload in orbit, to Politecnico di Torino was commissioned the development of a spacecraft a 3U CubeSat later named SPEISAT, capable of accomplishing such task.

Furthermore, the satellite was also required to transmit certain phrases, decided in accordance with Vatican City, on the amatorial UHF radiofrequency of 437.7 MHz so that the radioamateur all around the globe could receive the transmission. Given such premises the Spei Satelles mission can be categorized as a telecommunication one.

Finally, it was decided to develop in-house a sensing suite as secondary payload, capable of storing telemetry data and provide a wide set of information usable to characterize the orbit, as well as to assess the correctness of the analyses conducted in both the attitude and thermal aspects.

The development of such board is discussed in the master thesis of its developer, Simone Bollattino [5].

Figure 1.4 Spei Satelles mission logo

To sum up, the Spei Satelles mission has 5 objectives which can be divided in primary and secondary.

Primary mission objectives:

1. Host the Nano-book and safely bring it to LEO.
2. Transmit text messages to ground stations on an amateur radiofrequency in three different languages: Italian, English and Spanish.

Secondary mission objectives:

3. Characterize the internal and external thermal environment of the spacecraft.
4. Characterize the angular motion of the spacecraft.
5. Characterize the internal magnetic field of the spacecraft and Earth magnetic field.

The launch of SPEISAT took place on the 12th of June 2023 from the Vandenberg Space Force Base in California with the SpaceX Transporter-8 mission on board a Falcon 9. The spacecraft was placed inside an Astrofein deployer located on an ION Mk-II, provided by D-Orbit, which was released by the launcher in a SSO at an altitude of 525 km. SPEISAT was correctly deployed on the 23rd of June and it began its mission.

Figure 1.5 SpaceX Transporter-8 Falcon 9 launch, credits: SpaceX

With the launch of SPEISAT the Politecnico di Torino reaches the extraordinary amount of three spacecrafts launched. As a matter of fact, it has a great heritage in development of CubeSats, thanks to the e-st@r (Educational SaTellite @ Politecnico di toRino) family made of 2 satellites, e-st@r-I [6] and e-st@r-II [7], respectively launched in 2012 and 2016.

1.3 Thesis outline

This thesis focuses on the structural subsystem and the internal configuration of the spacecraft, from its early design to the environmental tests and the analysis of in-orbit data. As such, the following chapters will be presented:

- **Structure and FEA**: in this chapter the state-of-the-art of the structural subsystem will be discussed in terms of components and materials. Moreover, the validation model used in the project will be introduced, providing an overview of the FEM and the analyses later conducted to make an assessment the structure.
- **Design process**: it illustrates the design process followed. Firstly, the design drivers will be identified and used together with the applicable documents to present the system requirements for the areas of interest.
  Secondly, the DMM will be introduced as to discuss the first concept of the spacecraft, to later move on to the PFM. An overview of the system architecture will be provided to allow a better understanding of the complexity of the spacecraft and to introduce the design phase. This was conducted mainly in the *Solidworks* environment obtaining a CAD model used as a base of discussion for the later design of the internal configuration. As it will be explained the main challenge of this mission was the short amount of time, therefore an iterative process has been applied and its main iterations will be analysed here, discussing the problems faced during the development phase and solved through a variation of the structure and/or the general configuration of the spacecraft.
  Moreover, the harness aspect of the design will be presented and analysed, especially the wiring matter. This will conclude the design phase allowing the introduction of the surface treatments to which the structure has been subjected.
  Finally, the mass and volume budget will be presented, providing an insight of the physical properties of the spacecraft at the time of launch.
- **Structural Analyses**: This chapter focuses on the FEA conducted the model realized in the design process. These procedure followed can be divided in three main steps carried out in two different software:
  - ○ **Pre-processing**: this phase was conducted in the *MSC Apex* environment in its early stages to be later concluded in the *MSC Patran* one.
  - ○ **Solver**: the solving phase was entrusted to *MSC Nastran.*
  - ○ **Post processing**: the evaluation of results was conducted in *MSC Patran* or through the analysis of the files produced in the solving phase.
- **Environmental testing**: In this chapter the environmental tests will be presented, in particular the vibrational ones. These will serve both as a validation of the model

realized and as to test the spacecraft itself to the launch loads. Specifically, a comparison between the two sets of results will be presented and the possible differences will be discussed and explained.

- **Conclusion**: To evaluate the quality of the work done, an AIV&T activity will be discussed as to provide support to the design choices and to verify some of the requirements. Moreover, some in-orbit data will be presented to assess the status of the spacecraft and the effectiveness of the internal configuration.

2 Structure and FEM

2.1 The structural subsystem

The spacecraft structure serves as the host of the different spacecraft subsystems and has the role of withstanding the launch loads, protecting and bringing the internal components in orbit safely.

Moreover, it needs to be able to provide a discrete high degree of protection to the subsystems from the harsh space environment. This becomes especially relevant in the matter of radiations and extreme temperatures, both extremely dangerous for electrical components which could deteriorate and worsen their performance.

Sometimes the structure subsystem is grouped together with the mechanism one, especially in missions where there is a high degree of mobility of components, such as deployable solar panels or pointing antennas. In the SPEISAT case this didn't happen as the only mechanism present is the antenna deployment one, provided by *Tyvak International*, therefore the only aspect analysed in such subject is the mechanical interference between the structure and the deployed antenna.

The structural subsystem of a CubeSat is generally composed by the same elements which can be customized according to the mission objective.

The state-of-the-art is currently founded on a main frame, presenting several lightening to decrease the spacecraft mass, which generally incorporates the rails and their standoffs. The former are elements located on the longitudinal edges of each vertical face which end with their standoffs. These are protrusions located on the transversal faces and serve as points of support for the spacecraft when inserted in the deployer, as well as to maintain it in a fixed position. Moreover, the rails standoffs host the deployment switches, used to ensure that the CubeSat is inactive during the prelaunch activities, keeping the circuit open thanks to the pressure applied on them. After the deployment the switches open and the circuit is closed, booting the spacecraft.

As a matter of fact, the deployer is constituted by a spring mounted below a panel on which the CubeSat is positioned. Once the spring is compressed, the deployer lid is closed, with the spacecraft ready to be deployed.

This obviously leads to correctly assume that the spacecraft is launched in outer space uncontrolled. In this situation the ACS or ADCS plays its role in detumbling the satellite damping its angular velocity and stabilizing it.

17

Figure 2.1 CubeSat deployer: credits ISISPACE

Inside the deployer the only points of contact with the satellite correspond with the rails and rails standoffs. The latter, in particular, serve as constraints, preventing the CubeSat from oscillating or moving in any way. On the other hand, the rails are important especially during the deployment phase, as they need to guarantee surface roughness below a certain level (1.6 μm [1]) to allow the correct spacecraft sliding outside the deployer.
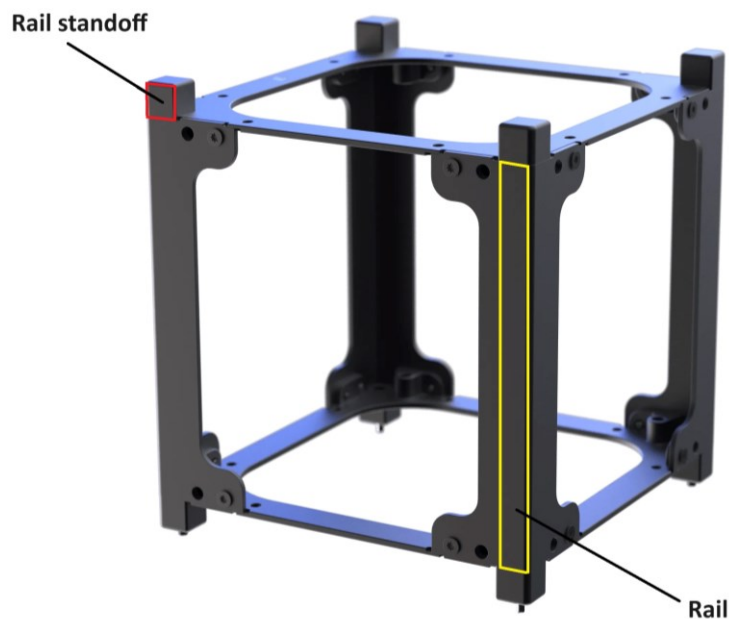
Figure 2.2 CubeSat main frame, credits: Endurosat

Inside the frame it's necessary to provide supports for the different spacecraft subsystem, especially when working with CubeSats with higher form factors, such as 3U, 6U or 12U. This is done through cross-members, transversal structural components which serve as a place on which it's possible to place various components. Moreover, it grants a discrete increase in the structure stiffness, even though such task can be assigned to another type of structural element called stiffener. This is usually a robust bar of aluminium which prevents the bending of the structure due to the launch loads and vibration environment.

However, recently there has been an increasing number of cases in which the stiffeners have been readapted to serve as a support for components, further lightening the structure and simplifying the design.

Figure 2.3 Example of stiffeners used as support elements, credits: Sputnix

As it can be seen, in the CubeSat standard this subsystem has always been subject only to minor changes due to the fixed sizes and form factors. This stagnation led to the commercialization of modular spacecraft structures, almost a mass production [8], characterized by a high number of inserts form cross-members. In such a way, according to the spacecraft architecture, it's possible to divide the internal space of the spacecraft into several bays in which it is possible to accommodate the subsystems separately, providing for each one of them a dedicated support.

Figure 2.4 1U, 2U, 3U, 6U CubeSat structures, credits: AAC Clyde Space

19

Having a structure characterized by such a degree of freedom, due to the possibility of changing the location of the cross-members, is a great advantage as it allows to bring slight, or not, changes to the configuration, according to the necessities. For example, due to a thermal problem it may be necessary to put in contact two components, allowing thermal conduction. A modular structure simplifies the solution making necessary to move only one component, without the usage of thermal straps, heaters, MLI or heat sinks, thus simplifying the system as well.

2.1.1   Materials

One of the major advantages of CubeSats is the relatively low costs of production, making them accessible to the academic world. Therefore, to prevent further rise of the costs and a more complicated development when it's not required, the tendency is to use materials already widely used. In this section the most common will be presented and compared.

Historically, the tendency has always been to develop the structure using aluminium alloy, in particular Al 5052, 6061 and 7075. This is due to the excellent properties of this material as it is strong and lightweight, while being relatively cheap.
On the other hand, only recently there has been a growing interest in the possibility of developing composite structures. For the matter of this thesis it's has been selected a composite realized with CFRP or Aluminium-(Silicon-Carbide) (Al-SiC).

The following table compares the materials previously cited providing an overview regarding the mechanical properties deemed as fundamental to assess whether a material is fit to be used to produce a spacecraft structure.

Property	Al-5052	Al-6061	Al-7075	Al(6061)-25%SiC
Density kg/m³	2.67e3 – 2.7e3	2.69e3 – 2.73e3	2.78e3 – 2.81e3	2.87e3 – 2.89e3
Young's module [GPa]	70 – 73.6	66.6 – 70	71 – 74.6	110 – 115
Poisson's ratio	0.33 – 0.343	0.325 – 0.335	0.33 – 0.343	0.3 – 0.35
Maximum yield strength [MPa]	66 – 72.9	241 – 281	345 – 496	390 – 400
Minimum operative temperature [°C]	-273	-273	-273	-273
Maximum operative temperature [°C]	150 – 170	130 – 150	80 – 100	262 – 277
Thermal conductivity [W/m.°C]	139 – 150	161 – 174	132 – 142	165 – 170
Specific heat [J/kg.°C]	963 – 1e3	934 – 972	913 – 950	860 – 890
Thermal expansion coefficient [μstrain/°C]	23.7 – 24.9	23.4 – 24.6	22.9 – 24.1	15 – 16.5
Price [EUR/kg]	1.66 – 1.86	1.66 – 1.86	3.32 – 3.71	177 – 300

Table 2.1 Materials comparison

The properties can be further analysed in a more simplified and clear way, using graphs, as done below.
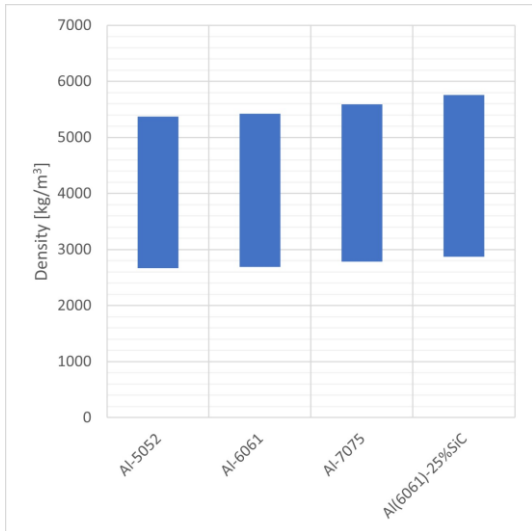
Figure 2.5 Materials' density comparison
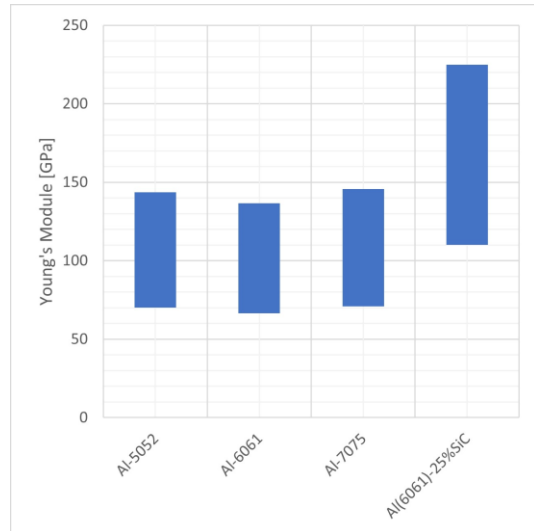
Figure 2.6 Materials' Young's module comparison
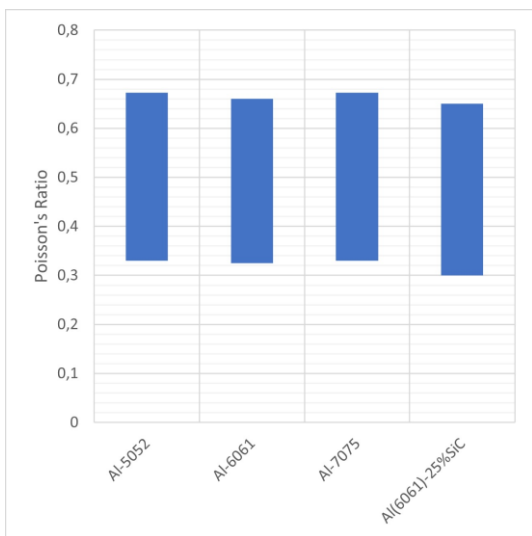
Figure 2.7 Materials' Poisson's ratio comparison
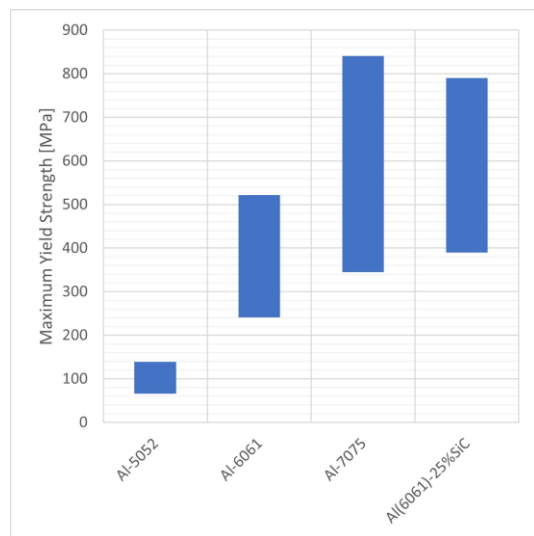
Figure 2.8 Materials' maximum yield strength comparison
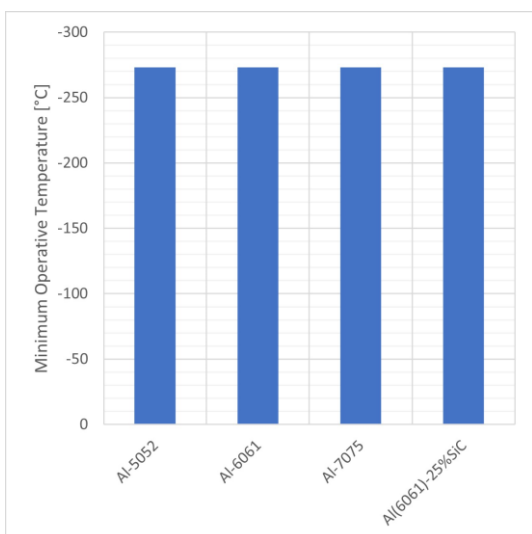
Figure 2.9 Materials' minimum operative temperature comparison
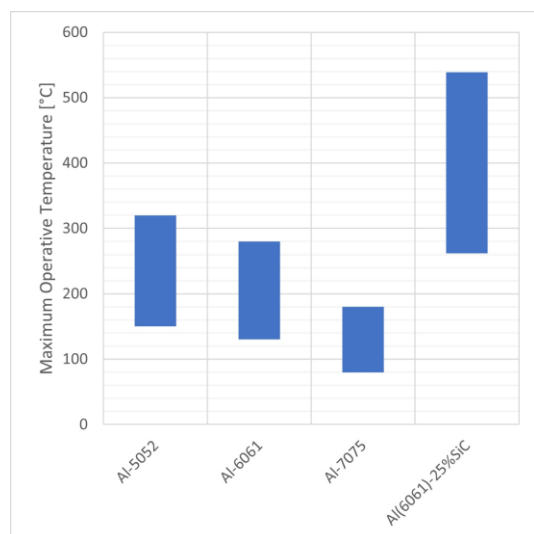
Figure 2.10 Materials' maximum operative temperature comparison

22
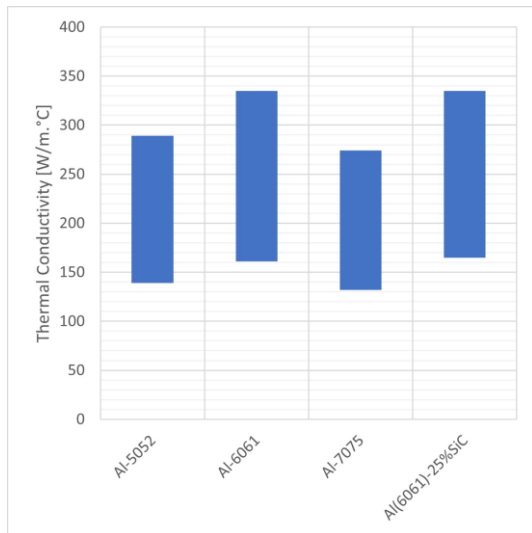
Figure 2.11 Materials' thermal conductivity comparison
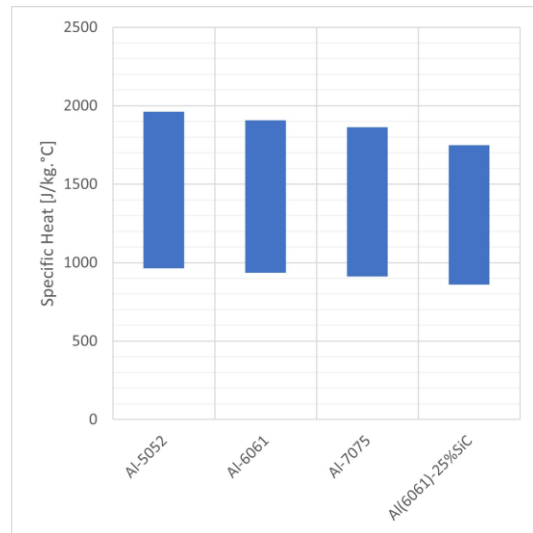
Figure 2.12 Materials' specific heat comparison
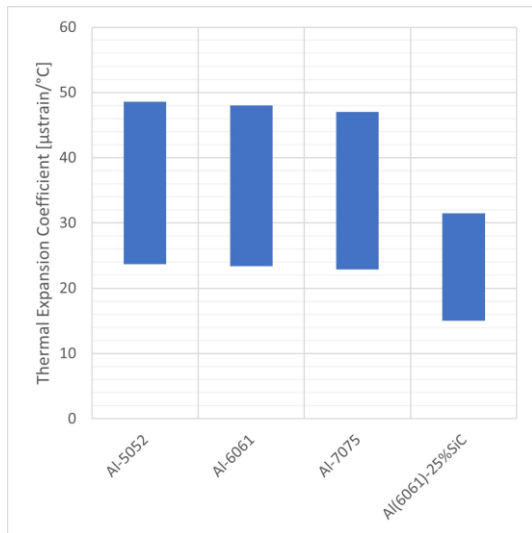
Figure 2.13 Materials' thermal expansion coefficient comparison
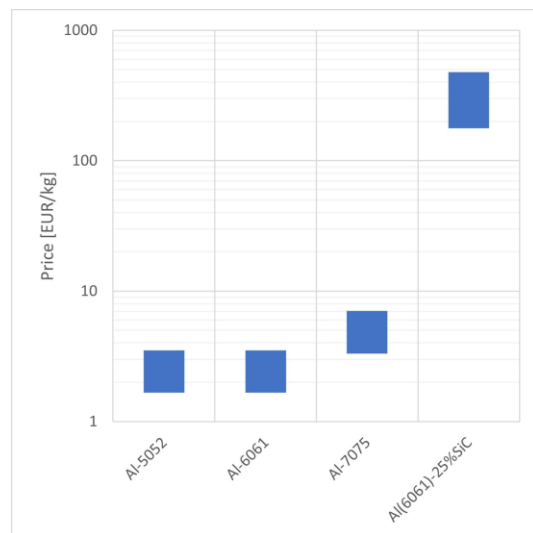
Figure 2.14 Materials' price comparison

As it can be seen from the pictures above the three aluminium perform relatively similar in many aspects, besides the maximum yield strength in which the Al-5052 presents much lower values than the others, as shown in Figure 2.8.

Regarding the Al-7075 alloy, this one performs in a similar way to the Al-6061 one, however it offers higher maximum yield strength, combined with a better manufacturability. On the other hand its density is slightly greater than the Al-6061 counterpart, aspect that can be fundamental in a space mission. This aspect is however counterbalanced by the better mechanical properties which can allow to obtain the same result with thinner components, determining a gain in the free space inside the spacecraft. It's also stiffer, aspect fundamental in applications where structural stability and vibration resistance play a vital role. Finally, on the thermal subject, the Al-7075 alloy generally performs better than the Al-6061 counterpart, however, this aspect needs to be assessed after the mission definition, as in some cases, for example, may be required a structure characterized by a higher degree of insulation, while in others it's important to guarantee thermal conduction.

Finally the Al-SiC composite offers mechanical properties on par with the aluminium alloys, sometimes even exceeding them by far, for example in the stiffness, as shown in Figure 2.6. On the other hand, the prohibitive price makes it unaffordable in many cases (it needs to be noticed that Figure 2.14 has the Y axis in logarithmic scale), especially with CubeSats missions where the costs tend to be contained in several cases. Moreover, it doesn't offer the same machinability of the other materials, therefore, beside the costs for the material itself, higher expenses for the components production need to be considered.

Due to the several advantages of the Al-7075, this is by far the most commonly used in the space sector. In particular, it was also the material deemed to be the best to produce the structure for SPEISAT.

2.2 Finite Element Method

2.2.1 Overview

Each design needs to be analysed and validated before moving to the production phase, in the structural subsystem this is done through FEA.

These analyses are based on a Finite Element Model. This is a mathematical model constituted of nodes and elements which can be scalar (0D), 1D, 2D and 3D. The last two are the most complex as they can be realized in different shapes.
Generally, the main guideline to choosing the correct element is to identify the desired goal and how to reach it, as in many cases the same problem can be solved in many ways, characterized by a different degree of complexity. As it may be expected, the objective of the model is to be as representative as possible of reality, therefore, in most cases, finer results are obtained only by increasing the depth of the method.

Moreover, it's possible to identify general and connector elements. The former is characterized by an arbitrary number of connection points while the latter is used to serve as a connection between points or elements satisfying the condition of rigid body. This was introduced to solve problems which may appear when working with spring, bars, rigid elements, or multipoint constraints.

The creation of elements allows the allocation of their properties, used to characterize the physical attributes of the system studied, through the definition of materials, which have to be separately created, orientation etc…
The following table serves to provide an overview regarding the main elements used and their properties [9].

Dimensions	Name	Description
1D	**CROD**	It's the simplest of the 1D elements, presenting only axial and torsional stiffness. Therefore, it is mainly used when the load applied is either a tension/compression or a torsion.
	CBAR	This element offers a wider set of applications than the CROD one as bending and transverse shear stiffness can be defined in the two perpendicular directions to the CBAR axial direction. Such capability, however, is limited by the fact that the properties cannot change along the element length. Moreover, unlike the previous element, it offers the possibility to define the section shape. Lastly, the ends of the CBAR element can be offset from the points. This means that even though it has been defined providing a set of geometrical elements as an input for its definition, in the mathematical level this may be not happen, as it could end before reaching such point.
	CBEAM	The CBEAM element offers all the capabilities of the CBAR one adding several new functionalities such as the possibility of defining different cross-sectional properties along the length of the beam or the fact the neutral axis (axis in the cross-section which doesn't present longitudinal stresses) and the shear centre (point in the cross-section to which shear loads can be applied without causing torsion in the section) don't need to be coincident. Moreover, if offers the possibility to define distributed torsional mass moment of inertia, particularly useful for dynamic analyses.
2D	**CSHELL (CQUAD/CTRIA)**	These elements can be divided into two groups, defined by the number of points which compose them: CQUAD and CTRIA. The former element can be defined as CQUAD4 or CQUAD8, while the latter as CTRIA3 or CTRIA6. Those characterized by the lower number of the two need a number of nodes equal to the number of the vertexes to be defined. The remaining present mid-side nodes and curved edges. Therefore, this allows more accurate simulations of curved shell applications without requiring a higher number of degrees of freedom. On the other hand, they are more difficult to mesh when working with irregular shapes. This element allows to obtain virtually any plate configuration through the definition of the right properties. It's possible to include up to 4 material properties: • MID1: membrane material property. • MID2: bending material property. • MID3: transverse shear stiffness material property.

		• MID4: property used to define coupling between the membrane and the bending deformation. Given such premise it's possible to imagine that this element can withstand any type of load, both out and in-plane.
	CSHEAR	Differently from the previous element, the shear panel is used where the bending stiffness and axial membrane stiffness of the plate is negligible. This allows to deduce that this type of element is capable of withstanding only in-plane loads, therefore is mainly implemented to simulate thin skin panels.
3D	**CHEXA**	The CHEXA element is the most commonly used element when working with solids. It's defined through 8 corner nodes and up to 12 optional mid-side ones. This element contains stiffness only in the translation degree of freedom at each point. Alternatives of this element are the CPENTA (wedge element with 5 faces), CPYRAM (pyramid element with 4 faces) and CETRA (tetrahedral element with 4 faces).

Table 2.2 NASTRAN elements

It needs to be noted that the relationship between elements may generate singularities, causing defects in the analysis phase. In example, the CSHELL element is connected only to 5 out of the 6 degrees of freedom. This may cause absence of stiffness, for example the one about the rotational degrees of freedom about the surface normal, in certain cases. This causes. This is caused by the creation of a singular stiffness matrix, making the job fail.

The Finite Element Model can be created with two different approaches:

1. From scratch: In this case there isn't a base from which it's possible to start. Using pre-processing software, such as *MSC Patran*, *MSC Apex* or *Ansys Workbench*, it's possible to create a geometry, to which will be applied a mesh allowing the definition of the elements' properties. Obviously, the mesh can be both 2D and 3D, based on the desired elements.
2. From an external file: In this case the pre-processing software imports an external file, created on another software, which may be *Solidworks*, and it's necessary to only generate the mesh, as well as define the boundary conditions. It's generally easier than the previous one as in most cases it's simpler to develop accurate geometrical model in software specialized in such task. As mentioned before, this is the approach used in the SPEISAT case.

At this stage only the properties of the model itself have been discussed; to complete the overview over the FEM it's necessary to define boundary conditions as well. In particular loads and constraints will be now analysed.

The former can be classified in three different categories:

1. Nodal: The load is applied only to a single entity, which can be both a geometrical and a mathematical one. The former being a point or a vertex, a curve or an edge, a surface or a face, or a solid, while the latter only a node. In the first case the load is distributed equally on all the nodes forming the element.
2. Element uniform: the load is applied uniformly to the whole element. This kind of load might be a distributed, inertial, or total one or a pressure. Obviously, the element can be both 1D and 2D.
3. Element variable: these are the same as the previous class with the only difference being that they vary across the element.

Moving on to the constraints, these can be divided in two main groups:

1. SPC: this is applied to a single degree of freedom, obviously multiple SPC can be applied to the same point binding an equivalent number of DOFs. Moreover, this can be used to enforce displacement at nodes. This can be particularly useful when the model is subjected to a fixed displacement and it's necessary to account the entity of the stress generated.
2. MPC: this type of constraint is used to describe a relationship between two or more degrees of freedom. In the case of a linear problem, it can be simplified as

$$\sum_j R_j u_j = 0 \qquad\qquad [\,1\,]$$

where u_j represents any degree of freedom and R_j a scale factor.
They require to work with multiple nodes which are classified as "master" and "slave". According to the relationship between these classes and the number of nodes which belong to them, it's possible to further classify this type of constraint.
- RBE2: This is characterized by a single "master" independent node and multiple "slave" dependent ones. It's mainly used to simulate a rigid connection.
- RBE3: Unlike the previous one, this uses a single dependent node and multiple independent ones. It's generally used to distribute loads and mass, without adding stiffness to the structure. The distribution happens according to a weight factor dependent on the distance of the "master" nodes from the slave one.
- RBAR: It works by creating a rigid bar between two nodes, or group of nodes, allowing the definition of up to two independent and two dependent terms, obviously the dependent and independent ones need to coincide. It permits any combination of the degrees of freedom defined in independent terms as long as their number adds up to six.

2.2.2 Typical analyses

In the space field are particularly relevant dynamic analyses as a spacecraft, to reach the orbit, needs to face the harsh launch environment, characterized by violent vibrations. As a way to prevent damages inside the fairings, launch company often require customers to provide

analyses relate to the natural frequencies and the spacecraft responses to the vibrational tests. Nonetheless, simple static analyses can provide an insight regarding the stresses which can manifest due to the launch loads.

2.2.2.1 Static analysis

In the launch environment the loads can reach particularly high values. Regarding the (quasi) static one, they are mostly due to the launcher acceleration, therefore generating inertia loads, expressed as compressive, tensional and lateral. As an example, Table 2.3 sums up the launch load of the Vega launch system [10].

Load Event		QSL (g) (+ = tension; - = compression)		
		Longitudinal		Lateral
		Compression	Tension	
1	Lift-off phase	-4.5	+3.0	±0.9
2	Flight with maximum dynamic pressure	-3.0	N/A	±0.9
3	1st stage flight with maximal acceleration and tail off	-5.0	N/A	±0.7
4	2nd stage ignition and flight, 3rd stage ignition	-5.0	+3.0	±0.7
5	3rd stage maximal acceleration	-7.0 + M[1]/1000	N/A	±0.2
6	AVUM flight	-1.0	+0.5	±0.7

Table 2.3 Vega launch loads, credits: Arianespace

Given these loads, the analyses goal is to determine the entity of the stresses and deformation which are generated during the launch phase.

Having defined a physical system through a mathematical model, the solver will process the problem solving the matrix operation

$$[K_{gg}]\{x_g\} = \{F_g\} \qquad [\,2\,]$$

where "g" represents the global displacement defined as the union of all the local displacement components at all of the nodes. This allows the definition of a set whose displacement is represented by $\{x_g\}$. $[K_{gg}]$ and $\{F_g\}$ respectively indicate the stiffness matrix and the load, whether explicit (force, pressure) or implicit (inertial load). The matrix is defined by assembling all the stiffness matrices for all the elements, assigned through the properties. Similarly, the load vector is created through the combination of all the explicit and implicit loads.

The two vectors have a dimension equal to the number of DOFs while the matrix is real and symmetric, but often singular. This causes the equation to not be solvable, therefore it's required to obtain a reduced set of equations. This is done by identifying the unconstrained structural DOFs through the exclusion from the g-set the DOFs bound by MPCs and SPCs, thus

---

[1] M = mass of the spacecraft [kg]

obtaining the f-set.

This set is then subject to a further condensation, through the Guyan reduction, allowing to obtain the reduced set of equations which can be rewritten as

$$[K_{ll}]\{x_l\} = \{F_l\} \qquad [\,3\,]$$

solvable through gaussian reduction [11].

2.2.2.2 Modal analysis

This analysis is conducted to determine the natural frequency and the mode shapes of the structure and the system. Such information are then used to determine how the body will respond when subjected to dynamic loads.

The natural frequencies are those at which free ($F(t) = 0$) and non-damped systems ($\zeta = 0$) tend to vibrate when excited. When this occurs, there is a perfect equilibrium between elastic and inertial forces. They are connected to the mode shape which is the deformed shape of a structure when vibrates at one of the natural frequencies. Therefore, for each of them there is a characteristic shape. They are functions of the structure properties and boundary conditions and can be firstly approximated with an equivalent [mass − spring] system (note that as mentioned above the damping is supposed to be null) [12].
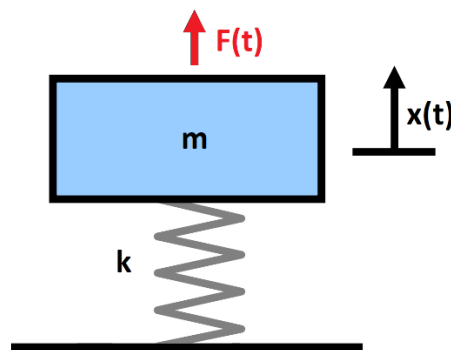
Figure 2.15 Mass-spring system

The equation of motion can be written as

$$m\ddot{x}(t) + kx(t) = F(t) \qquad [\,4\,]$$

with

$$x(t) = x_h(t) + x_p(t) \qquad [\,5\,]$$

$$x_h(t) = A\,sin(\omega t) + B\,cos(\omega t) \qquad [\,6\,]$$

Mixing equations [4] and [6] and setting $F(t) = 0$, it leads to

$$-mA\omega^2\,sin(\omega t) - mB\omega^2\,cos(\omega t) + kA\,sin(\omega t) + kB\,cos(\omega t) = 0 \qquad [\,7\,]$$

$$A(k - m\omega^2)\sin(\omega t) + B(k - \text{m}\omega^2)\cos(\omega t) = 0 \qquad\qquad [\,8\,]$$

$$\omega_n = \sqrt{\frac{k}{m}} \qquad\qquad [\,9\,]$$

Even though equation [9] may lead to thinking that the natural frequency[2] is a function of the intrinsic properties of the system, it actually depends on its state of equilibrium.

Modal analysis serves as an input for the vibration ones, aiming to determine whether resonance happens or not. This phenomenon occurs when a structure is stressed with an external load characterized by a frequency equal to the natural one. This causes an amplification of the response, which may lead to structural failures.

A way to analyse such phenomenon is through the introduction of the concept of Transmissibility Ratio. This can be described as the ratio between the maximum elastic force of the structure and the maximum applied force. Another way of expressing this term is by reducing the system [launcher – spacecraft] to a [mass – spring – damper] model, with two masses, one representing the spacecraft and the other launcher. In this case the TR can also be defined as the ratio to which is subjected the spacecraft over the launcher one. A more accurate formulation can be

$$TR = \frac{\sqrt{1 + \left(2\zeta\dfrac{\Omega}{\omega_n}\right)^2}}{\sqrt{\left(1 - \left(\dfrac{\Omega}{\omega_n}\right)^2\right)^2 + \left(2\zeta\dfrac{\Omega}{\omega_n}\right)^2}} \qquad\qquad [\,10\,]$$

A simple representation has been made in *Matlab* to show the effects of the resonance phenomenon with variable damping.

---

[2] ω_n is technically called natural angular frequency but it's more commonly used than f_n. Therefore, it's common practice to just call it "natural frequency".
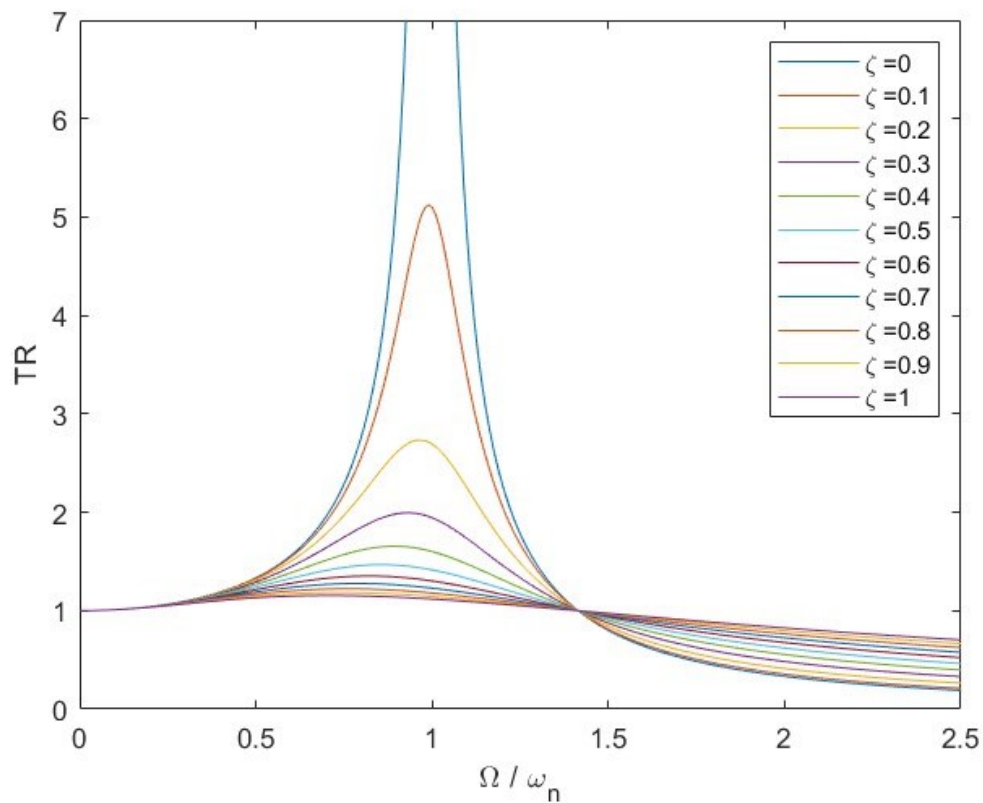
Figure 2.16 Resonance effects expressed through TR

As it can be seen with lower damping the value of the TR increases until its limit is $+\infty$ in the case where $\zeta = 0$.

With such premise, given the hypotheses that there are no damping or applied loads, the modal analysis is conducted by the resolution of the system expressed in matrix form as

$$[M]\{\ddot{x}\} + [K]\{x\} = 0 \qquad [\,11\,]$$

The homogeneous system of equation will have as solution a harmonic motion

$$\{x(t)\} = \{\phi\}e^{i\omega_n t} \qquad [\,12\,]$$

Therefore equation [11] can be rewritten as

$$-\lambda[M]\{\phi\}e^{i\omega_n t} + [K]\{\phi\}e^{i\omega_n t} = 0 \qquad [\,13\,]$$

$$([K] - \lambda[M])\{\phi\} = 0 \qquad [\,14\,]$$

Where $\lambda = (\omega_n)^2$. Equation [14] represents the classic eigenvalue problem

$$([A] - \lambda[I])\{\phi\} = 0 \qquad [\,15\,]$$

where $\{\phi\}$ is the eigenvector, or the mode shape.

From this, it's possible to define the physical displacement as a combination of all its normal modes as

$$\{u\} = \sum_i (\phi_i)\xi_i$$

[16]

Moreover, given that the matrices $[M]$ and $[K]$ are symmetric and real, they hold the following properties

$\{\phi_i\}^T[M]\{\phi_j\} = 0$	[17]	$\{\phi_i\}^T[K]\{\phi_j\} = 0$	[18]	If $i \neq j$
$\{\phi_i\}^T[M]\{\phi_j\} = m_i$	[19]	$\{\phi_i\}^T[K]\{\phi_j\} = k_i = \omega^2 m_i$	[20]	If $i = j$

Therefore, it's possible to define the ith generalized mass and stiffness, distinctive of each mode. While equations [17] and [18] guarantee the uniqueness of each mode thanks to their orthogonality property, equations [19] and [20] lead to the Rayleigh's equation, allowing a more accurate definition of natural frequencies.

$$\omega_i^2 = \frac{\{\phi_i\}^T[K]\{\phi_i\}}{\{\phi_i\}^T[M]\{\phi_i\}}$$

[21]

2.2.2.3 Random vibration analysis

The launch vibration environment is characterized by a non-deterministic motion; therefore, the future behaviour is impossible to determine. Unlike sinusoidal vibration, there is no known periodicity which makes it impossible to characterize the amplitude of the vibration as a function of time with a precise relationship.

Moreover, a peculiar characteristic of the random vibration is the possibility to excite many frequencies at the same time, while the sinusoidal counterpart, on the other hand, follows the typical profile. Therefore, the former allows to excite structural resonances of different components, characterized by different natural frequencies.
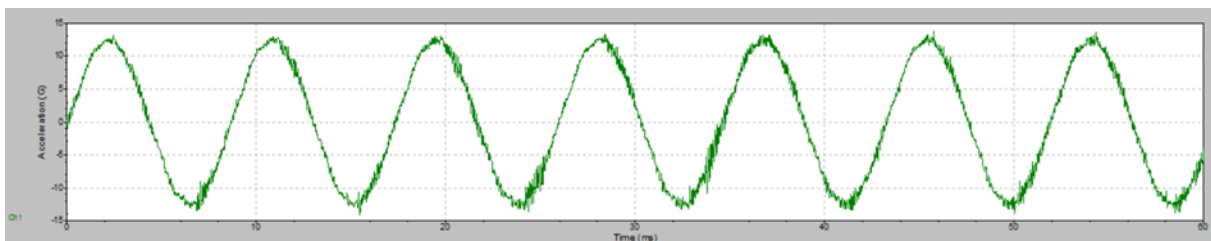
Figure 2.17 Sine vibration acceleration wavefront
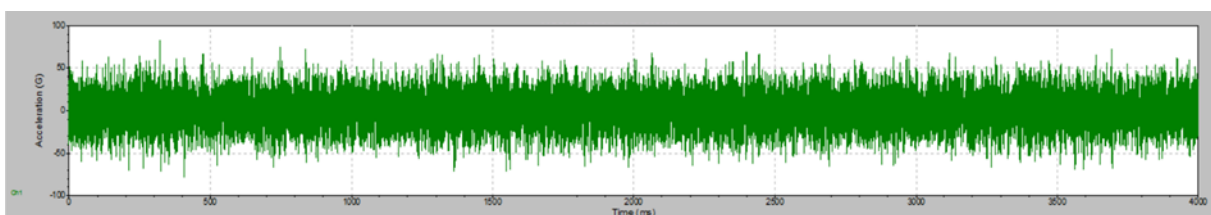
Figure 2.18 Random vibration acceleration wavefront

A simple example of the excitation to which a structure is subjected, can be realized with a [mass – spring – damper] system.
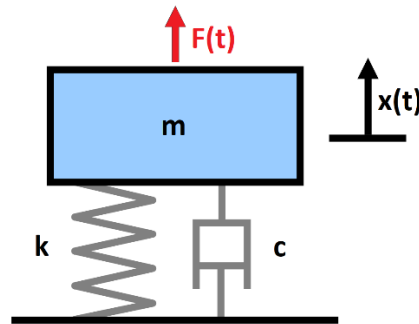
Figure 2.19 Mass-spring-damper model

The equation of motion can be written as

$$m\ddot{x}(t) + c\dot{x}(t) + kx(t) = F(t) \qquad\qquad [\,22\,]$$

$$\ddot{x}(t) + \frac{c}{m}\dot{x}(t) + \frac{k}{m}x(t) = \ddot{u}(t) \qquad\qquad [\,23\,]$$

And given that

$$c = 2m\zeta\,\omega_n \qquad\qquad [\,24\,]$$

$$\omega_n = 2\pi f_n \qquad\qquad [\,25\,]$$

Equation [23] can be written as

$$\ddot{x}(t) + 4\pi\zeta f_n\dot{x}(t) + (2\pi f_n)^2 = \ddot{u}(t) \qquad\qquad [\,26\,]$$

At this point it's common practice to change the domain, expressing everything as a function of frequencies. This allows to obtain much more data from an equal number of analysis as it leads to a stochastic solution. On the other hand, the temporal counterpart would require a number of analyses equal to the number of frequencies, thus leading to an enormous computational cost.

This conversion is done using the Fourier transform which expresses the dynamic response as the combined effect of the various inputs through a transfer function, which allows to determine the system output for each possible input.

Applying the Fourier transform to equation [26], the terms are expressed in the frequency domain, obtaining

$$\ddot{X}(f) - i2\zeta\left(\frac{f_n}{f}\right)\ddot{X}(f) - \left(\frac{f_n}{f}\right)^2\ddot{X} = \ddot{U}(f) \qquad\qquad [\,27\,]$$

Which can be also written as

$$\ddot{X}(f) = H(f)\ddot{U}(f)$$ [28]

Therefore, the transfer function can be expressed as

$$H(f) = \frac{1}{1 - i2\zeta(f_n/f) - (f_n/f)^2}$$ [29]

It needs to be noted that this is a simple formulation to define the acceleration to which a mass is subjected in a system characterized by random vibrations.

MSC Nastran solves this problem in a complex way using the output from the frequency response analysis carried out with a sinusoidal load. This data is then subjected to a data reduction procedure to obtain the random vibration analysis output. This will not be covered in this thesis as it would diverge excessively from its topic.

3   Design Process

The following chapter will focus on the structure and configuration design process, starting with an evaluation of the requirements and design drivers that led to the final iteration.

3.1   Design Drivers

The design of the structure was characterized by several necessities due to the unique short amount of time available to fully develop the spacecraft.

As mentioned before, the project begun at the beginning of January 2023, with its competition scheduled for the beginning of May. In such a narrow time window it was necessary not only to design and produce the various subsystem but also to assemble, integrate and test the satellite.

Figure 3.1 represents the project schedule through a GANTT graph, allowing a better understanding of the strict deadlines faced across the months. Obviously, it provides only a general overview of the timeline of the tasks discussed in this thesis and the deadline faced due to the necessity of conducting other activities, as an example the functional tests.
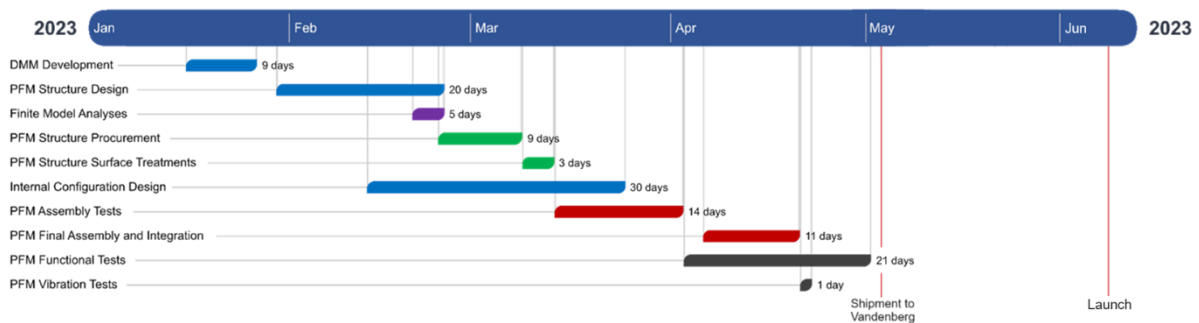
Figure 3.1 GANTT chart for the Spei Satelles mission

Given the short time at disposal, one of the major difficulties in the project was the fact that there was a constant update regarding the specifications of the other subsystems, such as dimensions or requirements. Such constraints made necessary to proceed with a concurrent engineer philosophy, minimizing the design and development time, through a near-real-time teamwork.

This parallelization of the tasks deemed necessary to proceed with a modular structure. What this means is that the structure realized could be easily updated adding or removing inserts for cross-members, as well as moving them upwards or downwards. In this way it was possible to reorganize the space inside the spacecraft, relocating subsystems according to the new inputs.

This philosophy of work proved to be extremely successful as it allowed a drastic decrease in the design phase for what concerns the configuration aspect, allowing to focus the attention on other tasks.

Moreover, due to the fact that several aspects of this mission were highly peculiar and challenging, such as the presence of two on-boards computers as it will be later explained, and

the time was very short, there was always the risk of needing to simplify the spacecraft system, therefore removing some components. This led to the necessity of not having a mechanical dependence between the various subsystems, which needed to be connected only to the structure.

With the prerequisite of conducting the AIV&T activities in the 4 months' timeframe, it was necessary to develop a structure which allowed to minimize the time required for the assembling and integration. Moreover, the baseline adopted for the project was to conduct the testing together with the first two activities.
In such way as soon as some components were integrated, they would have been tested, verifying their correct functioning. This would allow to develop a cyclical workflow minimizing downtimes and allowing the various team members to have proper rest periods.
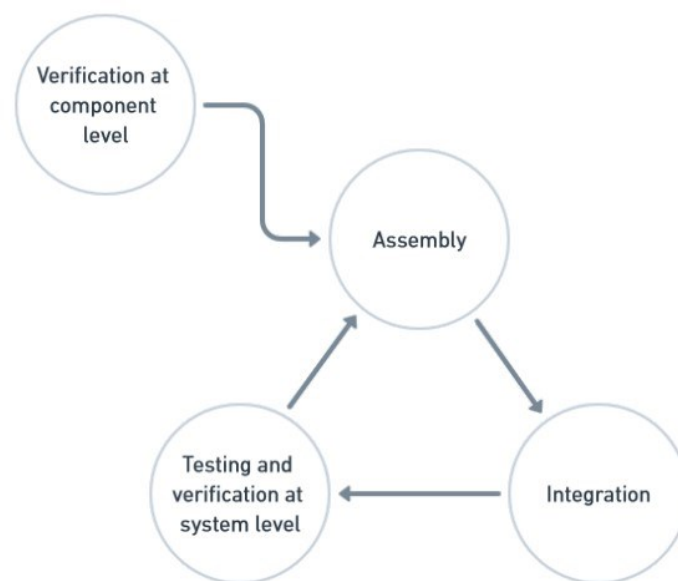
Figure 3.2 AIV&T activities cycle

The result was a series a of activities which needed to be conducted following a precise logic in order to fully test the spacecraft before the launch. The following picture provides an overview of the Spei Satelles mission AIV&T plan through a flowchart.

It should be noted how the cycle earlier described is present in the chart. The functional tests conducted on the PFM are interspersed with the assembly and integration activities, identified as "I-n".
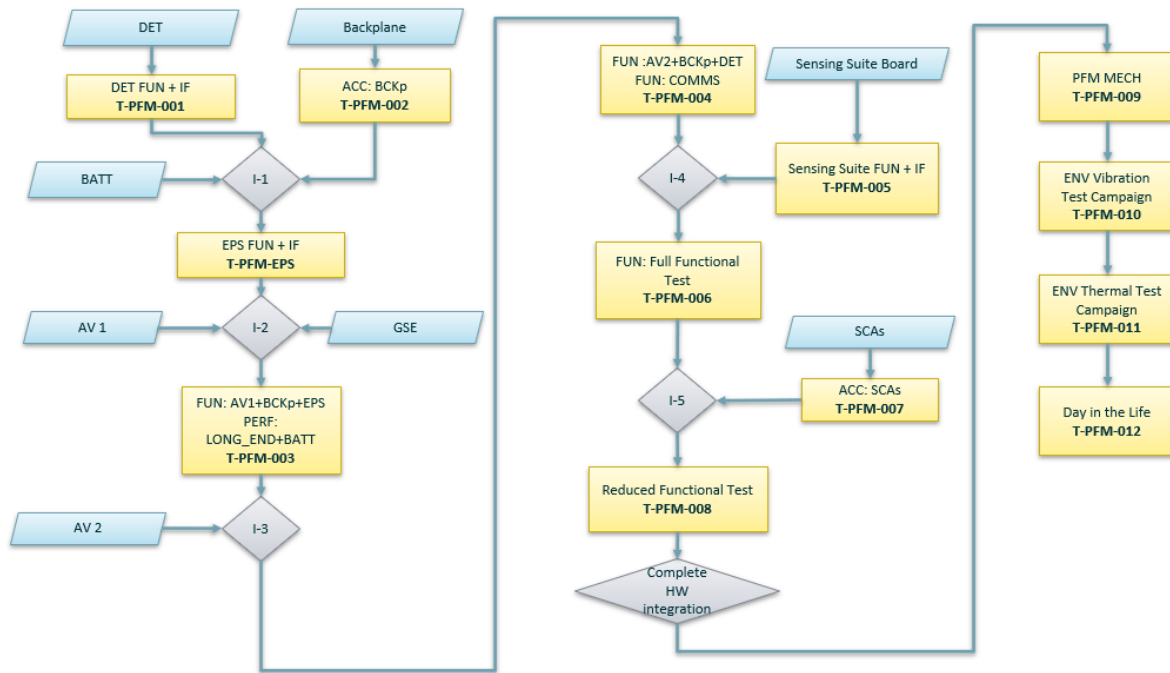
Figure 3.3 AIV&T plan

Another important aspect to keep in mind was the necessity to allow the possibility of conducting repair activities in short amount of time, without needing to disassemble large portions of the spacecraft, wasting large amounts of time to reassemble as well.

Therefore, this translates in an optimal access inside the spacecraft and the possibility to remove components without interfering with the others.

To sum up, the design drivers can be condensed as:

- Modular design.
- Mechanical independence between the internal subsystem to allow last-minute changes or easier repair activities.
- Possibility of testing during the integration phase.

3.2   Requirements

The requirements are a set of technical statements that describe what the mission, and its elements, shall accomplish during its operative life. They are defined at the early phases of a space mission, typically phase 0 and A, and are later updated in specific reviews. They can be classified into high-level and low-level requirements. The former are composed of technical statements produced on the base of the stakeholders' needs and general information defined in the early phase of the mission, such as its statement or objective. The second category, on the other hand, is used to describe the elements of the mission, as well as the mission itself, with a higher degree of detail, based on the design stage.

Moreover, the requirements definition includes the stakeholder needs, as well as government agencies, international organizations and industries, due to their involvement in the

production of a set of standards for space projects. As a result of this standardization work, for example, ECSS standards have been developed. This allows a minimization of the life-cycle cost, while providing detailed information regarding various aspects fundamental to the development of a space mission [13].

Due to the objective of this thesis, the requirements that will be later analysed can be mainly categorized as physical (mechanical) and environmental.
Given the nature of the requirements, their main sources have been documents provided mainly by the other main actors of the Spei Satelles mission: SpaceX and D-Orbit (Astrofein).

3.2.1 Physical requirements

For what concerns the physical requirements, the main document used as a source was the *Astrofein Interface Control Document* [14]. This serves as the user manual of the dispenser mounted on ION, in which SPEISAT was stored, therefore it provides a list of physical and mechanical requirements which needed to be satisfied to safely accommodate the spacecraft inside of it.
The main topics discussed were about the allowed materials, maximum allowed clearance for spacecraft attachments, maximum mass, dimensions, centre of gravity location and the sizes of the rails, as well as the surface treatment to which they needed to be subjected to be hosted in Astrofein.
Moreover, it was also provided further detail regarding the location of the access windows, which proved to be in accordance to the CubeSat standard, as specified in the CDS.

To fill some gaps of information, the CDS handbook was used as completion regarding the physical properties that the spacecraft needed to have, such as the roughness of the rails or further details regarding them.
Nevertheless, in certain aspects there ware conflicts with the *Interface Control Document*, in example regarding the protrusions dimensions on the various faces. For these cases it was decided to keep in account the specifications provided by the Astrofein ICD as it was the deployer used for the mission.
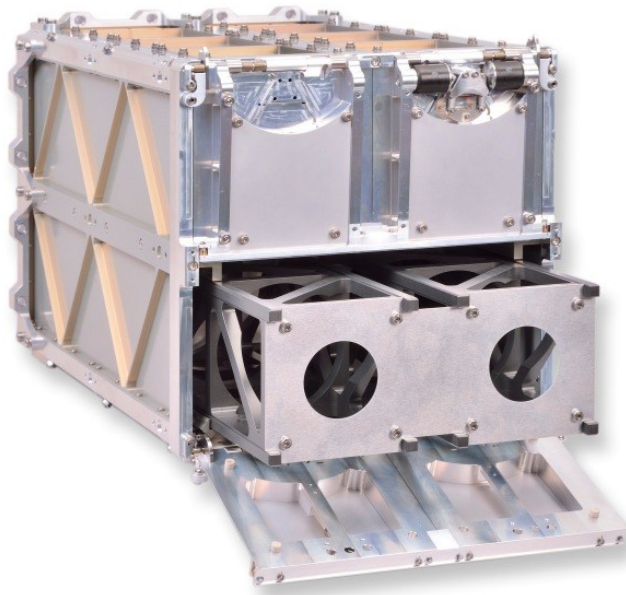
Figure 3.4 Astrofein PicoSatellite Launcher, credits: Astrofein

Furthermore, additional requirements which needed to be satisfied were related to the material used inside the spacecraft. A major concern was related to the various materials used in the subsystems for several different purposes, such as the spacers for the battery pack, the bushes, the thermal gap filler or the cables used to connect all the subsystems.

Therefore, during the procurement phase, the *spacematdb* database [15] was used to establish whether a component was suitable for the space environment.

Thanks to this documentation it was possible to define the following set of requirements.

Physical Requirements		
Identifier	Title	Text
SPEI-SYS-031	Mechanical fixtures	All mechanical fixtures (e.g., screws, bolts, nuts) shall have a defined required torque level, to be applied and measured during integration of the CubeSat
SPEI-SYS-032	Structure material	The CubeSat structure material shall be Aluminium or material with a similar coefficient of thermal expansion
SPEI-SYS-033	Rails treatment	The surface treatment of the CubeSat rails and rail ends, which contact the deployer guide rails and adjacent CubeSat rail ends, shall be hard-anodized aluminium to prevent any cold welding
SPEI-SYS-034	Number of rails	A CubeSat shall have four rails, one per corner, along the Z-axis
SPEI-SYS-035	Rails width	Rails shall have a minimum width of 8.5 mm for both dimensions along X and Y axis

SPEI-SYS-036	Rails edge rounding	The edges of the rails shall be rounded to a radius of at least 1 mm or chamfered to at least 1 mm x 45°
SPEI-SYS-037	Rails roughness	Rails shall have a surface roughness of less than 1.6 μm
SPEI-SYS-038	±Z structure min recess	The main structure of a satellite in ±Z shall be recessed more than 0.5 mm from the ±Z edge of the rails
SPEI-SYS-039	X & Y structure protrusion	The main structure of a satellite in ±X and ±Y shall not protrude beyond the side surface of the rails
SPEI-SYS-040	±Z component min recess	Any equipment/component/part in ±Z shall be recessed more than 2 mm from the ±Z edges of the rails
SPEI-SYS-041	Structure & Rails material	Aluminium 7075, 6061, 5005 or 5052 shall be used for both the main CubeSat structure and the rails. Note: Aluminium alloys which are similar in composition and coefficient of thermal expansion to those listed (e.g., Aluminium 6082) may be accepted. The CubeSat developer shall provide a justification based on similarity of the material properties.
SPEI-SYS-042	Hard anodization layer	The hard anodization layer of the CubeSat rails and rails ends shall be thicker than 10 μm
SPEI-SYS-043	Outgassing	CubeSat materials shall satisfy the following low outgassing criterion to prevent contamination of other spacecraft during launch: • Total Mass Loss ≤ 1.0% Collected Volatile Condensable Material ≤ 0.1% Note: The list of the used materials shall be provided in the Declared Materials List (DML).
SPEI-SYS-044	Maximum clearance X & Y axis	The maximum allowed clearance for satellite attachments between the CubeSat rails shall be normal to ±X and ±Y axis as follows: • ± X axis 12 mm ± Y axis 12 mm
SPEI-SYS-045	Maximum clearance +Z	The maximum allowed clearance for satellite attachments above the rails' ends shall be 4.5 mm normal to +Z axis
SPEI-SYS-046	Maximum clearance -Z	The maximum allowed clearance for satellite attachments concentrically to each slots centre line shall be cylindrical at Z axis with the following dimensions: • Height 58 mm Diameter 92 mm
SPEI-SYS-047	Hazardous materials	Beryllium, cadmium, mercury, silver, and other hazardous materials prohibited by the ISS

		guidelines for Materials (NASA SSP-30233) shall not be used
SPEI-SYS-048	Rails interruptions	The CubeSat rails shall not have interruptions such as gaps, holes, fasteners, or any other features present along the regions of the rails that come into contact with the deployer, other than those for roller switches located within the rails
SPEI-SYS-049	±Z structure max recess	The main structure of a satellite in ±Z shall be recessed less than 7.0 mm from the ±Z edge of the rails
SPEI-SYS-050	Structure accessibility	The CubeSat structure shall have at least 3 faces along the Z axis to allow it to operate on the satellite without obstacles.
SPEI-SYS-051	CubeSat mass	The CubeSat mass shall be less than 2.93 kg[3]
SPEI-SYS-052	CoG location	The CubeSat centre of gravity location measured from the geometric centre shall fall within the following ranges: • X Axis ± 20 mm • Y Axis ± 20 mm Z Axis ± 70 mm
SPEI-SYS-053	Coordinate system	The CubeSat shall use the coordinate system as defined in the figures attached. The origin of the CubeSat coordinate system is located on the geometric centre of the bottom plate (-Z)
SPEI-SYS-054	Carrier Integration	It shall be possible to integrate the CubeSat into the ION carrier with –Z face first.
SPEI-SYS-055	CubeSat dimensions	The CubeSat dimensions shall be as follow: • X dimension: 100 mm ± 0.1mm • Y dimension: 100 mm ± 0.1 mm Z dimension: 340.5 mm ± 0.3 mm
SPEI-SYS-056	Deployer contact	No external components other than the CubeSat rails shall touch the inside of the PSL 12U deployer, when integrated in the deployer
SPEI-SYS-057	Dynamic envelope	The dynamic envelope of a satellite in stowed configuration shall meet the dimensions specified in drawing attached. Note: The dynamic envelope is the volume representing all positions which may be occupied by an object during its normal range of motion, i.e., under static conditions, but also when exposed to mechanical solicitations (e.g., vibration test, ground transportation, launch) resulting in elastic deformation of the object or its components.

---

[3] This value was decided according to the mass of the DMM used by D-Orbit during a testing campaign.

SPEI-SYS-064	Repair activity accessibility	In order to maintain accessibility into the inner part of the CubeSat to allow for a repair activity, in case of anomalies, solar panels and/or side panels shall not be fixed to the structure in a way that access to the satellite requires the primary fixture to be broken. Note: mechanical fixtures (for example screws, bolts, and nuts) are preferred over glue as a primary means of fixture.

Table 3.1 System Physical Requirements

3.2.2 Environmental Requirements

Regarding the environmental requirements, the first document analysed come from SpaceX, the *Rideshare Payload User's Guide* (March 2022) [16], which allowed to better understand the environmental conditions to which the spacecraft shall be subjected during the launch phase, as described in §3.3.

In particular, the attention was brought to the aspects regarding the natural frequencies. The document provided a precise value of the minimum natural frequency of the spacecraft, which shall be at least 40 Hz.

Another useful information used in the analysis campaign was the quasi-static loads that the launch vehicle was expected to generate. Generally, this type of loads isn't particularly critical but were still considered to have a complete view over the spacecraft's behaviour during the launch phase.

Axial load factor [g]	Lateral RSS [g]
7.4	12.9

Table 3.2 Falcon 9 quasi-static loads

For what concerns the random vibrations environment, a document provided by D-Orbit was used as it represented the output of the system composed by Falcon 9 and ION [17]. This was also the one used during the environmental tests as it will be explained in 5.3.

Due to the coupling of the two vehicles, the resulting vibrations environment was a more adverse one for the spacecraft therefore, it produced a more conservative result.

The spectra of the Falcon 9 vibrations and those of the two systems coupled are later compared.

Frequency [Hz]	ASD [g²/Hz] All axes
20	0.00440
100	0.00440
300	0.01000
700	0.01000
800	0.03000
925	0.03000
2000	0.00644

Table 3.3 Falcon 9 random vibrations environment

Frequency [Hz]	ASD [g²/Hz]
20	0.01800
45	0.06000
130	0.06000
230	0.01800
700	0.01800
800	0.03600
925	0.03600
2000	0.00773

Table 3.4 Falcon 9 + ION random lateral vibrations environment

Frequency [Hz]	ASD [g²/Hz]
20	0.012
50	0.022
210	0.022
330	0.048
400	0.048
500	0.024
700	0.024
800	0.036
925	0.036
2000	0.008

Table 3.5 Falcon 9 + ION random longitudinal vibrations environment

Given these inputs, it was possible to determine the environment that the spacecraft shall experience. However, it was still necessary to understand its positioning inside ION and the launch vehicle itself. To fill this gap of information, the previous document was used as it contained data regarding the orientation of the carrier inside the Falcon 9. Moreover, another document was provided which illustrated the position of SPEISAT inside ION. This allowed to determine the position of the access ports and to completely convert the reference frame from the launch vehicle to the spacecraft one. This aspect will be later picked up again, in 4.2.1, with the addressing of loads used during the FEA.

With such premises, the requirements have been compiled.

Environmental Requirements		
Identifier	**Title**	**Text**
SPEI-SYS-080	Natural Frequency	The first natural frequency shall be no less than 40 Hz on the condition that the four rail ends on ±Z are rigidly fixed
SPEI-SYS-082	Random Vibrations Lateral (X & Y axis)	The CubeSat shall be tested for Lateral random vibrations (X and Y axis of ION) as shown in table: Frequency [Hz] / ASD [g²/Hz]: 20 / 0.01800 45 / 0.06000 130 / 0.06000 230 / 0.01800 700 / 0.01800 800 / 0.03600 925 / 0.03600 2000 / 0.00773
SPEI-SYS-083	Random Longitudinal Vibration	The CubeSat shall be tested for Longitudinal random vibrations (Z axis of ION) as shown in table:

Frequency [Hz]	ASD [g²/Hz]
20	0.012
50	0.022
210	0.022
330	0.048
400	0.048
500	0.024
700	0.024
800	0.036
925	0.036
2000	0.008

Table 3.6 System Environmental Requirements

3.3   Dummy Mass Model

The DMM was developed at the beginning of January to serve as a representation of the spacecraft during a testing campaign conducted by D-Orbit on their vehicle.

It was composed of a main structure realized in aluminium alloy Al 5754 h111 which served as a simplified representation of the final structure.

Given the necessity to develop, manufacture and assemble it in less than a month, as the model was to be delivered the 26th of January, the structure was realized minimizing the number of components, therefore having 4 parts for the faces, 4 rails and 3 cross-members, which served as supports for the mock-up of the subsystems' components, as well as to add integrity to the structure.

Furthermore, higher stiffness was guaranteed through 4 threaded bars which crossed the whole model along its longitudinal axis. To fix everything altogether a nut and a locknut were used in correspondence with every cross-member.

The following picture depicts an exploded view of the DMM.
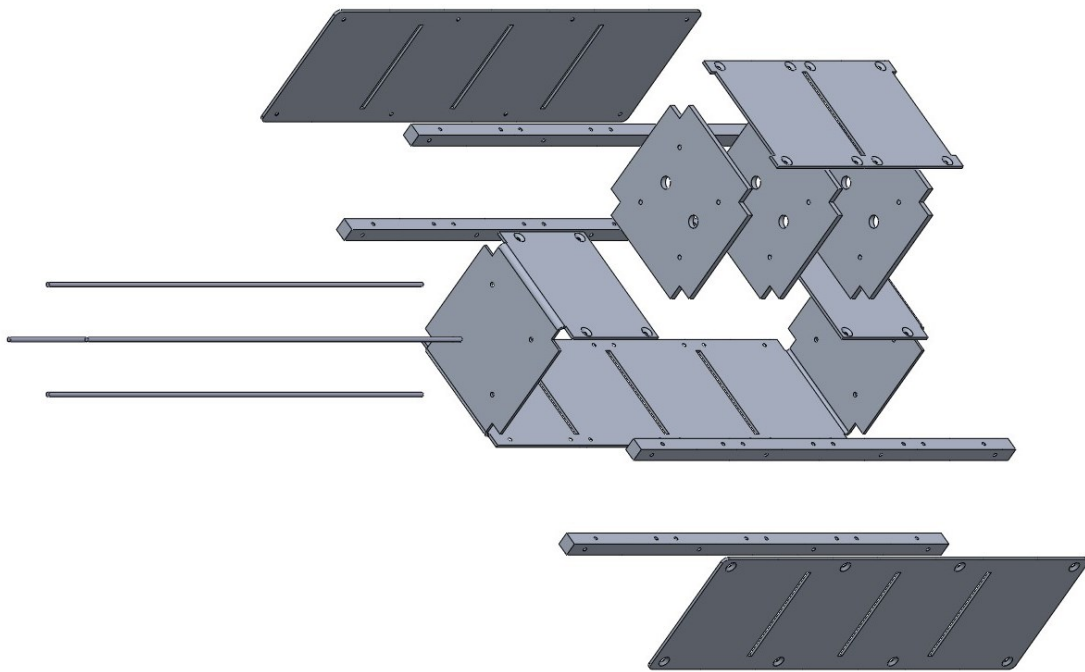
Figure 3.5 DMM exploded view

With such structure it was required to create an accurate representation of the subsystems, in terms of mass, inertia and location.

The components deemed as fundamental to represent were the two C&DH and two CommSys, the battery pack and the backplane[4].

The first three elements were realized using aluminium blocks made in-house, as per the backplane, a thin foil of spring steel was adopted.

Regarding the location of these elements, the battery pack was decided to be located in correspondence to the spacecraft CoG, while the two blocks were to be placed symmetrical to it. In particular it was agreed to store them as close as possible to the $\pm Z$ faces. These were used to each represent the C&DH and CommSys assembly as they were hypnotized to be kept close.

For what concerns the backplane, it was located on what was set to become the $+X$ face.

Therefore, the realization of the DMM led to the definition of the reference frame which will be used during the project.

As per the CDS, the reference frame shall have its origin located in the geometric centre of the CubeSat.

---

[4] The complete system architecture will be discussed in 3.4.1

Figure 3.6 DMM with reference frame

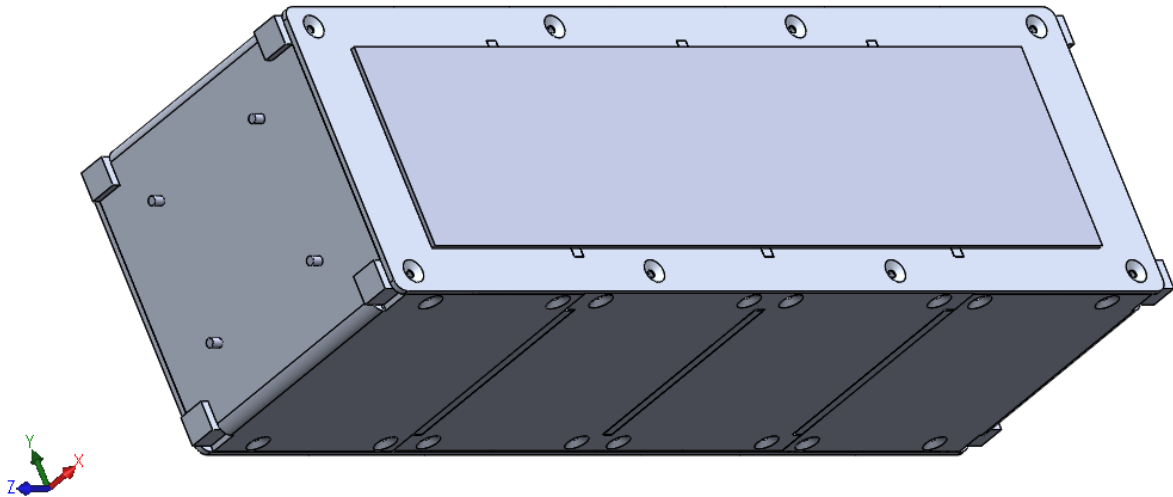With the ending of the assembling phase the model obtained is the one shown in Figure 3.7 and Figure 3.8.Internal view of the DMM
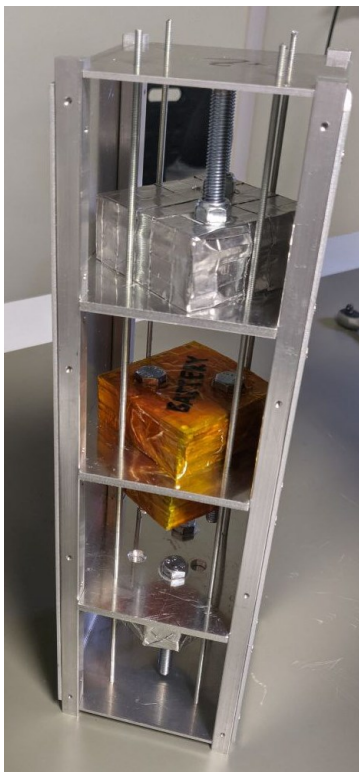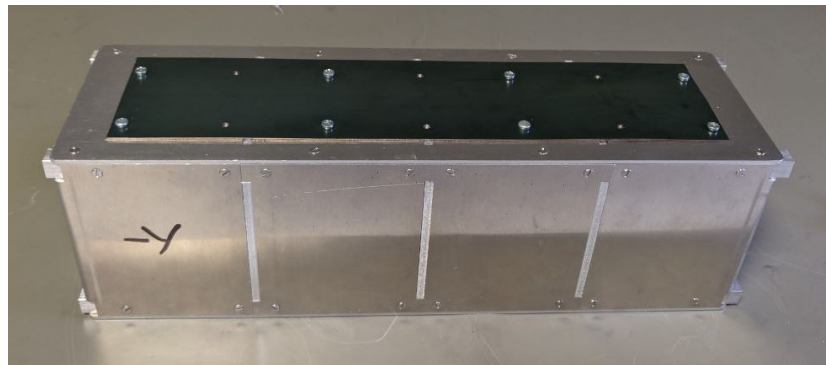

Figure 3.7 Internal view of the DMM

Figure 3.8 External view of the DMM

Which had the following properties:

Property	Value in the CAD model			Value in the physical model
Mass [g]	2970			2930
CoG location [mm]	$X = 3.27$ $Y = 0.00$ $Z = 0.00$			
Moments of inertia taken at the CoG [$g * mm^2$]	$\begin{bmatrix} 26253709.02 & -2369.83 & -1038.61 \\ -2369.83 & 10868899.07 & 0.00 \\ -1038.61 & 0.00 & 5484454.09 \end{bmatrix}$			

Table 3.7 DMM physical properties

As this model was a preliminary representation of SPEISAT, the mass value obtained was used as the spacecraft maximum mass, as seen in the requirement SPEI-SYS-051. This was because the test conducted was a dynamic one, therefore a higher satellite mass at the launch would have led to a more critical, not investigated situation, while a lower one wouldn't have affected the system ION + spacecrafts in a negative way, resulting only in a decrease of the stresses generated inside the carrier.

3.4 PFM

This paragraph shall serve to describe the spacecraft system itself. The model philosophy adopted was the PFM one, with the development of a "flight model on which a partial or complete protoflight qualification test campaign is performed before flight." [18]
This method was decided due to the already mentioned extremely short time available as it allows to perform all the test campaign on the same model, leading to a minimization of costs.
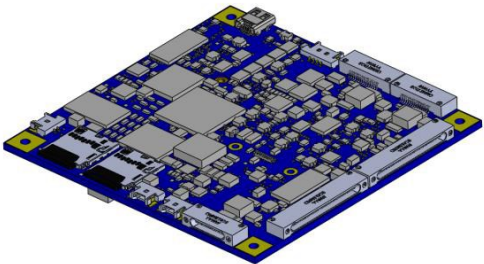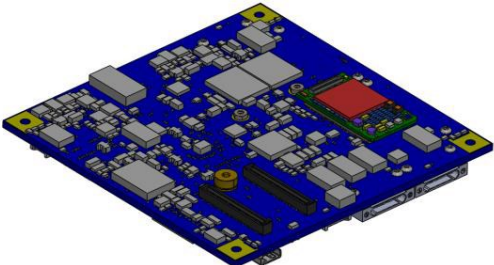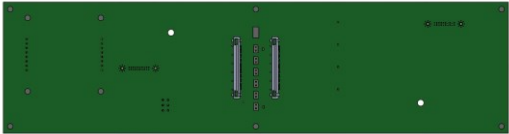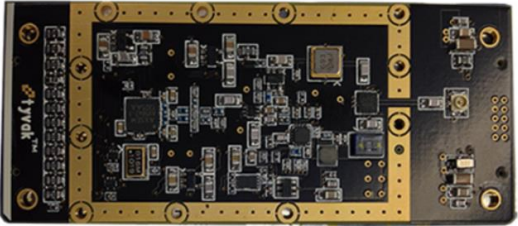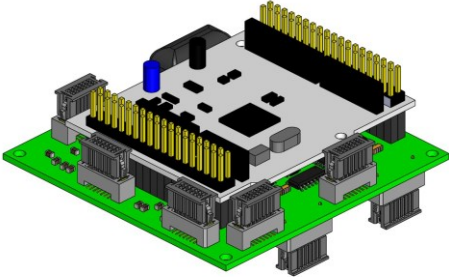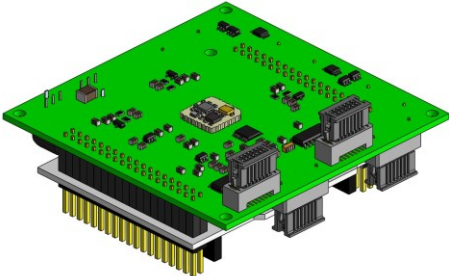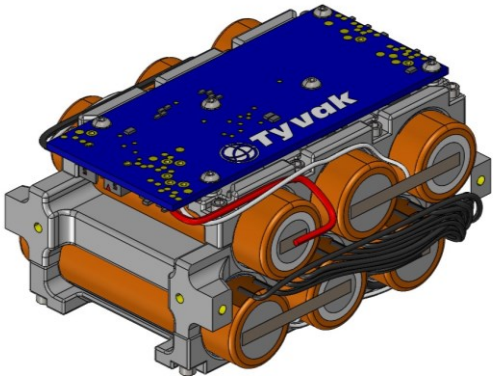
Moreover, the design process adopted was an iterative one, starting from a raw structural frame which would have been refined with each iteration, thanks to the inputs from the various subsystems' groups. Obviously, this method permitted to return to a previous iteration in case of difficulties encountered along the route taken.
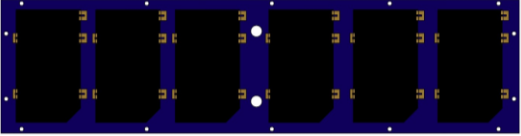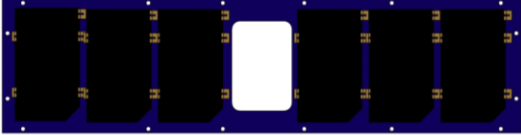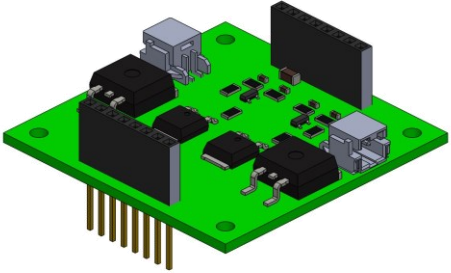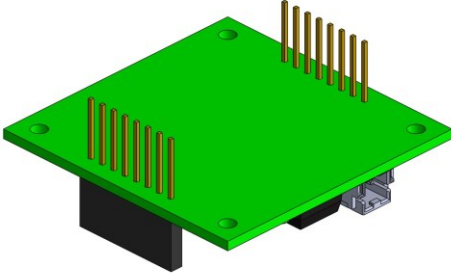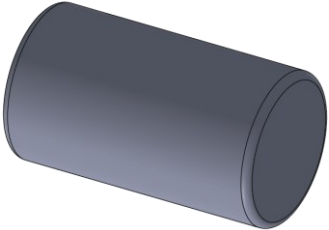
3.4.1 System architecture

Given the already discussed functions of the structural subsystem, it's necessary to discern the various subsystems' components to follow the design phase and its iterations.

Table 3.8 provides an overview of the system architecture, discussing the various components integrated.

Name	Quantity	Description	Picture
C&DH	2	Unlike most CubeSats' missions, it was decided to use two different C&DH implementing a "cold" redundancy. One board has been elevated as master of the other, handling more data and becoming a system critical point, as such there is not an effective redundancy as one component is deemed as more important than the other. Regarding their functions, they provide the system with capabilities of gathering payload and housekeeping data, processing and handling commands through decoding, encryption and decryption and distribution. Moreover, they manage off-nominal conditions guaranteeing the possibility to switch between operative modes.	*Figure 3.9 C&DH front view, credits: Tyvak International* *Figure 3.10 C&DH rear view, credits: Tyvak International*
Backplane	1	The backplane enables a major part of the interfaces among the electrical components, as well as the umbilical connectors, therefore serving as the "backbone" of the system.	*Figure 3.11 Backplane front view* *Figure 3.12 Backplane rear view*

CommSys	2	As per the C&DH system, the communication system is based on two different carrier boards and to each one a transceiver and the antennae are connected, allowing the radio transmission in the UHF frequency of 437.5 MHz. They are located on the $\pm Z$ faces of the spacecraft.	*Figure 3.13 CommSys transceiver, credits: Tyvak International*
Sensing suite	1	It implements the secondary mission performing several tasks. Thanks to a network of thermistors, it's capable of mapping the thermal environment inside and outside the spacecraft verifying the model developed during the project. Moreover, it hosts an IMU, capable of characterizing the internal and external magnetic field and the angular motion [5].	*Figure 3.14 Sensing suite front view* *Figure 3.15 Sensing suite rear view*
Battery pack	1	It's composed of a total of 6 Lithium-ion cells (3S2P) with the function power storage to keep the satellite at full functionality during the eclipse period, when the solar panels aren't exposed to sunlight.	*Figure 3.16 Battery pack, credits: Tyvak International*

Solar panel	4	The solar panels are body mounted, therefore in a fixed position, and are composed of 6 solar cells each allowing power generation when exposed to sunlight. They are located on the $\pm X$ and $\pm Y$ faces of the spacecraft, with the one located on the $+X$ face presenting an opening to allow access to the umbilical connectors.	 *Figure 3.17 Solar panel* *Figure 3.18 Solar panel with access port*
DET	1	Like the sensing suite, this board has been completely developed by the team, with the function of protecting the battery from overvoltage events, as well as providing backpropagation protection to the solar panels. In case of overvoltage events the excessive power is dissipated through two shunt resistors as heat on the spacecraft structure.	 *Figure 3.19 DET front view* *Figure 3.20 DET rear view*
Permanent magnets	2	These have the function of aligning the spacecraft to a reference attitude, using the local magnetic field.	 *Figure 3.21 Permanent magnet*
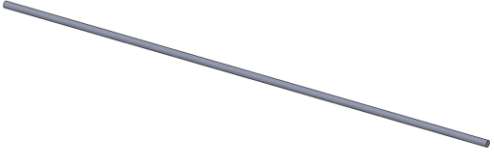
Hysteresis rods	6	These rods are realized with a soft ferromagnetic material capable of damping the angular velocity of the spacecraft thanks to a torque generated due to their interaction with the geomagnetic field.	*Figure 3.22 Hysteresis rod*

Table 3.8 System architecture

With the identification of the various components, it's possible to proceed with the description of the structural design and the relative internal configuration.

3.5 Structural and configuration design

As mentioned before the design followed an iterative process. Therefore, in this thesis the major milestones will be covered and analysed describing the major advantages achieved in those iterations, as well as their flaws or problems encountered by the other subsystems groups, solved in later versions of the design.

3.5.1 1st design iteration

During the first design phase, one of the key points that was established was the necessity to distinguish the structure in two separate groups: the primary and secondary one. The former represented by the $\pm X$ faces together with the rails and their standoffs, while the latter would include all the cross-members, stiffeners and $\pm Z$ faces.

Moreover, as mentioned in 3.1 and 3.2.1, it was necessary to provide the possibility to carry out maintenance work, as well as testing, therefore providing a high degree of accessibility to the subsystems and components. To solve such a problem a blocks solution was conceived, where every component will be firstly mounted on its specific support, as part of the structural subsystem, and be later assembled on the primary structure. This method would have allowed to freely remove components just by losing the appropriate screws, without having to operate on uninvolved parts.

The idea was conceived from the flatsat concept, a motherboard to which all the avionics modules are installed as if it was a real spacecraft, allowing to carry out testing operations. The result to which was aimed, therefore, would have been a flatsat-like assembly which would have been closed only during the final steps of the assembly procedure, leaving the possibility to operate on the subsystems until the last moments available.
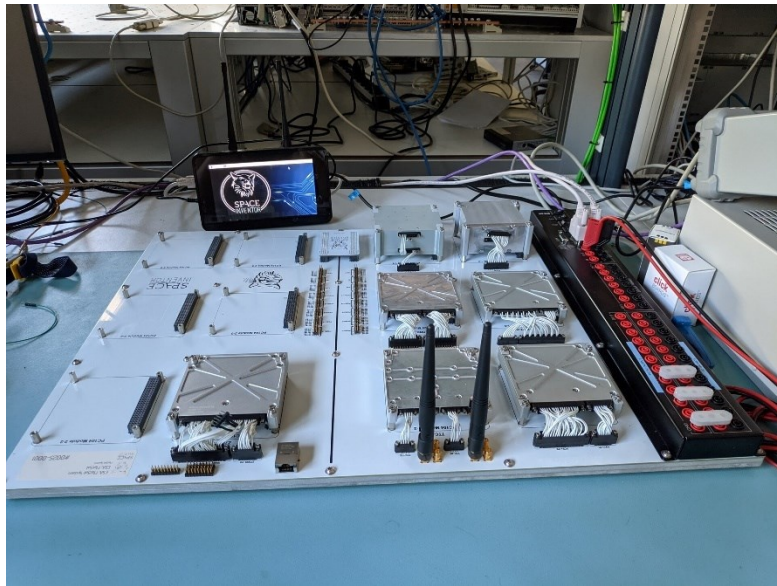
Figure 3.23 CubeSat FlatSat, credits: ESA

With the definition of the key concept, it was possible to proceed with a first design of the primary structure. Knowing that the structure was to be realized through CNC machining, thus starting from a plate, the idea was to obtain a panel with several brackets in correspondence of which it was possible to place either a stiffener, or a cross-member, properly inserted in the corresponding slot.

3.5.1.1 Preliminary configuration
In the following table the location hypothesized for the various components will be presented, as well as the type of support designed.

Component	Position	Support	Motivations
Battery pack	In correspondence of the spacecraft's CoG.	Bound by 2 stiffeners.	The battery pack was the heaviest component; therefore, it was deemed necessary to place it in correspondence with the spacecraft's CoG, preventing a change of its location which was limited as expressed in the requirement SPEI-SYS-052.
Backplane	Directly attached to the $+X$ face.	Primary structure itself.	Due to its size, it was impossible to locate the board elsewhere. Following what was done during the DMM manufacturing phase, it

			was located on the later name $+X$ face.
CommSys	On the $\pm Z$ faces.	Directly attached to the faces.	Due to the board design, the antennae were supposed to be directly connected to the board, minimizing the generation of noise because of the cable losses.
C&DH	Symmetrical to the battery pack and as close as possible to the $\pm Z$ faces.	Located inside a specifically designed case and placed on a cross-member.	The idea was to keep the internal configuration as symmetrical as possible; however, due to the first backplane design, with the DET hosted very close to the battery pack, it was deemed impossible to place the C&DH more centrally. Therefore, they were located near the correspondent CommSys board.
Sensing suite	Near the $-Z$ face	Located on a reinforced cross-member, later referred as cross-stiffener.	During the backplane design phase, it was decided to locate the sensing suite and DET symmetrically to the battery pack due to the volume available and the space required by the connectors on the board.
Hysteresis rods	2 cluster of 3 rods located symmetrical to the battery pack.	Each cluster had 2 of its rods located on a cross-member while the last was to be inserted in a slot carved inside the primary structure	The analysis conducted by the team pointed out the necessity to have 6 rods to obtain better results in terms of motion damping. Assuming that each axis of the spacecraft reference frame had the same number of rods parallel to them. Therefore, those inside the XY plane were placed on the cross-member, while the one

			parallel to the Z axis was inserted in the primary structure corresponding to the $-X$ face.
Permanent magnets	Attached to the $+X$ face separated in correspondence of the CoG, therefore separated by the battery pack	Directly attached to the face itself.	From the ACS simulations it was possible to determine that the pointing effect was maximized when place in correspondence of the CoG.

Table 3.9 1st configuration description

With this first-hand data, it was possible to estimate the location of the various points in which the supports were to be placed. Obviously at this point of the project several volumes were still unknown therefore it was only possible to provide a qualitative evaluation of the space that they were supposed to occupy.

3.5.1.2 Preliminary structure

To simplify the design process, a parametric CAD model was realized, therefore providing the possibility to move the components as well as to add insert or brackets where needed with ease and reducing the risks of ruining the file.

In the *Solidworks* environment it's possible to import external .txt file in which the different measures are quantified. Once the drawing of the model inside the software is realized, it's simply necessary to assign the imported quota to the element of interest. In case it was required to move an object connected to such measures, it's sufficient to modify the amount in the text file. Once the part or assembly is rebuilt, the changes will appear.
When working with assembly however it's important to define accurately the mating preventing conflicts. In this case, for example, the best way to proceed was through the mating of the supports either with a concentric relationship with the brackets or through the coincident one in the case of the cross-members' inserts.

Therefore, keeping in mind the necessity of realizing several inserts for the secondary structure, the primary structure obtained at the end of the first iteration was realized and can be seen in Figure 3.24, Figure 3.27 and Figure 3.28.
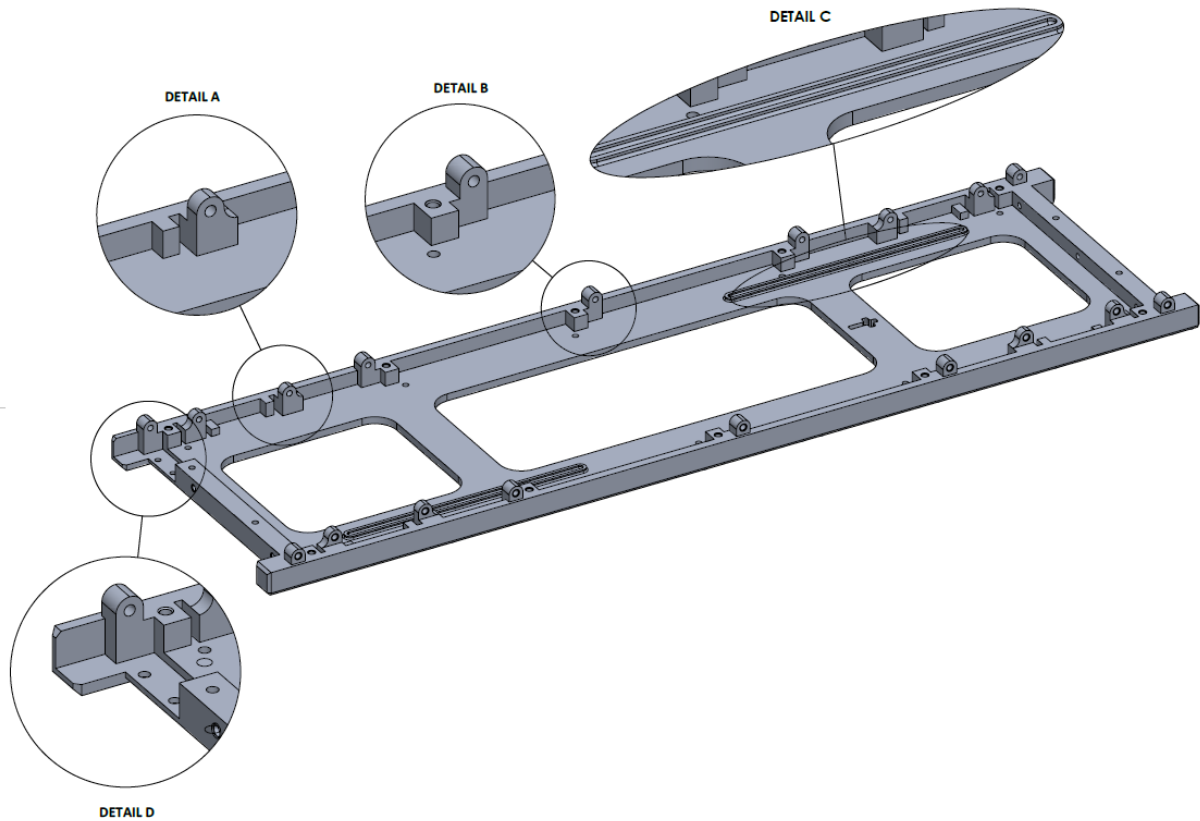
Figure 3.24 -X primary structure internal view

From detail A, it's possible to observe the bracket used to bind the cross-member inserted in the slot visible from the same view.

Detail B represents a point in which a stiffener is supposed to be placed and in this case as well, a bracket is present; however, unlike the cross-member one, it features a hole in the primary structure to further block the reinforcing element. In this way it's possible to prevent not only rotations around the X axis thanks to the bracket, but around the Y one as well.

Detail C shows the socket in which the hysteresis rod is supposed to be placed. The idea was to insert the element inside its slot and to cover it with the Scotch-Weld™ Epoxy Adhesive 2216, widely used in the project to fix the screws during the final steps of the assembly and integration, to prevent them from moving.

Lastly, detail D highlights the groove designed for the deployment switch. As per the CDS the deployment switches are supposed to be two for a matter of redundancy and located on the rail standoffs following the guide shown below.

55

Figure 3.25 Deployment switches configuration options

In this case the design was realized following the model of the switches represented in Figure 3.26.

Figure 3.26 Pressure switch, credits: Banana Robotics

Similarly to Figure 3.24, Figure 3.27 represents the internal view of the $+X$ primary structure.

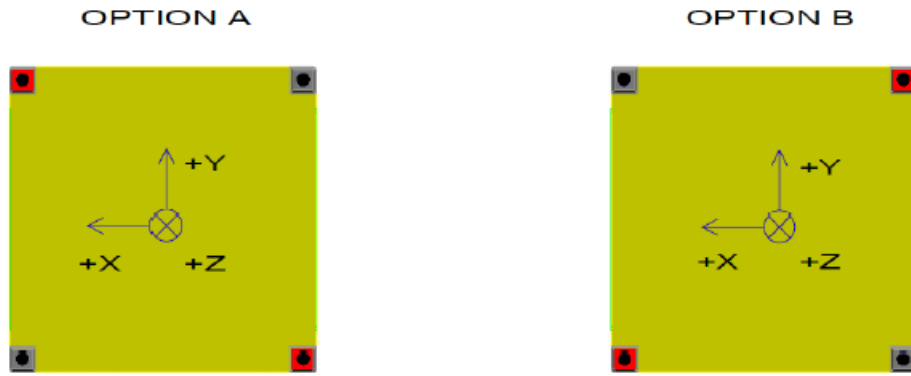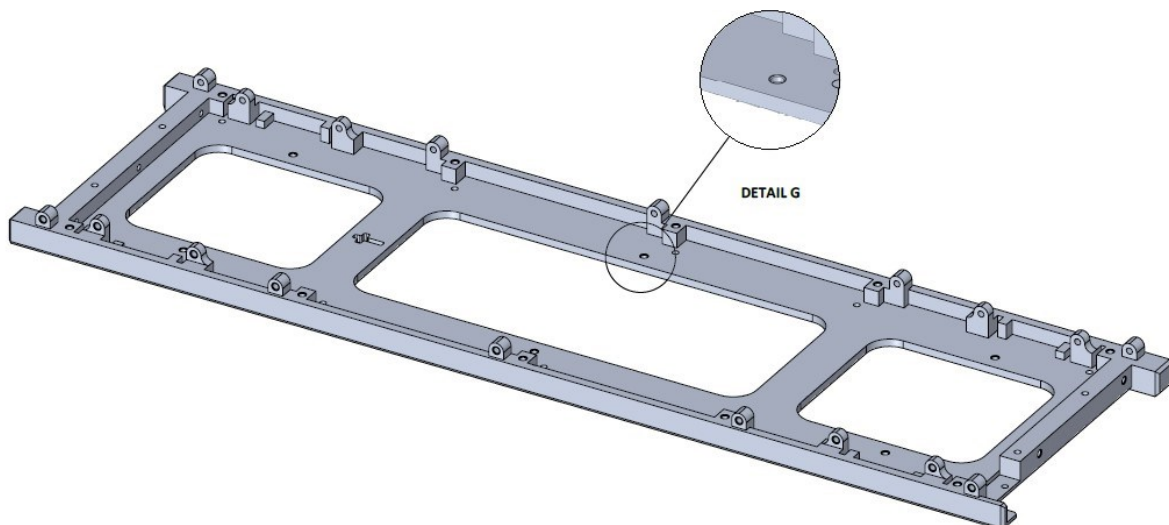*Figure 3.27 +X primary structure internal view*

56

In this figure it's possible to observe the differences between the two faces as it's clear the absence of the slots for the hysteresis rods, placed only on the $-X$ face to simplify the assembly procedure. On the other hand, this component presents the holes designed to hold the backplane, as shown in detail G.

Lastly, Figure 3.28 shows the external face of the primary structure.
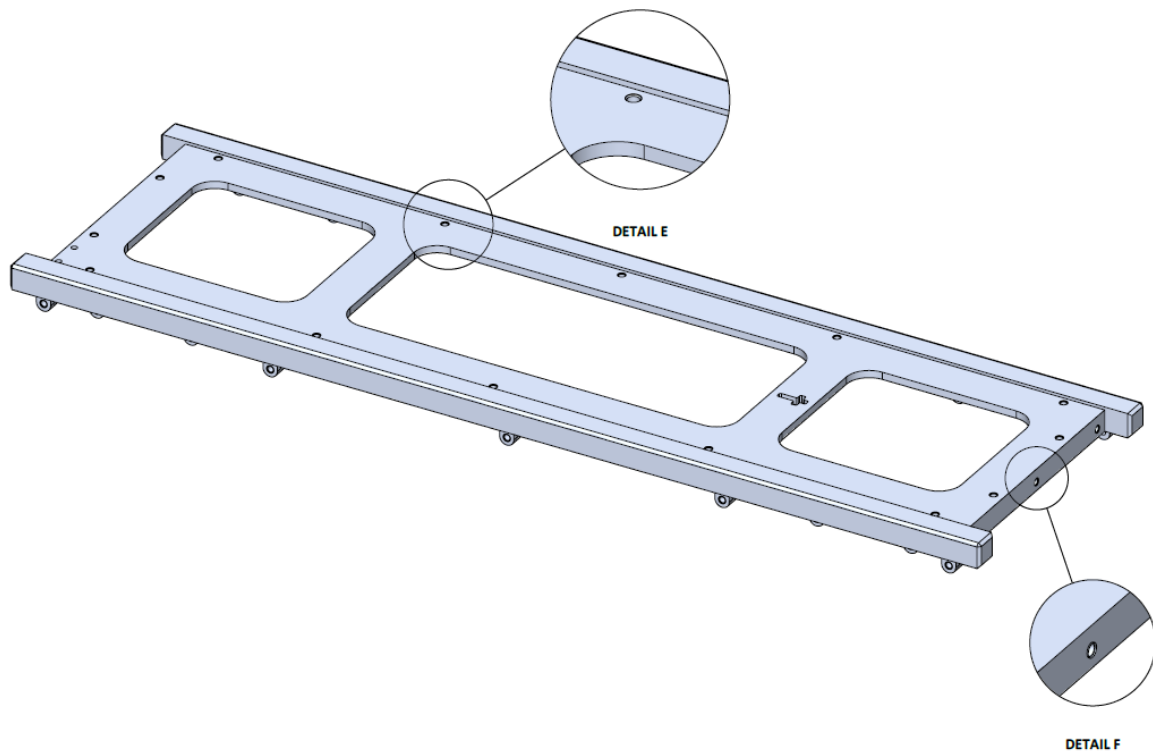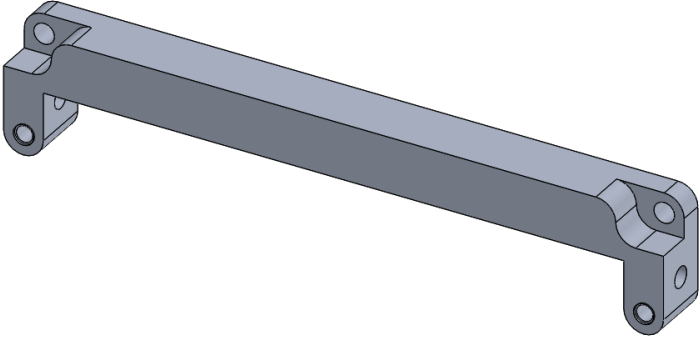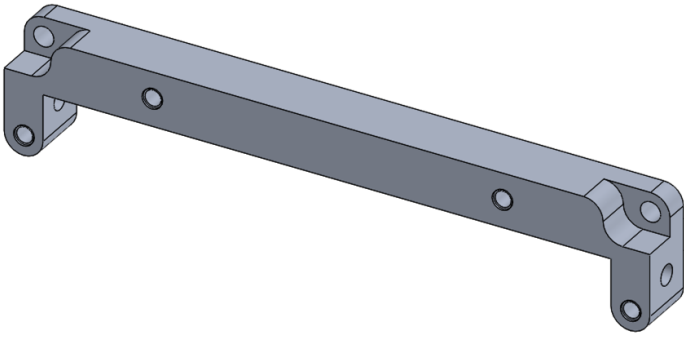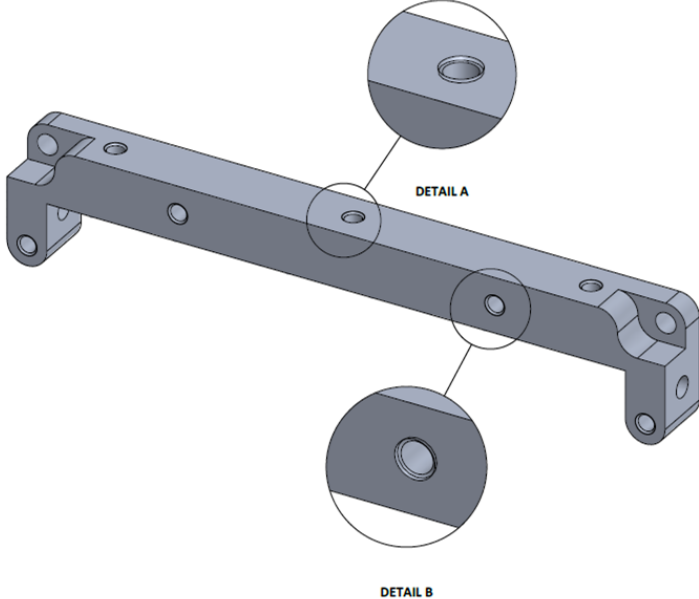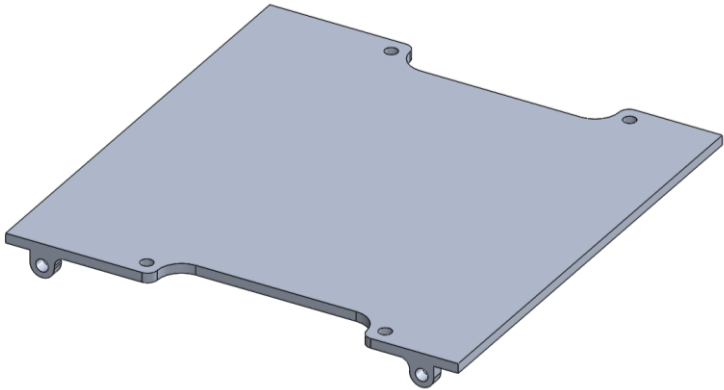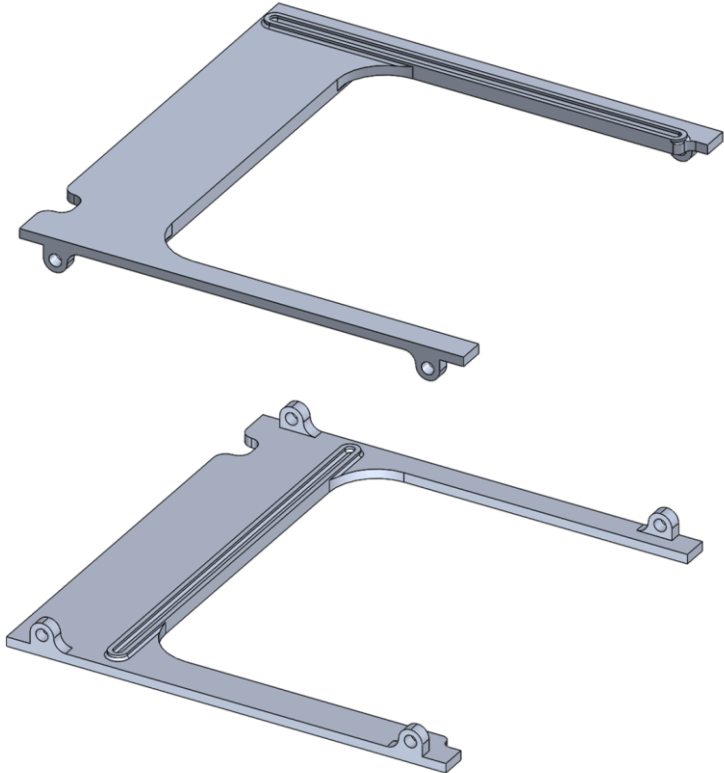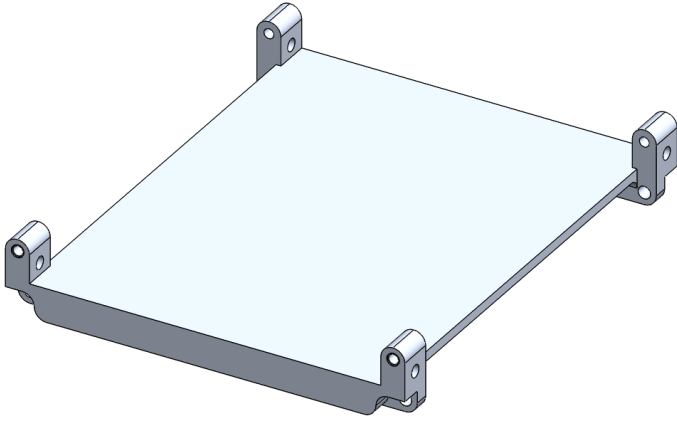
Figure 3.28 Primary structure external view

In such figure it's possible to appreciate the holes used to connect the solar panel to the primary structure in detail E, while detail F highlight the holes that were to be used to connect the structural component to the $\pm Z$ faces hosting the CommSys.

Moreover, from such view it's possible to appreciate the work done regarding the solar panels' clearance. The face ended slightly earlier than the rails, providing an insert in which the panels could be accommodated. In fact, on the $\pm X$ faces they were supposed to be fixed through the holes previously described, while on the $\pm Y$ ones they were to be connected only to the stiffeners.

Moving on to the secondary structure, it may be distinguished into 4 different groups of elements.

Structural component	CAD representatioin	Function
Stiffener		Used to stiffen the whole structure.
		Used to stiffen the structure and support the battery pack, using extra holes.
	DETAIL A DETAIL B	Used to stiffen the structure as well as serving as the coupling point for the $\pm Z$ skins (detail A) and the solar panels (detail B).

Cross-member		It serves as the support for the C&DH, located inside its case. To guarantee the possibility for cables to pass longitudinally inside the spacecraft, two recesses have been designed.
		As its main task is to host the hysteresis rods, it was designed to be particularly light, therefore it presents a big recess to serve as lightening. Moreover, it features a smaller indentation to allow the passing of the groove in which the third hysteresis rod is placed.
Cross-stiffener		It serves as the support for the sensing suite. Being the board a heavy component, the structural element was designed as two stiffeners connected by a plate serving as a tray on which the sensing
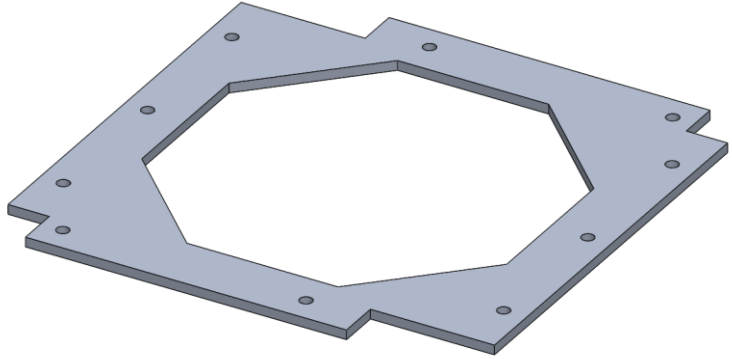
		suite can be placed.
$\pm Z$ faces		From the first iteration the composition of the communication system wasn't clear yet. Therefore, the minor faces were designed with a big hole to allow the connection of the board with the antennae, located inside a box placed outside the spacecraft.

Table 3.10 Secondary structure elements

The result of the first structure and configuration iteration can be seen in Figure 3.29.

#	Component
1	C&DH
2	Backplane
3	DET
4	Battery pack
5	Sensing Suite
6	CommSys
7	Deployment switch

Figure 3.29 1st iteration configuration

While the result of this iteration may not seem particularly relevant due to the unknown volume required by all the components, it actually serves as an ideal base to start with. As mentioned before, the structure modelled is parametric, therefore, many of the sizes which

may need to be adjusted due to newer components dimensions can be changed very quickly. The same can be said regarding the possibility of adding new points in which it's possible to place either cross-members or stiffeners, granting the structure an even higher degree of modularity.

3.5.2 2nd design iteration

With the definition of the volumes occupied by the several components it was possible to size more accurately the space required by each subsystem's element. Moreover, the backplane, as it will be seen, has undergone several changes which allowed to redefine the location of some components.

Furthermore, with the proceeding of the various subsystems' groups the first design criticalities came to light, leading to further changes in the design. Therefore, this second iteration explores the new configuration produced as a response to the up-to-date information and board designs.

3.5.2.1 Updated structure

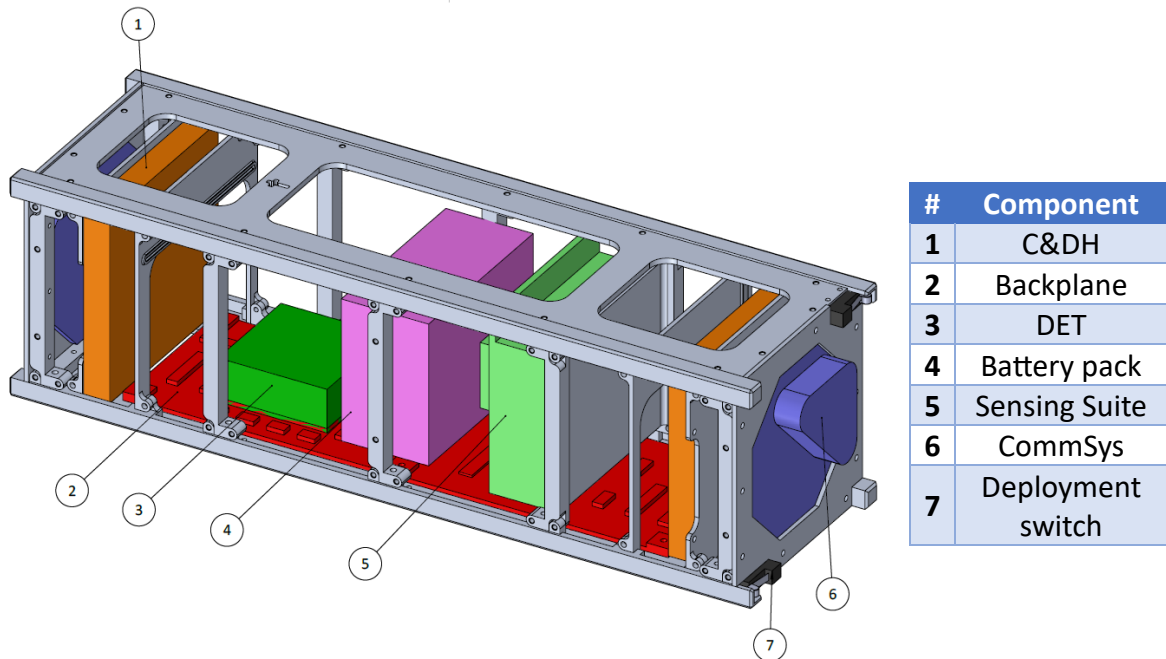With the availability of the CAD models of the components provided by *Tyvak International,* it was possible to proceed with the refinements of the structural elements which were mechanically connected to them.

The first information came from the model of the C&DH. Until this moment there was a lack of information regarding the board dimensions and the maximum thickness achieved due to the various electrical components placed on it. However, it was now possible to proceed with the design of the case to host the board. This was realized as a case composed of two different plates, one realized directly from the cross-member, and the other provided by *Tyvak International* to speed up the development process.

Another critical aspect which needed to be faced was the cable management one. With the proceeding of the development phase, the procurement one started as well. Therefore, it was required to determine the characteristics of the cables needed for the various components, in particular their width.

The C&DH operates with two different wirings, one dedicated to its power supply and the other to the data transmission. As it was required to provide the possibility for them to connect the backplane with the board, dedicated openings were devised.

With such premises, the outcome from the design process is the following cross-member.
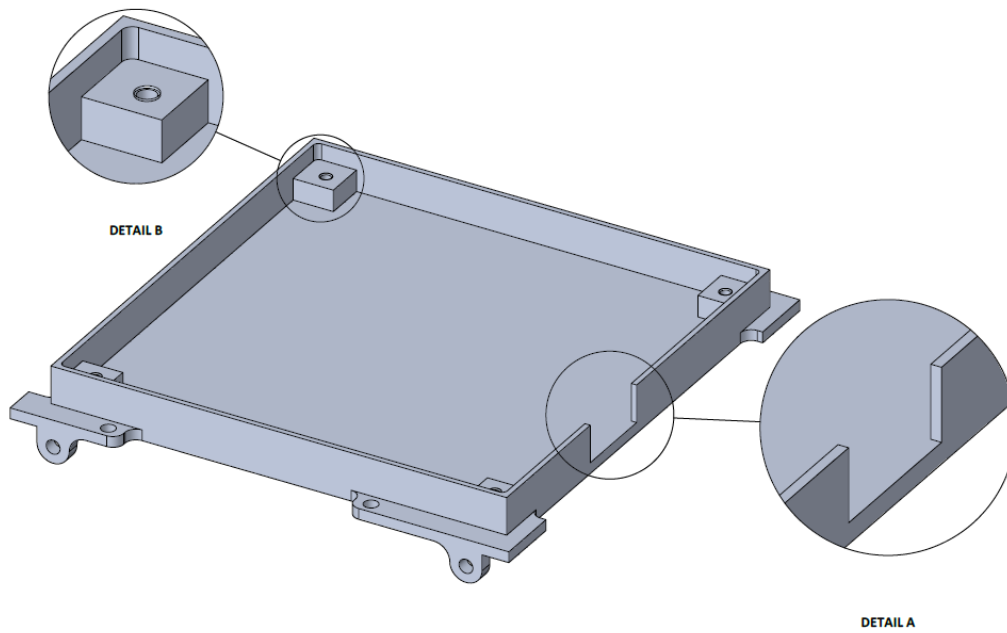
Figure 3.30 Cross-member to host the C&DH

Detail A highlights the slot designed to make the power cable pass, while detail B shows the spacers integrated in the cross-member to keep the C&DH distanced from the structural element, preventing contacts with the electronic components. Moreover, it was designed to be compatible with the second part of the case, provided by *Tyvak International*, as mentioned earlier.
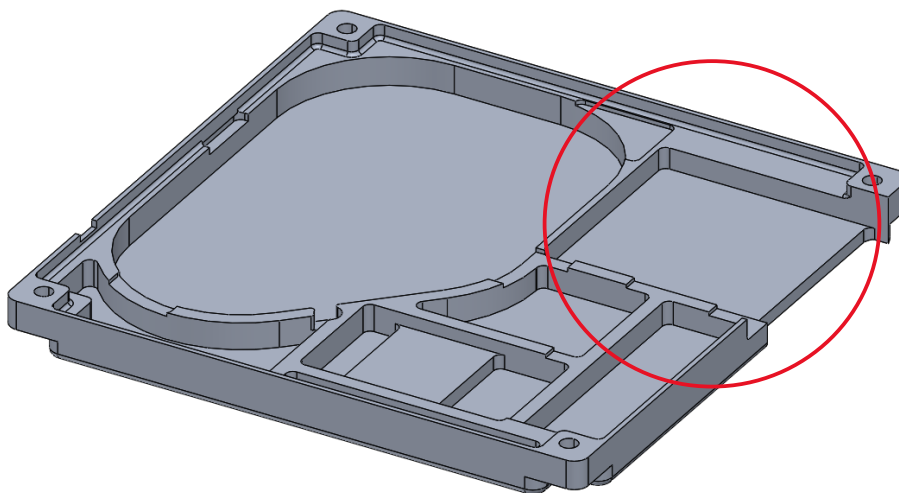
Figure 3.31 2nd part of the C&DH case, credits: Tyvak International

In this figure it's possible to observe the various slot dedicated to the integrated electronics, in particular it's highlighted the one for the flat cable, used for the C&DH data transmission.

Combining the two elements with the C&DH, the following result was obtained.
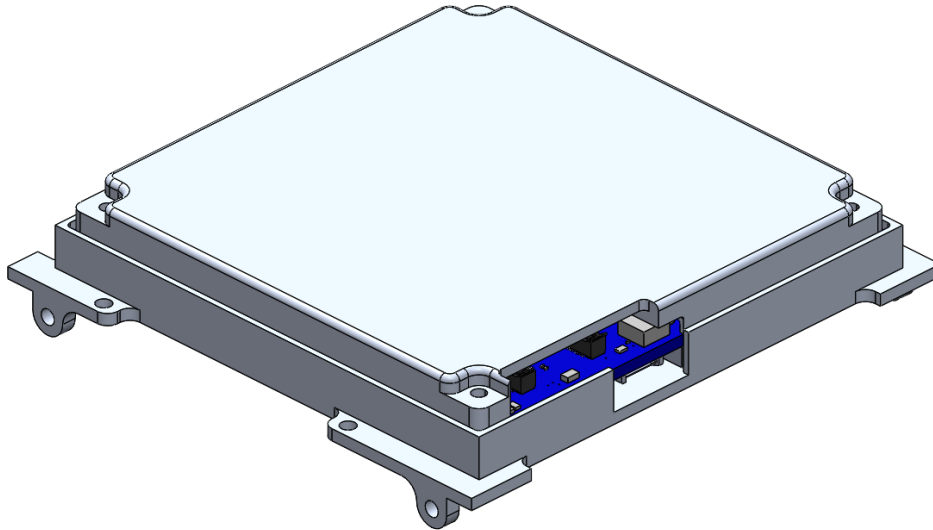
Figure 3.32 C&DH subassembly

This allows to introduce the concept of subassembly, widely used inside this project. As mentioned in 3.5.1, the idea was to create a flatsat-like assembly with the various modules represented by the subassemblies. As it can be seen from Figure 3.32, once the various components are mounted together, it's possible to install the module directly on the primary structure, connecting the electronic components altogether. Viceversa, it can be easily dismounted by simply disconnecting the wirings and proceeding the mechanical remotion of the subassembly.

Another update in the design carried out during this iteration was the cross-stiffener produced to support the sensing suite. With a clearer design of the board, it was possible to model this structural element more accurately.

In particular, the location of the various connector for the thermistors was defined, as well as holes one. Starting from the latter matter, 4 spacers were designed to distance the board from the supporting element, as seen in detail A in Figure 3.33. Regarding the former topic, the connectors placed on the board were 5, for a total of 32 thermistors, respectively placed 3 on top of the sensing suite, and 2 on its back. These last 2 required some space to facilitate the connection of the connectors once the board was integrated in the spacecraft, as well as to help the distribution of the various thermistors. For this purpose an indentation was designed in the cross-stiffener in correspondence with the 2 connectors, as shown in detail B.

Finally, the connectors used to connect the board with the backplane were defined but this didn't affect the structural element whatsoever.

DETAIL A

DETAIL B
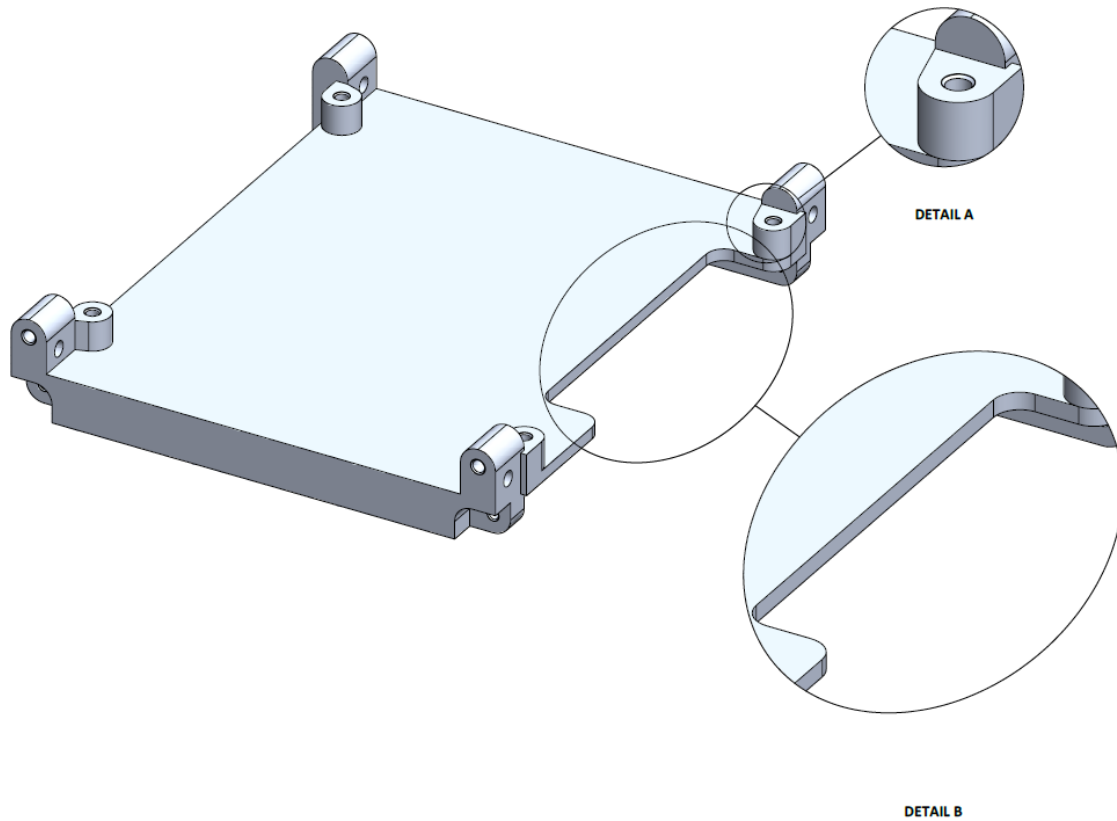
Figure 3.33 Updated cross-stiffener

Further definition of such component allowed to produce the second subassembly.
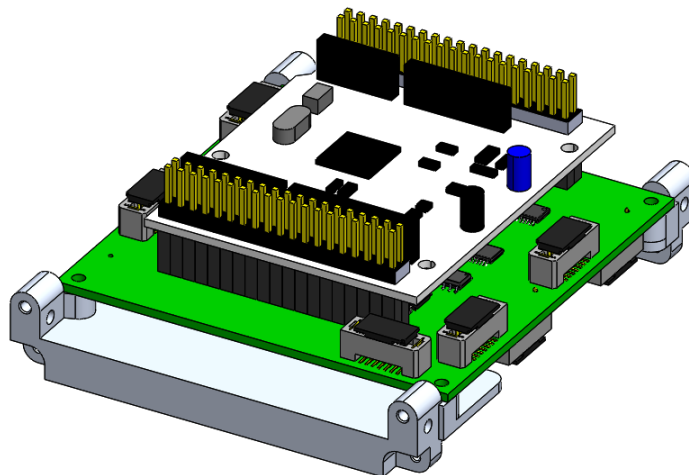
Figure 3.34 Sensing suite subassembly

Moreover, moving on to the CommSys, *Tyvak International* provided the case for such subsystem as their board was supposed to be integrated on the spacecraft, solving one of the main unknowns regarding the secondary structure, as this part was still only a mock-up.

Having this cover, it was possible to join such structural component with the $\pm Z$ faces, obtaining the support in which the CommSys was supposed to be placed. In this way the board

would have faced the external environment providing an interface with the antennae, as expected, while still maintaining the critical components shielded by the outer space radiations and temperature.
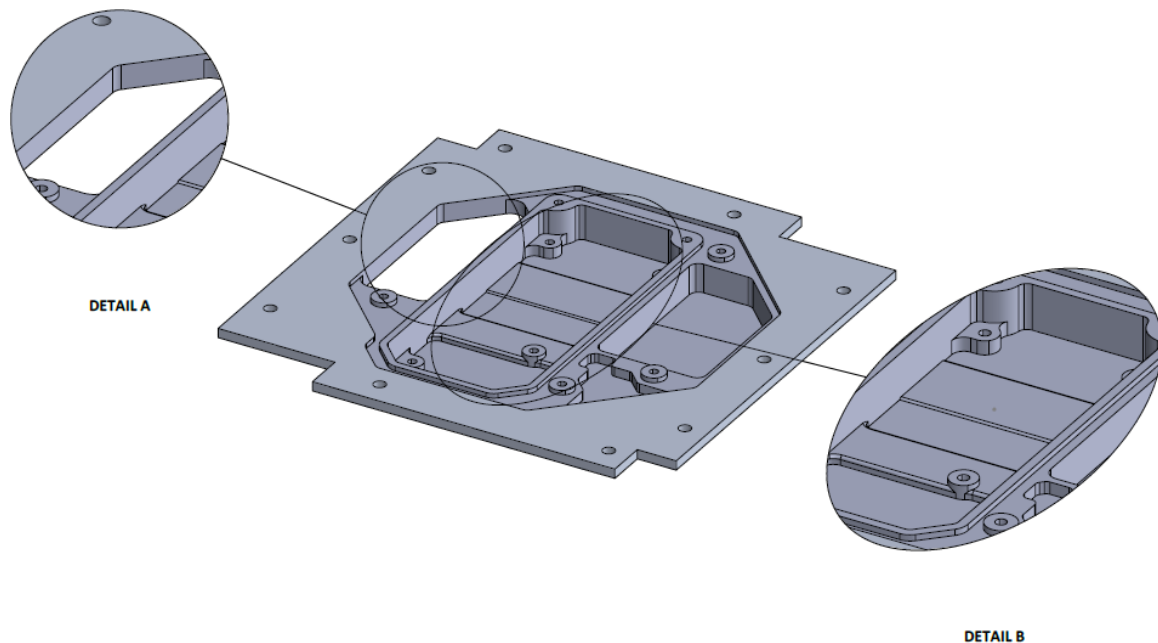
Figure 3.35 −Z CommSys support

In Figure 3.35 detail A highlights a hole left to allow the passing of cables. In this case both power and data passed through the same wiring. Meanwhile, detail B shows the slot in which the transceiver should be inserted in order not to keep it exposed to the interior of the spacecraft. Moreover, this same slot was covered with a thermal pad to grant a more efficient heat transfer from within the spacecraft, as the transceiver faces malfunctioning problems at lower temperatures, more less -10°C, and the thermal analyses conducted highlighted that such event could occur if any changes weren't to be done to the model.

The work done allows to introduce the CommSys subassembly and its main components. It needs to be noted that a transceiver is mounted inside the support, directly attached to the board but in the CAD model this wasn't designed.

#	Component
1	CommSys support
2	CommSys board
3	Antennae case
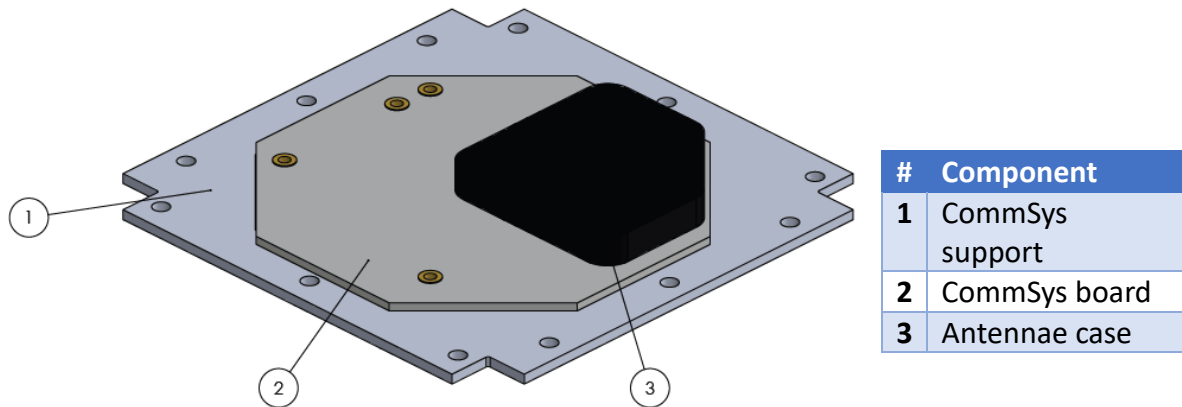
Figure 3.36 CommSys subassembly

Lastly, the primary structure has been updated adding 6 built-in spacers to distance the backplane from the structural element, preventing damages to the board as it could bend due to the launch loads and vibrations, causing repetitive collisions with the aluminium.
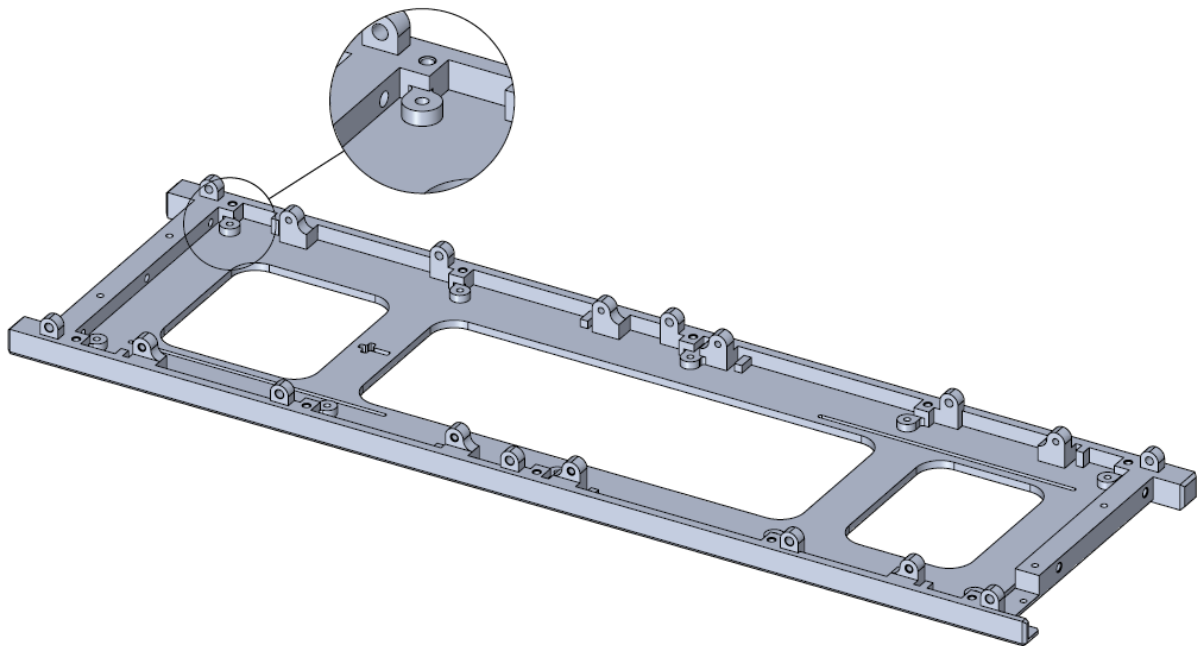
Figure 3.37 Backplane spacer

3.5.2.2 The thermal problem

The knowledge of the orbit in which the spacecraft was to be released allowed to perform several analyses, in particular the thermal group conducted studies on the hot and cold case, bringing up a critical point [19] [20]. From the thermal analyses conducted on *Thermal Desktop* it appeared that the battery pack was subject to a high degree of heat loss through conduction. This represented a major issue due to the operative temperature of such component, which had its lower limit at 5°C and the heaters didn't seem to compensate enough for the heat loss

without consuming an excessive amount of power.

To solve this problem the idea brought up led to the realization of an insulation system to create what was called a "heat bubble". In this way it could have been possible to confine the heat in the battery pack region without having it dispersed through conduction due to contact with the structure. In order to achieve the expected result it was necessary to avoid contact between the battery pack and the stiffeners, as well as between the screws and the same structural components.

The contact between the battery pack and the stiffener could be easily prevented by placing an insulating part between the two components, the chosen candidate was a washer.

On the other hand, the second cause of heat transmission was more complex as the screw wasn't in contact with the structural element only inside the hole, but on its external face as well due to its head. The solution to this problem was achieved using a bush and placing it inside the hole.

The selection of the best materials was carried out through an in-depth analysis on *Spacematdb*, a database which contains useful information which allow to determine whether a material is space compliant or not. In particular, the quantities which were deemed as critical were the RML and CVCM which needed to be respectively lower than 1% and 0.1% [21].

The materials which presented the best thermal and mechanical properties while being compliant to the outgassing requirements were the PTFE, used for the washers, and the Iglidur-X, used for the bushes.
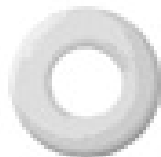
Figure 3.38 PTFE washer

Figure 3.39 Iglidur-X bush

TML	0.05%
RML	0.02%
CVCM	0.00%

Table 3.11 PTFE outgassing properties

TML	0.20%
RML	0.10%
CVCM	0.00%

Table 3.12 Iglidur-X outgassing properties

The reason the PTFE was chosen as the material for the washer was because it's relatively easy to compress. Therefore, it would have been easier to tighten the screws while keeping the insulation properties. On the other hand, the Iglidur-X is incredibly hard (85 on the Shore D scale), therefore its presence wouldn't have affected the structural integrity in any way as it couldn't be dented by the screws thread, causing the battery pack to vibrate during the launch phase.

The addition of these components reflected on the design of the stiffeners dedicated to battery pack support. In particular, a narrowing was designed to keep in account the extra thickness brought by the bush and the washer.
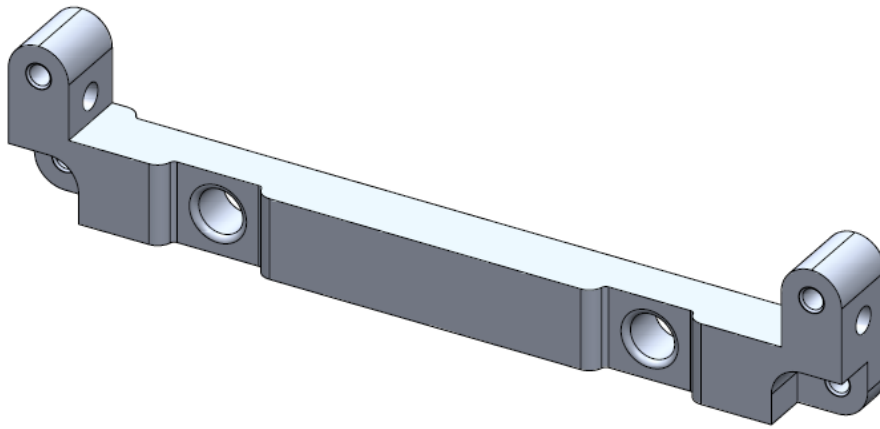
Figure 3.40 Stiffener granting thermal insulation

In this way it was possible to prevent the heat dispersion due to conduction from the battery pack to the rest of the system.

A sectioned view of the thermal insulation system can be seen in Figure 3.41**.**
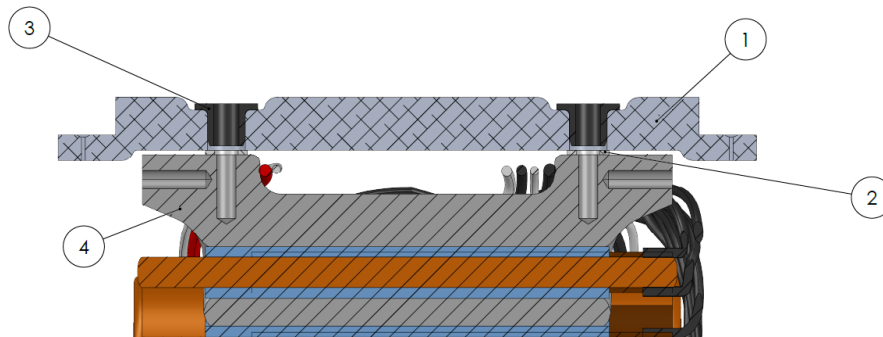
#	Component
1	Stiffener
2	PTFE washer
3	Iglidur-X bush
4	Battery pack

Figure 3.41 Sectioned view of the battery pack insulation system

Thus, obtaining the third subassembly, composed of the battery pack, washers, bushes, and stiffeners.
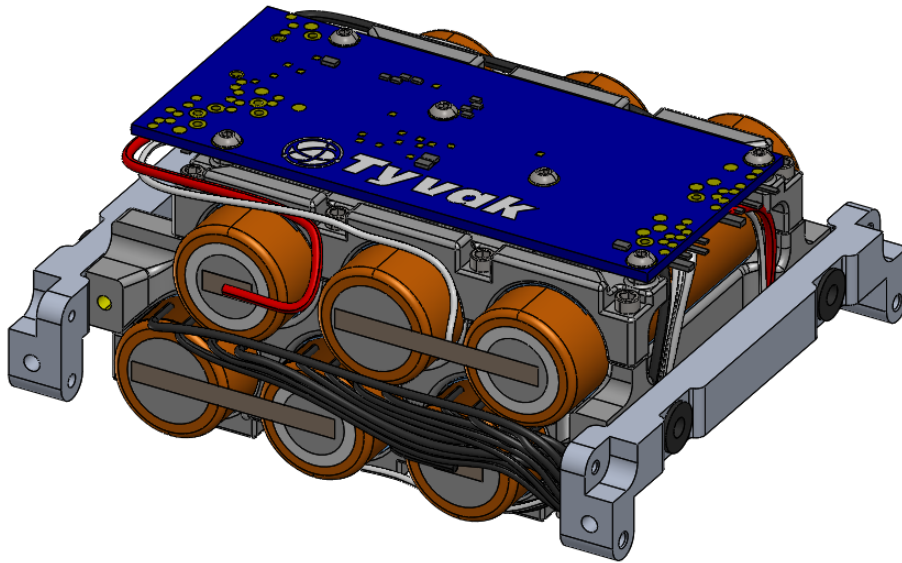
Figure 3.42 Battery pack subassembly

However, the implement solution prevented only heat dispersion due to conduction, without taking into account the radiative component. Moreover, the battery pack didn't generate enough heat by itself, therefore it was necessary to find an external heat source that didn't consume extra power. The solution deemed as the best consisted in the relocation of the C&DHs close to the battery pack in order to exploit the heat produced to further warm the component without having to turn on the heaters. This was possible also thanks to the updated backplane design, which placed the DET closer to the $+Z$ face.

To guarantee and maximize the heat exchange, a thermal pad was used as it was placed between the C&DHs' case and battery pack. Moreover, it was decided to implement the same solution inside the cases themselves, as the thermal pad was located in correspondence of the flat cable slot, guaranteeing a good conduction between the board the structure as well.
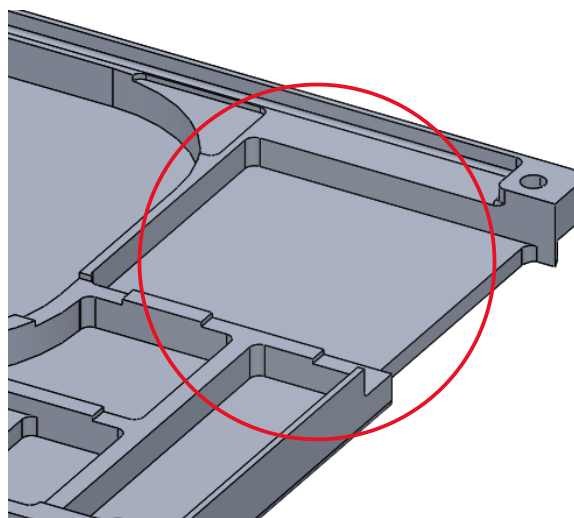
Figure 3.43 Thermal pad location inside the C&DH case

3.5.2.3 Updated configuration

The variations to the design during this iteration led to an updated configuration with several differences from the previous one, the main ones being more precise measures due to the absence of mock-up subsystems, substituted by the actual CAD models of the components, although still in development hence subject to changes.
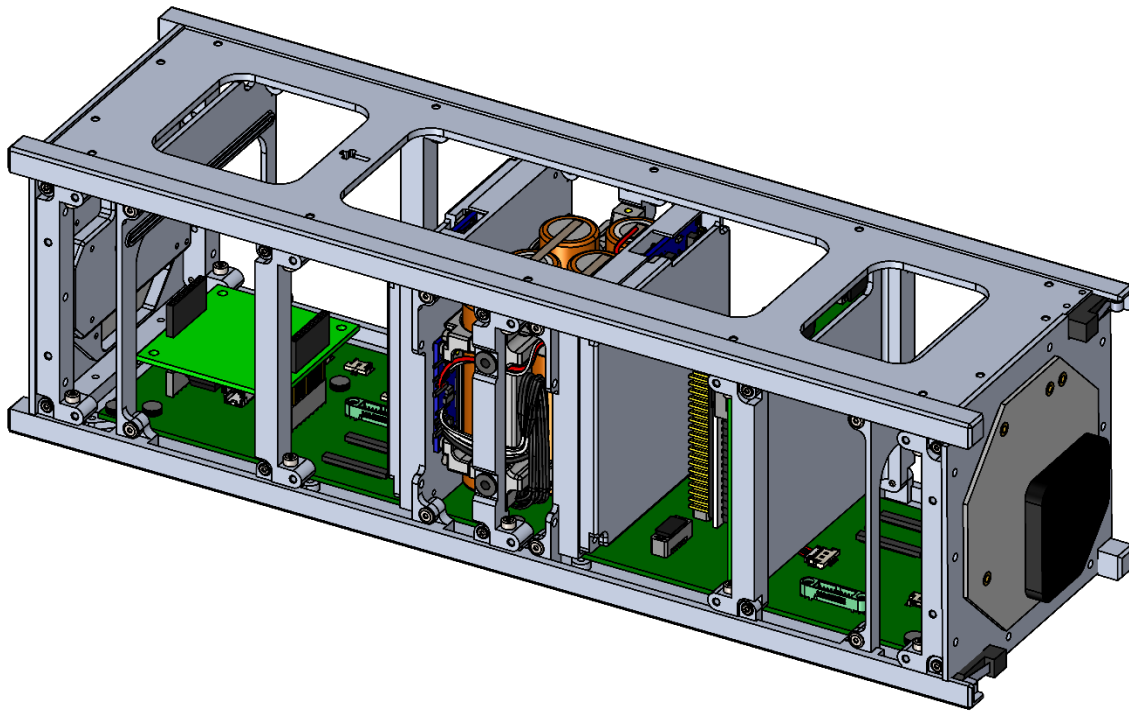
Figure 3.44 2ⁿᵈ iteration configuration

To sum up, during this iteration the main changes introduced were:

- The introduction of a thermal insulation system to prevent a temperature drop in the battery pack.
- The shift of the C&DHs to further increase the battery pack temperature.
- The development of the C&DHs' case.
- The development of the CommSys support.
- Minor modifications to the cross-stiffener.
- Minor changes to the $+X$ primary structure.

3.5.3 3ʳᵈ design iteration

With the 2ⁿᵈ design the location of the internal components is almost completely defined as there are only minor tasks remaining. Therefore, this iteration focuses on improvements to the structure due to necessities which came up with the proceeding of the work.

3.5.3.1 Updated primary structure

The main characteristics of this component remained mostly untouched during the whole design process; however, some finishes were required before sending it in production.

One of the biggest alterations to which it was subjected was the change of the deployment switches. In 2.1 it was explained that 2 deployment switches were to be installed to guarantee the shut-off of the spacecraft during all the ascension phase by keeping the circuit open. Unlike what was said earlier, it was later decided to proceed with the utilization of separation switches. Differently from the deployment counterpart, these are supposed to produce a small push when closing the circuit thanks to their mechanical system, helping the carrier deployer to safely eject the spacecraft.

Figure 3.45 Separation switch, credits: Metrol

Due to this change, a small design change was required in the slot designed initially for another type of switch.

The idea was to create a small hole in the $-Z$ rail standoff in which the switch was to be inserted. A counterbore was designed inside the hole to halt the insertion of the electrical component when it reached the correct longitudinal position. Moreover, to keep it fixed, it was decided to use a grub screw that once tightened would have stopped the switch thanks to the pressure it exerted.

After the counterbore the hole would have continued to guarantee the passing of wirings that would have exited from a small bay located inside the primary structure, near the dedicated connectors located on the backplane. Furthermore, this hole had a double function, as it could be filled with the already mentioned Epoxy Adhesive 2216 to prevent the moving of cables during the ascension phase.

Cable management is a critical point in the design of a spacecraft configuration as the vibrations generated by the launcher can cause the wirings to repeatedly impact on the structure or other components. This could lead to damages to the cables or, in the worst cases, to their cut-off.

The importance of this aspect varies from component to component, as in some cases the worst that could happen would be a degradation of the mission or the loss of some functions, such as due to the cutting of a thermistor wire. However, the separation switches' cables represent a mission critical point in the system design as their malfunction could compromise the whole mission.

In this mission context the safety of the cables was guaranteed with several methods that will be later analysed.

#	Component
1	Grub screw hole
2	Separation switch hole
3	Counterbore
4	Cable's bay

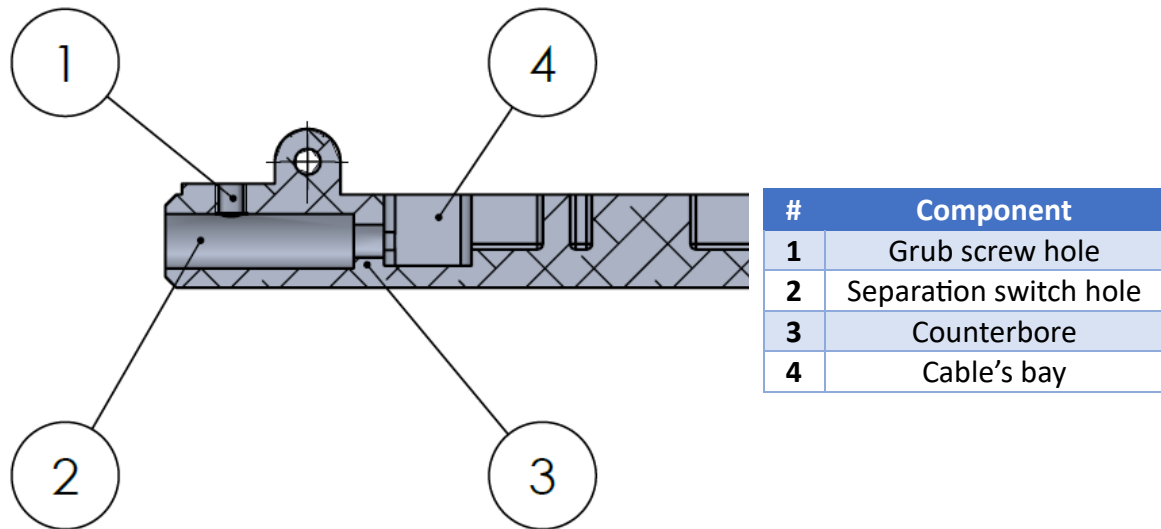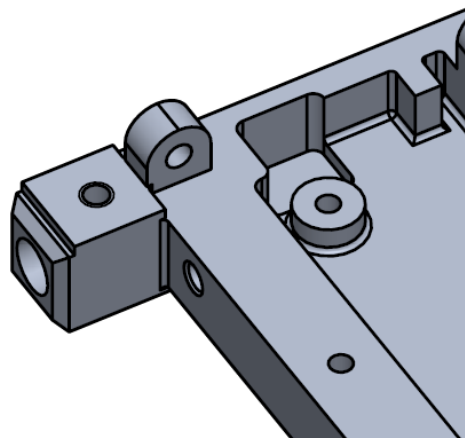*Figure 3.46 Sectioned view of the separation switch hosting system*

Figure 3.47 Separation switch hosting system

A smaller change to which the primary structure was subjected, in particular the $-X$ one, was the realization of wider lightening to allow the C&DH flat cable to bend more gently, preventing it to be damaged due to the narrow bending angles and the possibility of repetitive impacts with the structure.
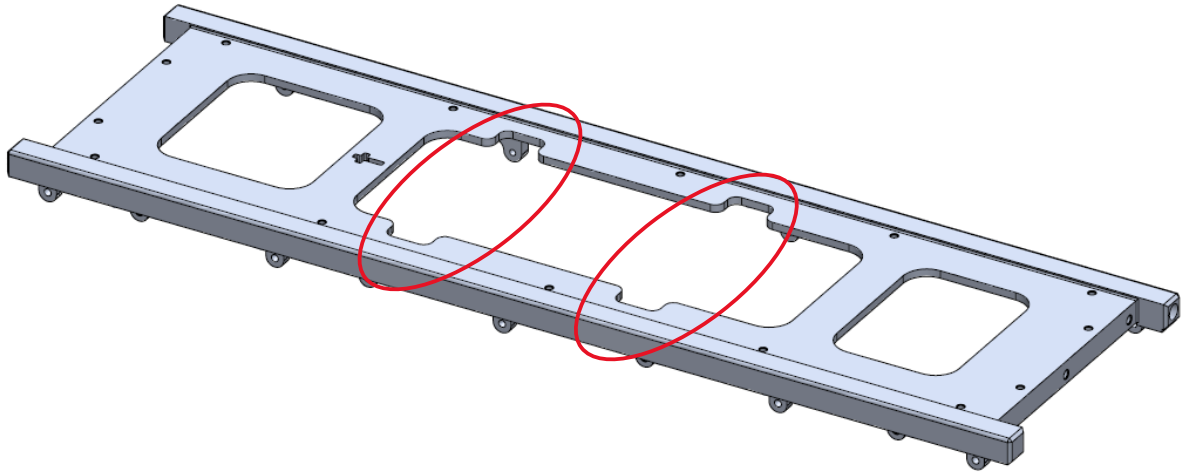
Figure 3.48 Updated −X primary structure

3.5.3.2 Updated secondary structure

As already explained in 3.5.2.2, the battery pack suffered from a drastic heat loss, which could lead to its malfunction. Among the different solutions implemented, the shift of the C&DHs closer to the cells didn't seem to prove enough effective due to the excessive heat loss cause by the mechanical path between the board and the rest of the structure.

The first idea brought up was the utilization of the same PTFE washers inside between the board and the cross-member, without the need to re-design components. However, this couldn't solve the problem regarding the conduction through the screws. Moreover, it was impossible to use the same Iglidur-X bushes as they were incompatible with the board holes diameter. The idea to use smaller bushes was immediately rejected as they would have been too little, thus requiring screws which couldn't safely secure the C&DHs.

Therefore, the only possible solution was the realization of the cross-member completely separated from the case, and not as a part of it. In this way it would have been possible to place the thermal insulation components between the two structural elements without compromising the safety of the board.

Obviously, such solution required the case to be facing towards the battery pack as in the previous iteration, the cross-member was the component the closest to it. Maintaining this configuration would have resulted in a worse scenario as the cross-member would have been colder and not capable of heating the battery pack.
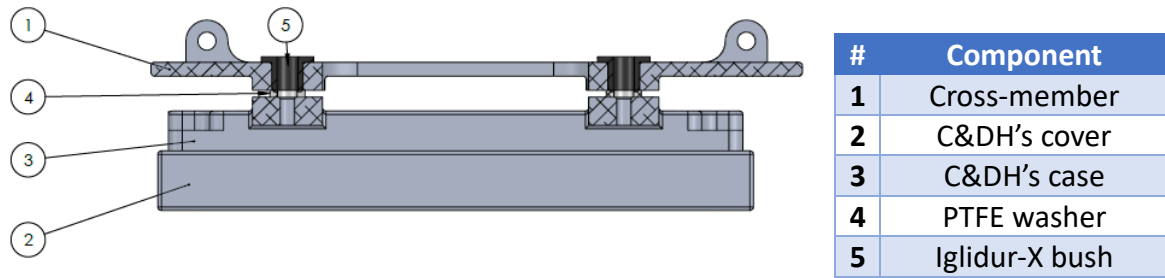
#	Component
1	Cross-member
2	C&DH's cover
3	C&DH's case
4	PTFE washer
5	Iglidur-X bush

Figure 3.49 Sectioned view of C&DH insulation system

As mentioned in 3.5.2.1, the C&DHs required flat cables for data transmission, these proved to be particularly critical as they are extremely delicate, needing to be bent only within a certain angle range. Therefore, it was necessary to give them as much space as possible to bend, increasing their turning radius, as well as preventing impacts with the structure. The latter problem was solved with the widened lightening realized in the $-X$ primary structure. For what concerns the former, the cross-member was designed to keep the C&DHs' case as close as possible to the backplane, without compromising its safety.

Figure 3.50 C&DH flat cable

The changes introduced led to the redefining of the C&DH subassembly, introduced earlier, which is now composed of the three structural elements and the C&DH board. The new design doesn't affect the modularity of the system whatsoever and it's still possible to obtain a flatsat-like model.

It needs to be specified that the primary structure received a slight modification regarding the location of the inserts for the C&DH subassemblies due to the reasons explained above. Moreover, it was still necessary to grant an adequate proximity between them and the battery pack as countermeasure to the thermal problem.
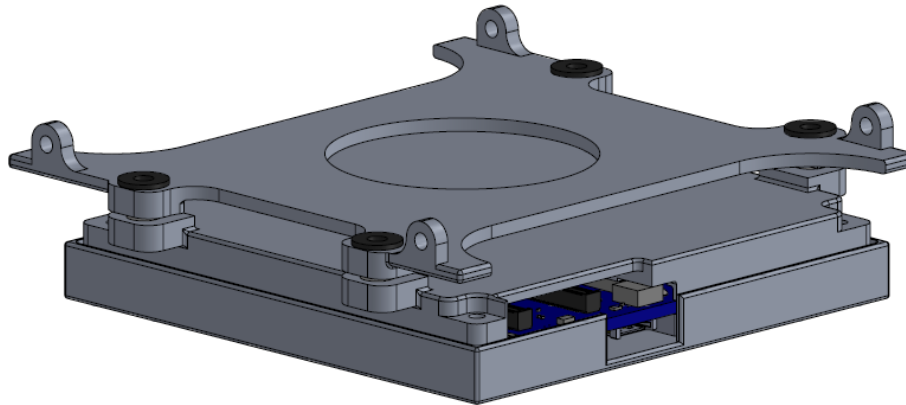
Figure 3.51 Updated C&DH subassembly

Finally, a minor consideration done during the final design review was about the temperature of the solar panels. From the thermal analyses, these resulted to reach extremely high temperatures, resulting in their degradation. This was caused by a poor degree of thermal conduction between the panel itself and the rest of the structure, through the face on which it was located, especially in the $\pm Y$ faces cases, where they were connected only to stiffeners. To prevent such issue, it was decided to implement a similar solution to the one used to guarantee a good thermal conduction between the C&DHs and the battery pack, thus using thermal pads.

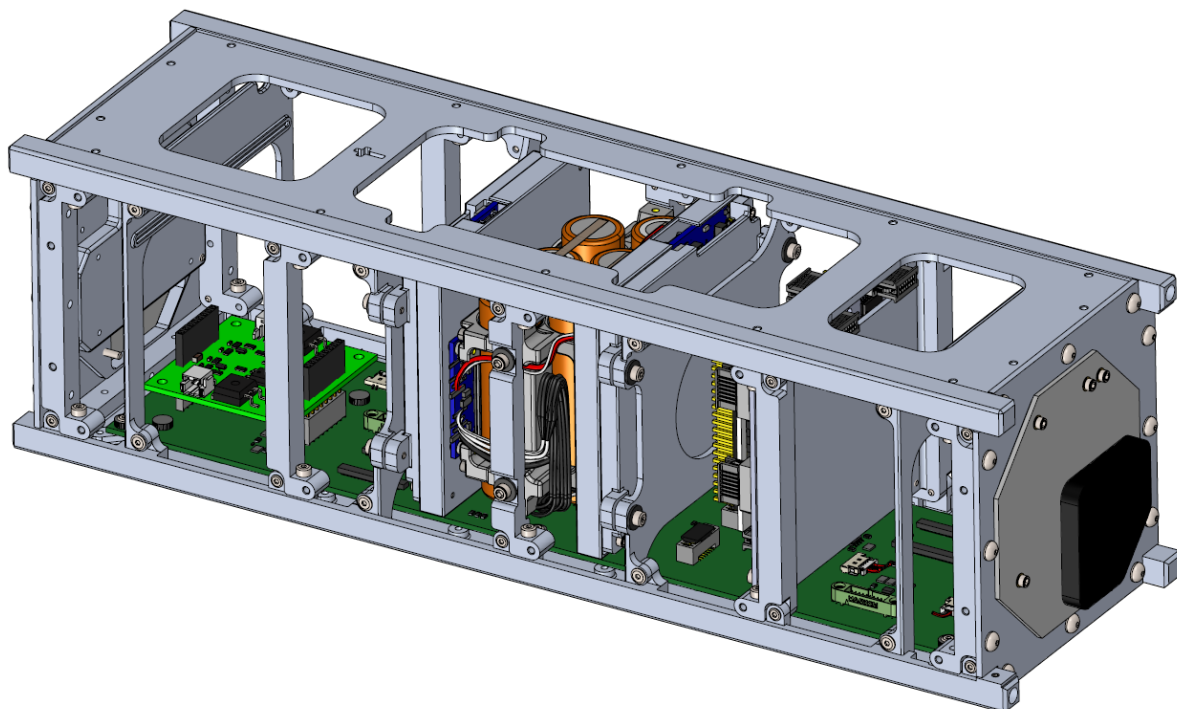This leads to the introduction of the third and final internal configuration.

Figure 3.52 Final internal configuration

As it can be seen from the picture above, the various subassemblies can be connected only to the $+X$ primary structure leaving the possibility of accessing the various components to carry out maintenance or cable management tasks, as expressed in the requirements.
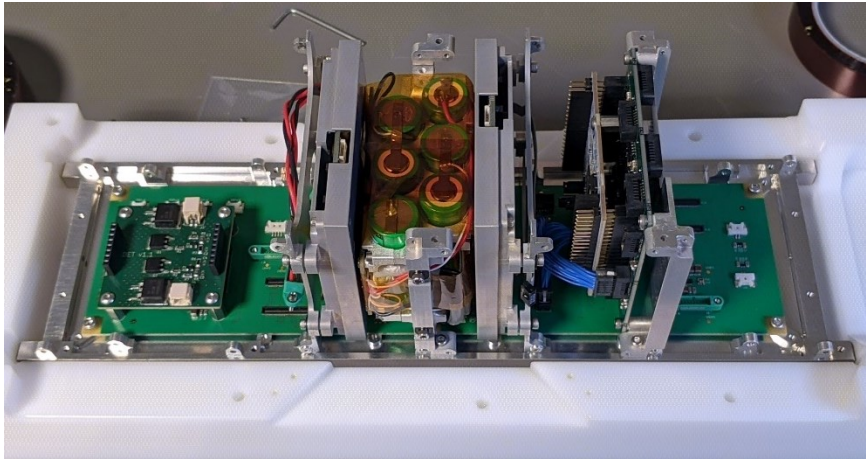

Figure 3.53 SPEISAT partially in the flatsat configuration

At this point, the remaining aspects that have yet to be analysed concern the harness and wiring which will be now discussed.

3.5.4   Harness

The screws topic doesn't require a deep analysis as the decisions regarding such aspect were taken keeping in mind the necessity of utilizing screws small enough to not require particularly large holes, but capable of sustaining the launch loads without breaking.

Moreover, another aspect which needed to be considered was the mechanical interference that could happen in certain situations. To avoid such an issue, in a couple of cases flat-headed or low-headed screws were chosen. For example, the formers have been used inside the spacecraft to connect the stiffeners with the primary structure's brackets while avoiding contact with the solar panels which were supposed to make contact with the stiffeners themselves, as shown in Figure 3.54. Another case concerns the screws used to assemble the CommSys subassemblies with the primary structures and the stiffeners. In this case it was required to prevent interference between the screws and the antennae during their deployment, therefore the low-headed ones were deemed as appropriate as they allowed the passing of the antennae while being available for screws of a bigger size.
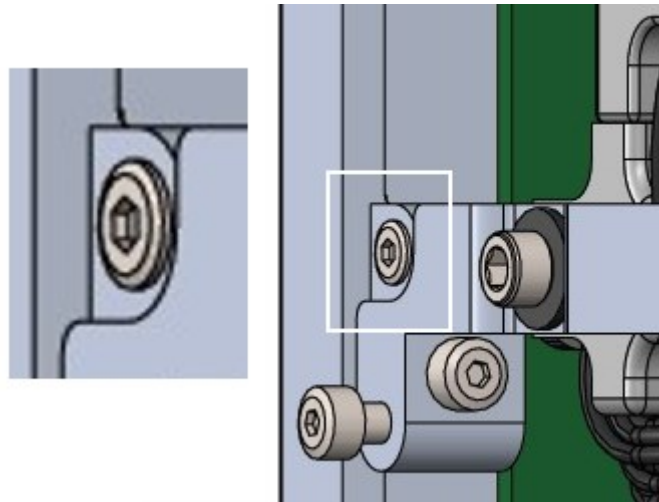
Figure 3.54 Flat-headed screws use

Therefore, with such premise, the choices fell on screws in the range from M2 to M3, all with the hexagon socket as the assembly and integration phase was carried out mainly using hex wrenches due to the difficult accessibility of certain areas.

Moving on to the wiring, in any space mission it's fundamental to keep the cables safe to avoid loss of functionalities from the satellite or, in the worst cases, the loss of the mission. Inside this project, in order to prevent any type of danger for the cables, the first that was done was in the design phase, when most of the structural elements have been thought with fillets to prevent cuts due to the sharp edges.

Moreover, it was necessary to keep the cables in a fixed position to avoid them oscillating due to the launch vibrations. The simplest solution was to use the Kapton, widely used in space missions, to stick them where they were deemed to be safe. To prevent the generation of oscillations, the boundary points were chosen pretty close between each other as the vibration frequency of a string under tension can be calculated as

$$ f = \frac{\sqrt{\frac{T}{m/L}}}{2L} \qquad\qquad [\,30\,] $$

Where L represents the string length between two boundary points.

However, it was deemed necessary to further protect these components, especially those that, due to their size and location, weren't possible to attach to structural elements as earlier explained. In this case it was decided to reinforce them using an aluminium adhesive tape in order to stiffen the cables, preventing them to vibrate and bend and, whether they were to collide with another internal component, to protect them.
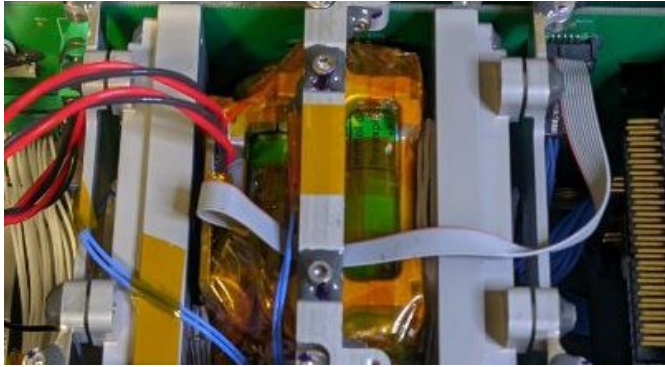
77

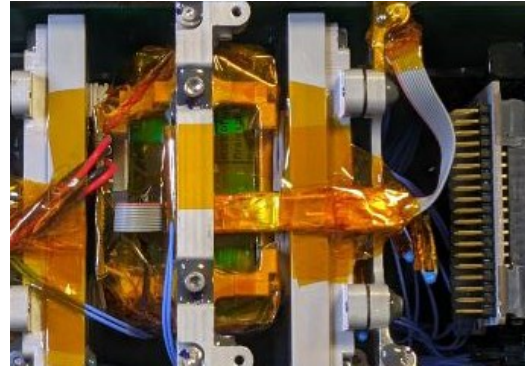*Figure 3.55 Battery data cable before cable management operations*

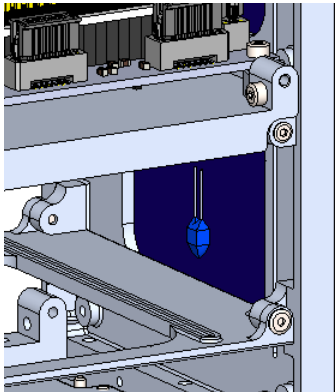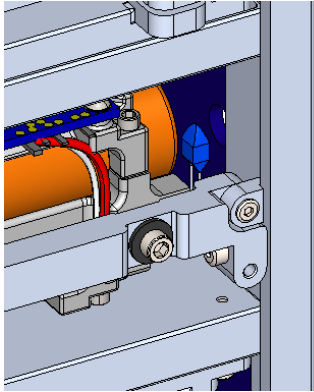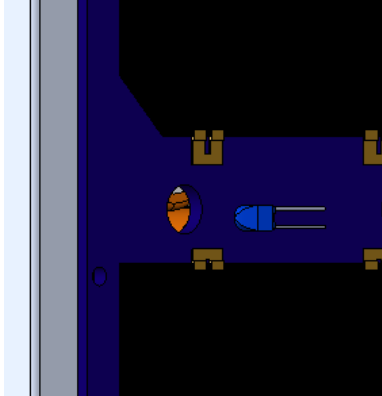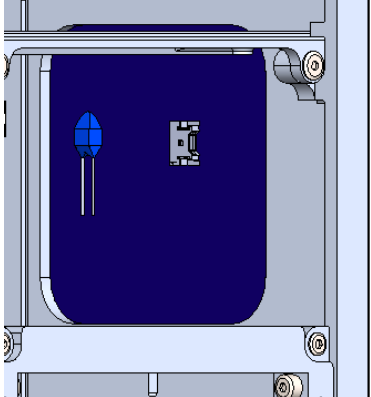*Figure 3.56 Battery data cable after cable management operations*

Figure 3.55 and Figure 3.56 offer and insight regarding the cable management performed on the battery pack data cable, considered one of the most important ones. As it was to pass below a stiffener, due to the fact that the solar panel was supposed to make contact with it, the cable was reinforced with the aluminium film in the parts corresponding to the structural element and the C&DH's case.
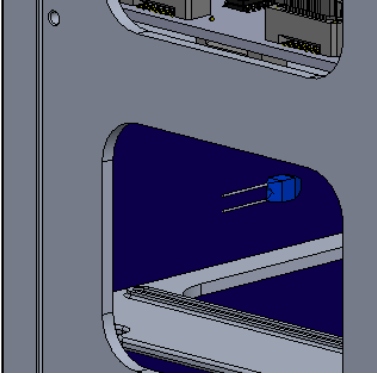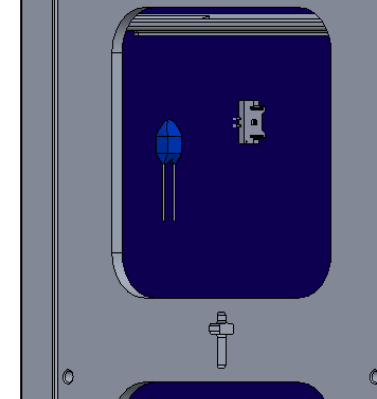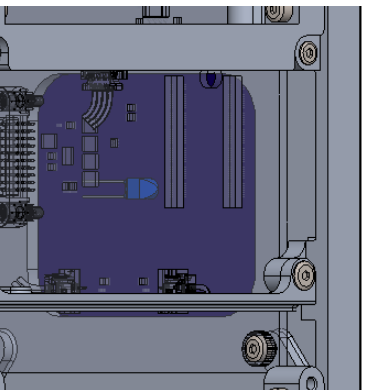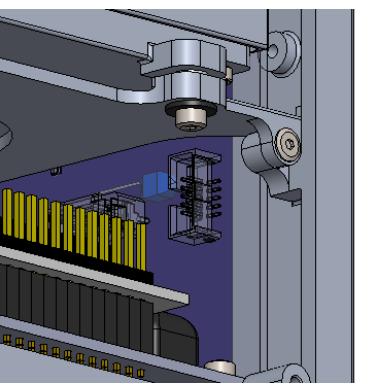
Moreover, to prevent the rubbing between the cable with other components, it was stuck to the case to prevent any movements. Finally, the structural components to which the cable makes contact with, are covered with Kapton as to prevent cuts do to the edges that remained sharp.
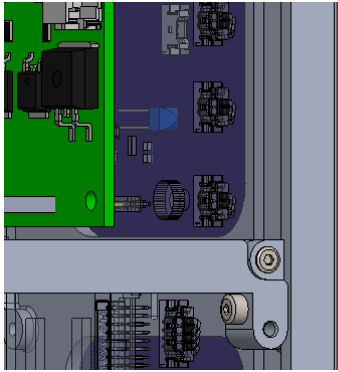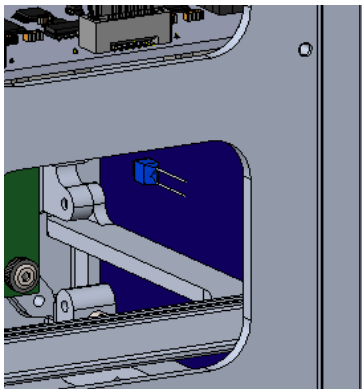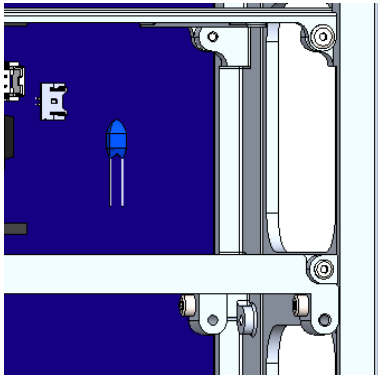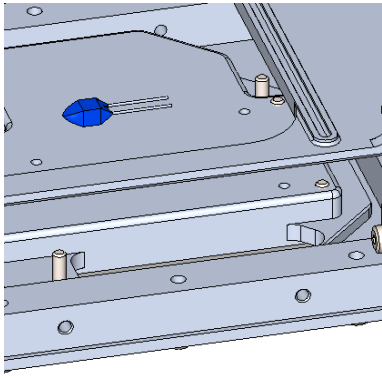
Besides the main cables connecting the components between each other, there were also the 30 smaller ones, used in the secondary mission to connect the sensing suite to the thermistors scattered inside the spacecraft, 2 of them were removed due problems incurred during the integration activity.
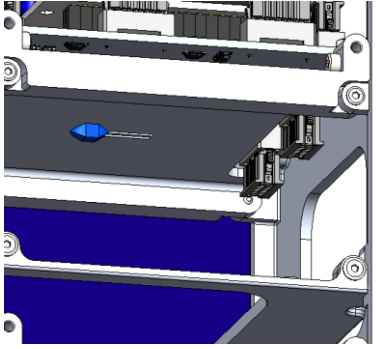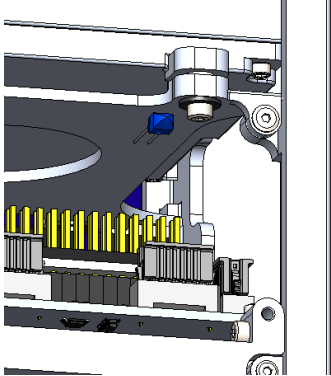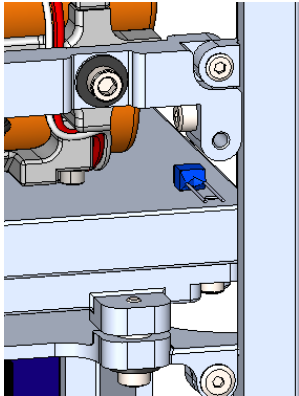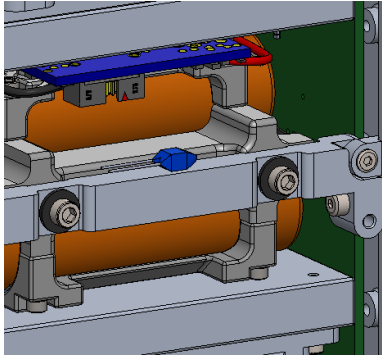
Due to their number, it was deeply inefficient to work on each of them individually. Therefore, the idea was to organize, when possible, the cables to form a skein, tying them together using the Kapton to later stick it where it was deemed safe, generally on the primary structure or the stiffeners, avoiding as well as possible the birth of vibrating phenomena which could lead to the damaging of the cables.
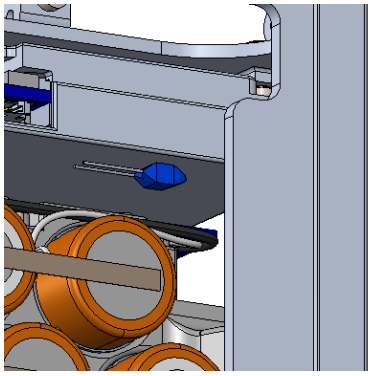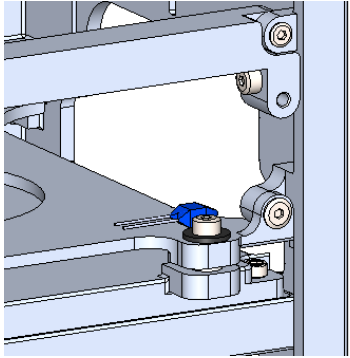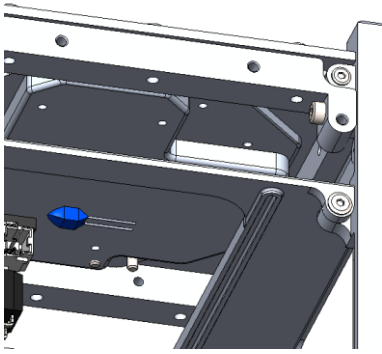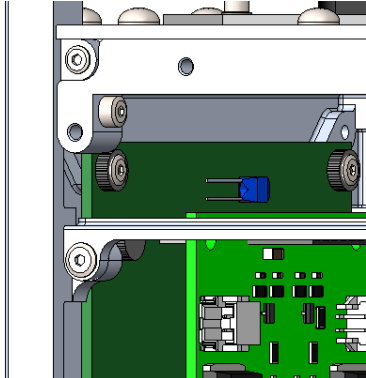
The following table provides an overview of the thermistors' location, as well as the sensing suite face on which the socket to which they were connected was located.
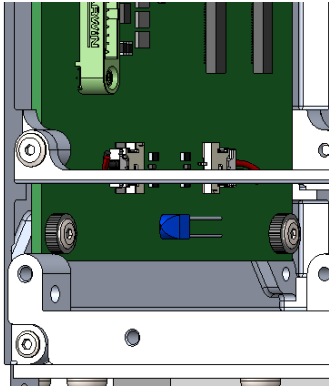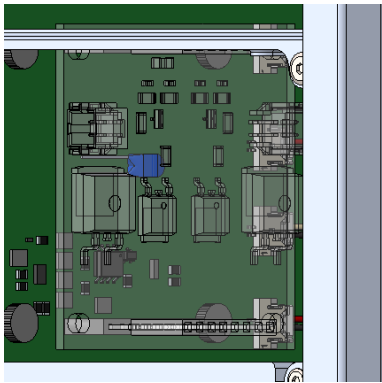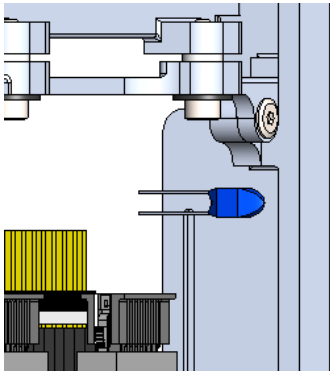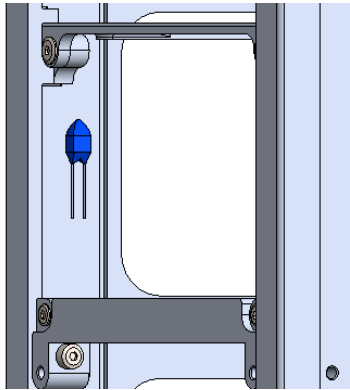
Name	Component attached to	Photo	Sensing suite face
Thermistor 1	$-X$ solar panel		$-Z$
Thermistor 2	$-X$ panel		$+Z$
Thermistor 3	$-X$ solar panel (outer face)		$+Z$
Thermistor 4	$-X$ solar panel		$+Z$
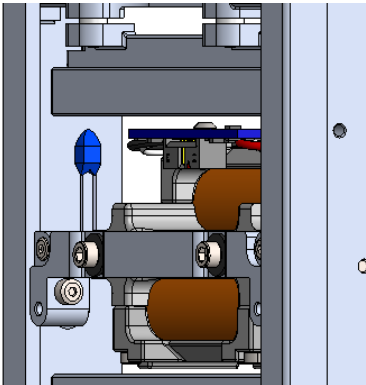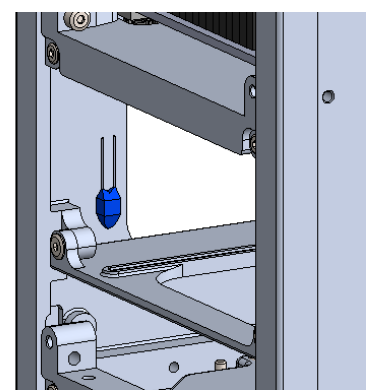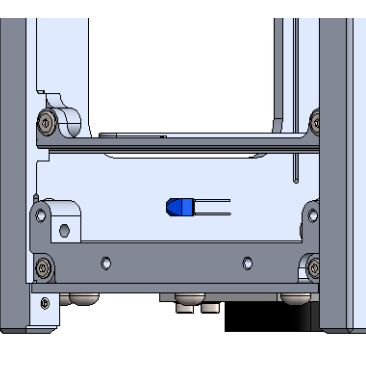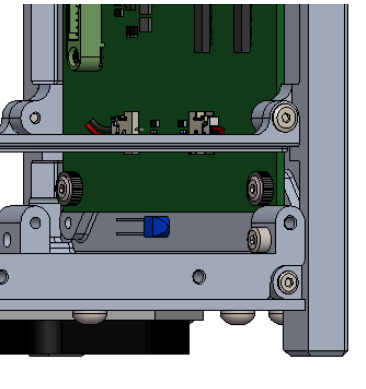
Thermistor 5	$+Y$ solar panel		$+Z$
Thermistor 6	$+Y$ solar panel		$+Z$
Thermistor 7	$+X$ solar panel		$+Z$
Thermistor 8	$+X$ solar panel		$+Z$

Thermistor 9	$+X$ solar panel		$+Z$
Thermistor 10	$-Y$ solar panel		$-Z$
Thermistor 11	$-Y$ solar panel		$+Z$
Thermistor 12	$-Z$ CommSys		$-Z$

Thermistor 13	Cross-stiffener		$-Z$
Thermistor 14	C&DH 1 cross-member		$+Z$
Thermistor 15	C&DH 1's case		$-Z$
Thermistor 16	Battery pack stiffener		$+Z$

Thermistor 17	C&DH 2's case		$+Z$
Thermistor 18	C&DH 2's cross-member		$+Z$
Thermistor 19	$+Z$ CommSys		$-Z$
Thermistor 20	Backplane		$+Z$

Thermistor 21	Backplane		$-Z$
Thermistor 22	DET		$+Z$
Thermistor 23	$-X$ primary structure		$-Z$
Thermistor 24	$-X$ primary structure		$+Z$

Thermistor 25	$-X$ primary structure		$-Z$
Thermistor 26	$-X$ primary structure		$-Z$
Thermistor 27	$-X$ primary structure		$-Z$
Thermistor 28	$+X$ primary structure		$-Z$
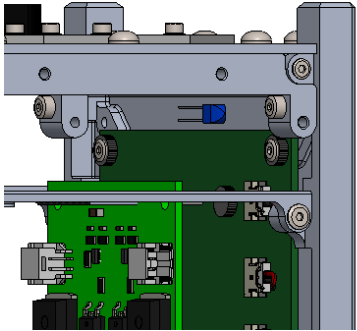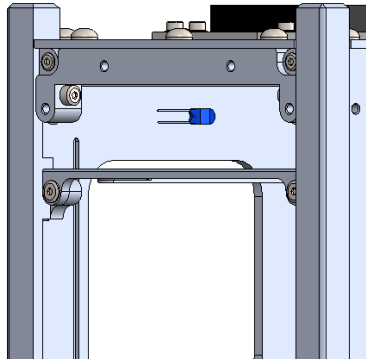
Thermistor 29	$+X$ primary structure		-Z
Thermistor 30	$-X$ primary structure		+Z

Table 3.13 Thermistors' location

The location of the thermistors has been decided in accordance with the thermal analyses results, identifying key points where the data collection would play a key role in validating the thermal model.

As an example, in order to assess the capabilities of the insulation system, one thermistor has been placed on the C&DH's case, directly in contact with the board, while a second one has been located on the cross-member part of the subassembly, downstream from the insulation system, thus thermally isolated from the board.

The following pictures provide an overview of the whole system, with the thermistors location inside the spacecraft.
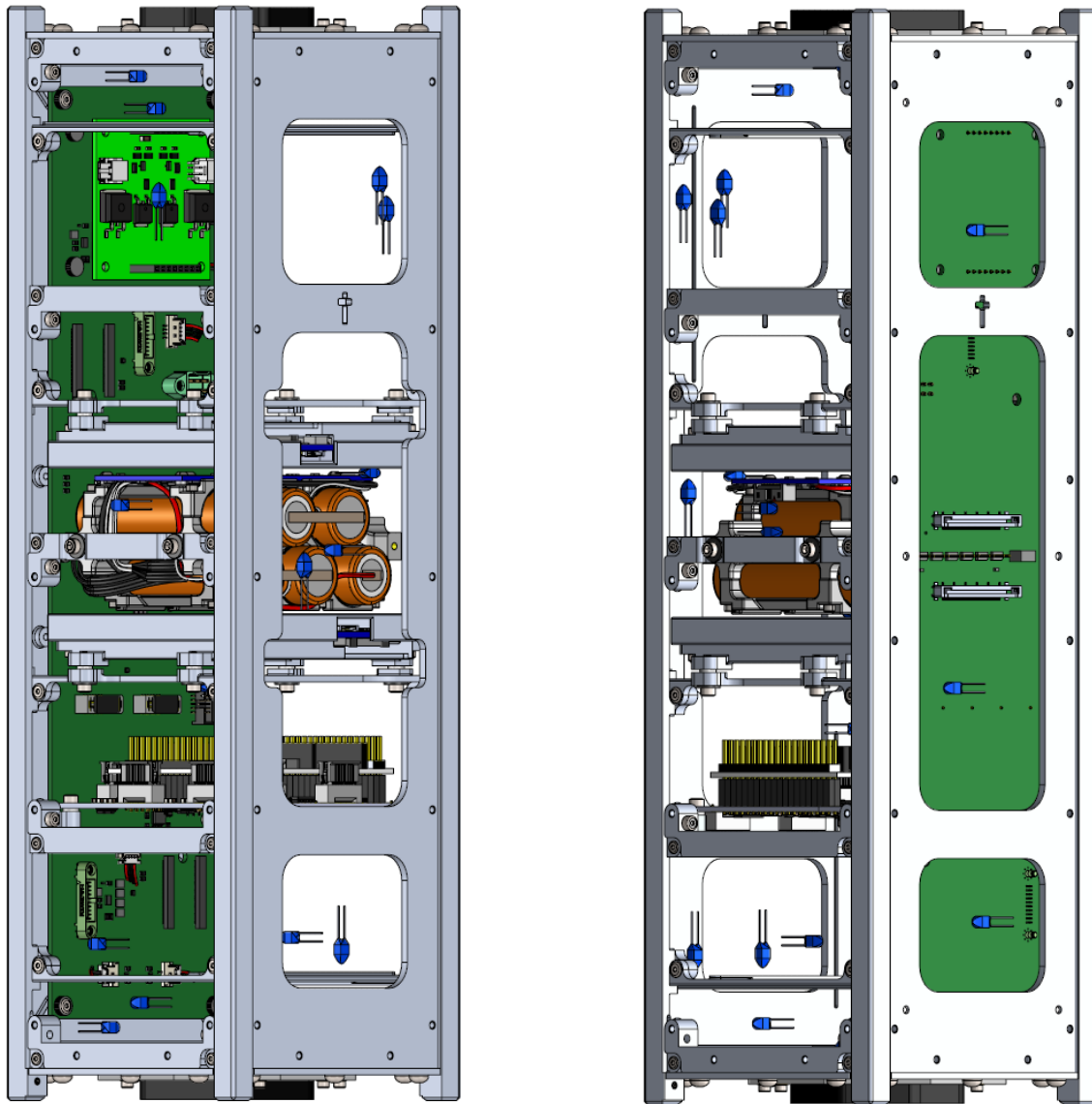
Figure 3.57 Thermistors' location overview

The cable management was conducted in the *Solidworks* environment to determine the best path for the cables as their number proved to be quite challenging. In this way it was possible to qualitatively calculate the cables' length as well as the correct socket in which each wire was supposed to be connected. The location of the thermistors was decided keeping in account first of all the temperatures which were to be monitored from an operational point of view, as to determine whether the battery was hot enough for example, but also to verify the thermal model developed in-house. The number of sockets played a major role too, as it was important to locate the thermistors in places where their cables couldn't entangle each other, making the assembly and integration phase more challenging.

Figure 3.58 Cables' sockets on the sensing suite

The result of such work can be seen from the following figures of the spacecraft already assembled and with the cable management fully completed.
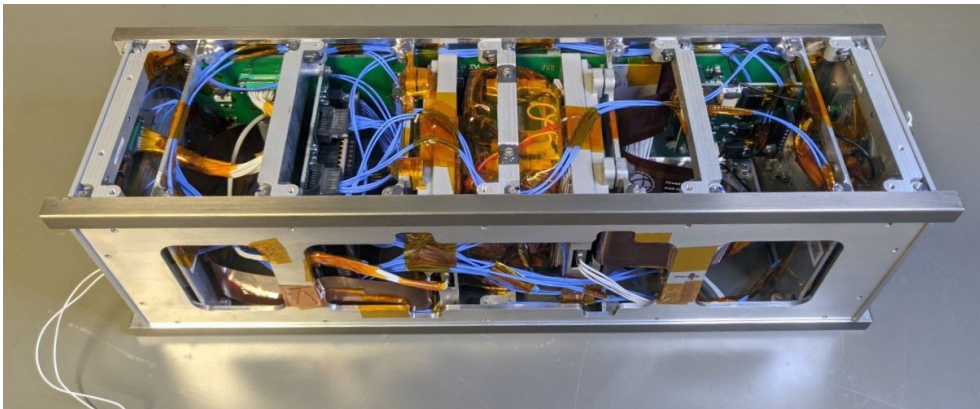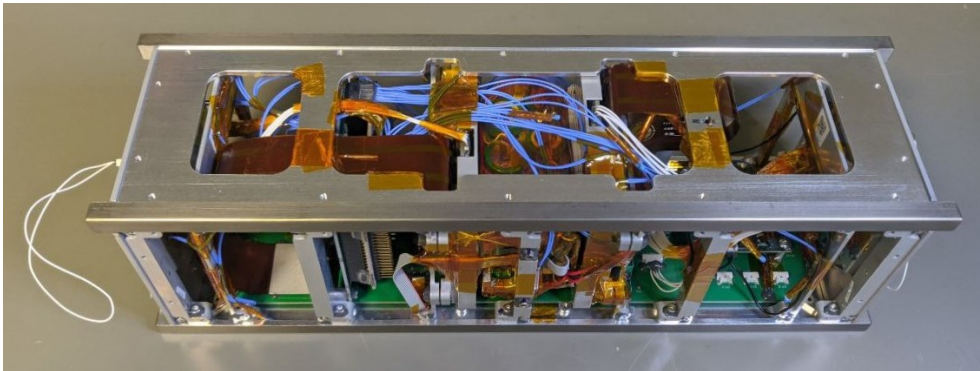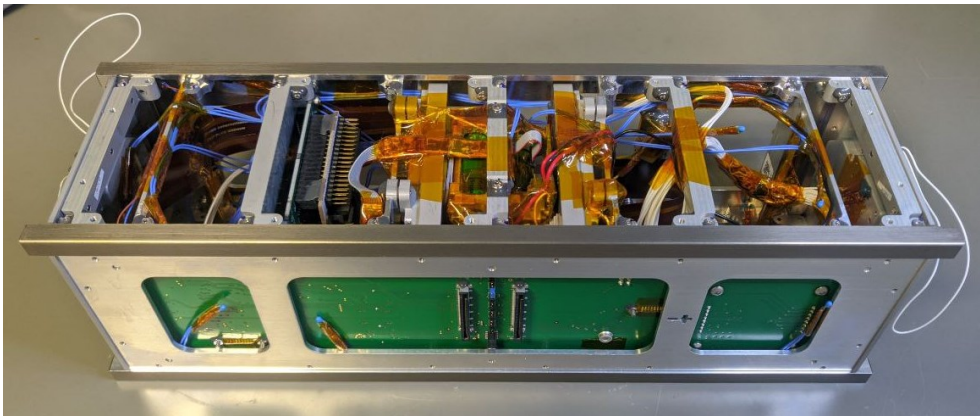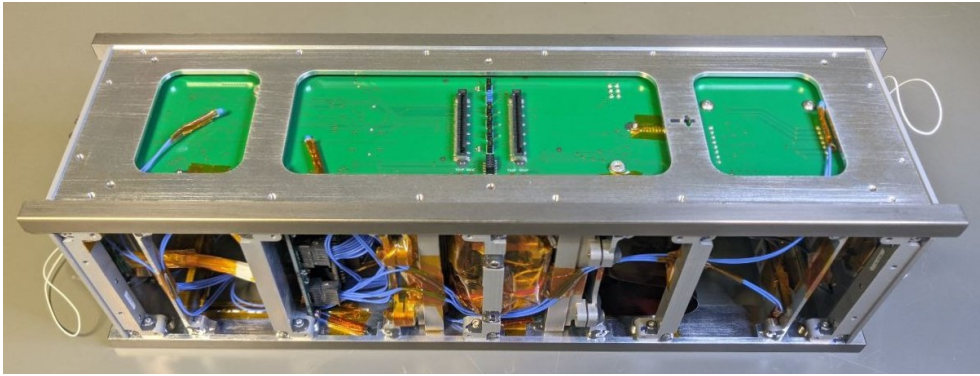
Figure 3.59 Thermistors' cable management

3.5.5 Magnets orientation

As mentioned before, the ACS of this spacecraft is a passive ones, based on permanent magnets and hysteresis rods. The former are used to allow the correct pointing of the spacecraft using Earth's magnetic field by generating a control torque. The latter, on the hand, serve their purpose mainly during the detumbling phase as their interaction with the geomagnetic field generates a damping torque that dissipates the spacecraft rotational kinetic energy. The evaluation of such method has been carried out through several analyses and the results provided by the sensing suite support such method.

While the hysteresis rods have a fixed position because of the cross-members in which they have to be inserted, this is not the case for the magnets. Through the analyses it came out that the best position for these components is near the spacecraft CoG. Therefore, it was decided to position them next to the battery pack.

The last aspect to take care of was the orientation of the magnets. The decision that was made was mainly dictated by the system architecture on a software level. As mentioned in 3.4.1, one C&DH is master of the other, therefore it was decided to make that the face mostly pointed towards the Earth's surface is the one hosting the CommSys connected to the master C&DH, or C&DH 1, as the telemetry received from such board were to contain more data.

3.5.6 Surface treatments

As it could be seen from Figure 3.59, the spacecraft's rails have a different colour from the rest of the structure. This is because of the surface treatments to which the structure has been subjected.

In particular, the rails received a hard anodization treatment while the rest of the structure a SurTec 650 one.
The former is vastly used in the space field, since it is required from almost every launch company, as it can be seen from the SPEI-SYS-042 requirement. The process is based on a reaction which allows to increase the thickness of the oxide layer on metal part, which naturally is very thin. The component is immersed in a 20% sulphuric acid solution, which acts

as an electrolyte, and it behaves as the cathode on an electrolyte cell. Through the application of a current, oxygen ions develop on the surface of the treated part, combining with the aluminium atoms. This combination leads to the formation of a hard and compact layer of aluminium which offers several properties useful in space missions:

- Corrosion resistance
- Wear resistance
- Hardness
- Dielectric insulation
- Cold welding prevention

Moreover, the SurTec 650 treatment is an electroplating technique used to cover the aluminium with a thin layer of passivation increasing its corrosion resistance.

Figure 3.60 offers an overview regarding the surface treatment performed on the primary structure $+X$. The color yellow highlights the areas where the hard anodization is required while the rest shall be subjected to the SurTec 650 treatment.
In the specific, the request for the hard anodization was done in accordance with the military specification as in MIL-A-8625 [22], therefore demanding a type 3 (hard) and class 2 (coloured) anodization.

- YELLOW ZONE: ANODIZATION ACCORDING TO MIL-A-8625, TYPE 3, CLASS 1
- REMAINING ZONES: SURTEC 650
- COMPLETE PROTECTION OF ALL HOLES FOR ALL TREATMENTS
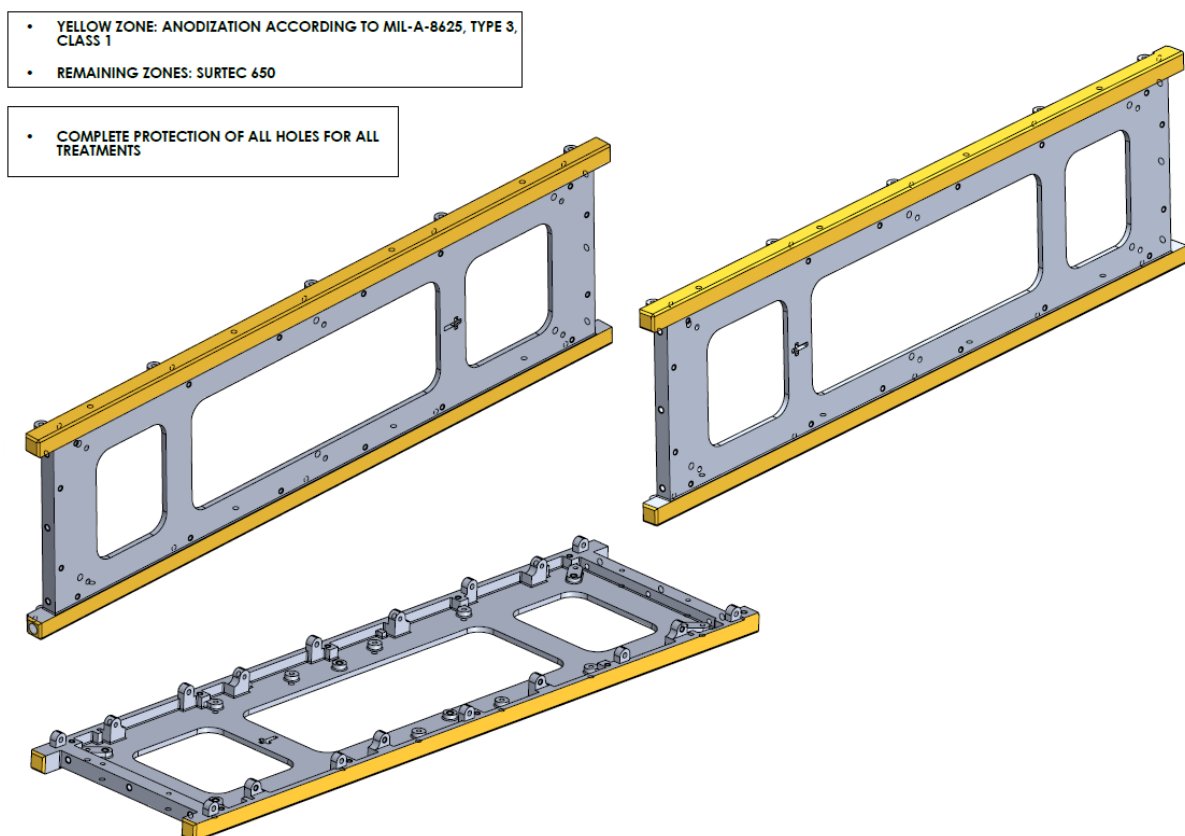
Figure 3.60 Surface treatment sheet

Regarding the note "Complete protection of all holes for all the treatments" voice, this was done as the hard anodization treatment increases the thickness of the components relatively

by a lot, therefore there would have been interference problems between the holes and the screws if the protection hadn't been applied. In fact, as it can be seen from the figure above, such treatment has been conducted only on the external faces of the rails, as to prevent possible interferences between the various structural components. However, the remaining faces were subjected to the SurTec 650 treatment as it doesn't produce a particularly thick layer therefore it wouldn't have compromised the tolerances. Still, the holes protection was requested as a safety measure.

Obviously, the carrying out of such treatment needs to be done with the best safety measures as even the smallest damages to the structure could compromise the components quality. This is especially true for the rails as even scratches would make them flight non-compliant,

To sum up, the full structure, realized in aluminium alloy Al-7075, was subjected to a superficial treatment to boost its properties, making it compliant with the requirements provided by the launch company, and enhancing its performances, thus preventing possible failure or degradation in the space environment.

3.5.7   Mass and volume budgets

With the completion of the description of the final structural design and configuration, it's useful to provide an overview of the system which can be done through the system budgeting, a fundamental tool in system engineering.

In particular, in the topic of this thesis, this can be done through the draft of the mass and volume ones, without covering the power and link budgets.
Starting from the mass one, it allows to determine how the complete weight of the spacecraft is distributed among its components with a different degree of detailing. The volume budget, on the other hand offers a summary of how the satellite internal space is occupied.

3.5.7.1 Mass budget
The mass budget can be defined using both the singular components and the subsystems to have a clearer overview of the most impactful in terms of mass.

It should be reminded that even though the CDS specifies that the maximum allowed mass of the spacecraft should be 6 kg, as a system requirement, the spacecraft mass cannot go above 2.93 kg, due to the DMM mass used in the test campaign by D-Orbit. Therefore, the margin has been calculated keeping in account such value.

Component	Subsystem	Quantity	Unit mass [g]	Total mass [g]
+X Primary structure	Structure	1	223.25	223.25
-X Primary structure	Structure	1	217.75	217.75
Stiffener	Structure	6	16.33	97.98
Battery stiffener	Structure	2	11.98	23.96
C&DH's Cross-member	Structure	2	28.14	56.28
Hysteresis rods' cross-member	Structure	2	19.83	39.66
C&DH's case	Structure	2	38.28	76.56
C&DH's cover	Structure	2	37.52	75.04
Cross-stiffener	Structure	1	68.43	68.43
Z skin	Structure	2	59.09	118.18
Antenna	Communication System	2	18.00	36.00
CommSys board	Communication System	2	30.79	61.58
UHF Transceiver	Communication System	2	20.23	40.46
C&DH Board	Command & Data Handling System	2	51.08	102.16
Backplane	Command & Data Handling System	1	100.00	100.00
Sensing suite board	Sensing Suite	1	76.13	76.13
Thermistor	Sensing Suite	30	0.11	3.30
Permanent magnet	Attitude Control System	2	1.00	2.00
Hysteresis rods	Attitude Control System	6	0.65	3.92
Solar panel	Electrical Power System	4	149.50	598.00
Battery pack	Electrical Power System	1	454.00	454.00
DET board	Electrical Power System	1	15.00	15.00
Deployment switch	Electrical Power System	2	2.00	4.00
Nanobook	Payload	1	1.00	1.00
Harness	-	-	-	193.51
Total				2688.15
Margin				241.85

Table 3.14 Mass budget

As it can be seen by the positive margin the mass safely remains below the limit imposed by the DMM mass.

The following representation provides a summary of the distribution of mass among the different subsystems.
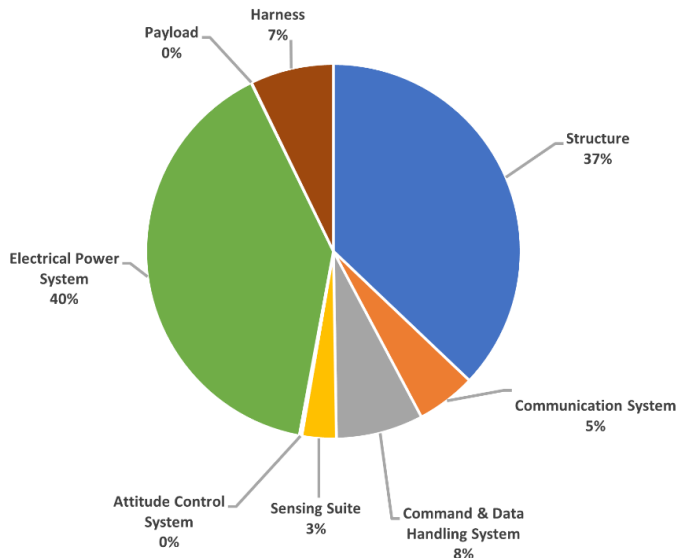
Figure 3.61 Mass distribution among the subsystems

Subsystem	Total mass [g]
Structure	997.09
Communication System	138.04
Command & Data Handling System	202.16
Sensing Suite	79.43
Attitude Control System	5.92
Electrical Power System	1071
Payload	1
Harness	193.51

Table 3.15 Total mass of the subsystems

3.5.7.2 Volume budget

The volume budget has been performed using as unit of measure the CubeSat unit, to provide a better understanding of the space occupied. Moreover, in this case, for simplicity's sake, the volume budget will be discussed using the subassemblies whenever possible, as they allow to better determine the space occupied by the different components.

As a reminder, the CubeSat unit, is represented by a 100x100x113.5 mm "cube", therefore it's safe to assume that the volume inside the spacecraft available for the various subsystems, may be around 97x97x97 mm. Thus, excluding the thickness of the structure and the rails' standoffs. In particular, the latter measure has been considered during the drafting of the following budget.

Subassembly	Quantity	Unit volume	Total volume
Battery pack	1	0.33U	0.33U
Sensing suite	1	0.35U	0.35U
C&DH	2	0.28U	0.56U
CommSys	2	0.08U	0.16U
Component	Quantity	Unit volume	Total volume
DET + connectors	1	0.07U	0.07U
Backplane + spacers	1	0.14U	0.14U
Hysteresis rods' cross-member	2	0.06U	0.12U
Total			1.73U
Margin			1.27U

Table 3.16 Volume budget

Even though the results from Table 3.16 may lead to think that a 2U CubeSat could have been enough for this mission, that's not the case at all. In fact, the system presented several cables which needed to follow specific paths to prevent damages. This contributed to the taking up of the remaining empty spaces, filling completely the spacecraft. As it could be seen from Figure 3.59.

Moreover, all the subsystems had to interface with the backplane, therefore it was necessary to provide an adequate area to place all the connectors, where possible, or to directly mount the components, as in the DET case. Such thing would have been impossible with a smaller backplane, as even the 3U one, as incredibly dense.

As it was done for the previous budget, it possible to represent the volume occupied by the subassemblies and components through a chart to provide a better understanding of the space division.
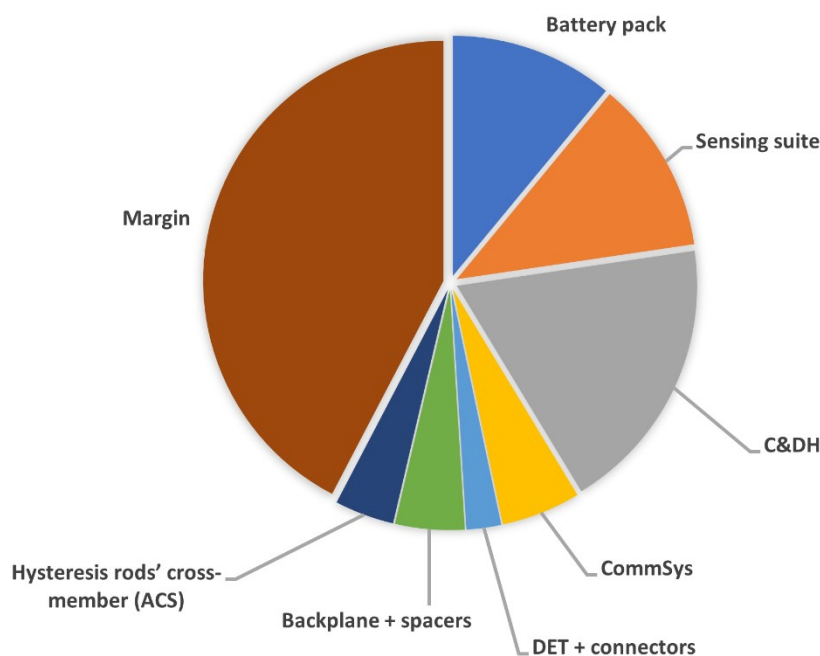
Figure 3.62 Volume distribution among the subassemblies and components

With the drafting of the budgets, the design phase is concluded and it's possible to move on to the validation and testing one. The assembly and integration won't be covered in this thesis, but an example of an AIV&T activity will be later presented as to provide a design assessment.
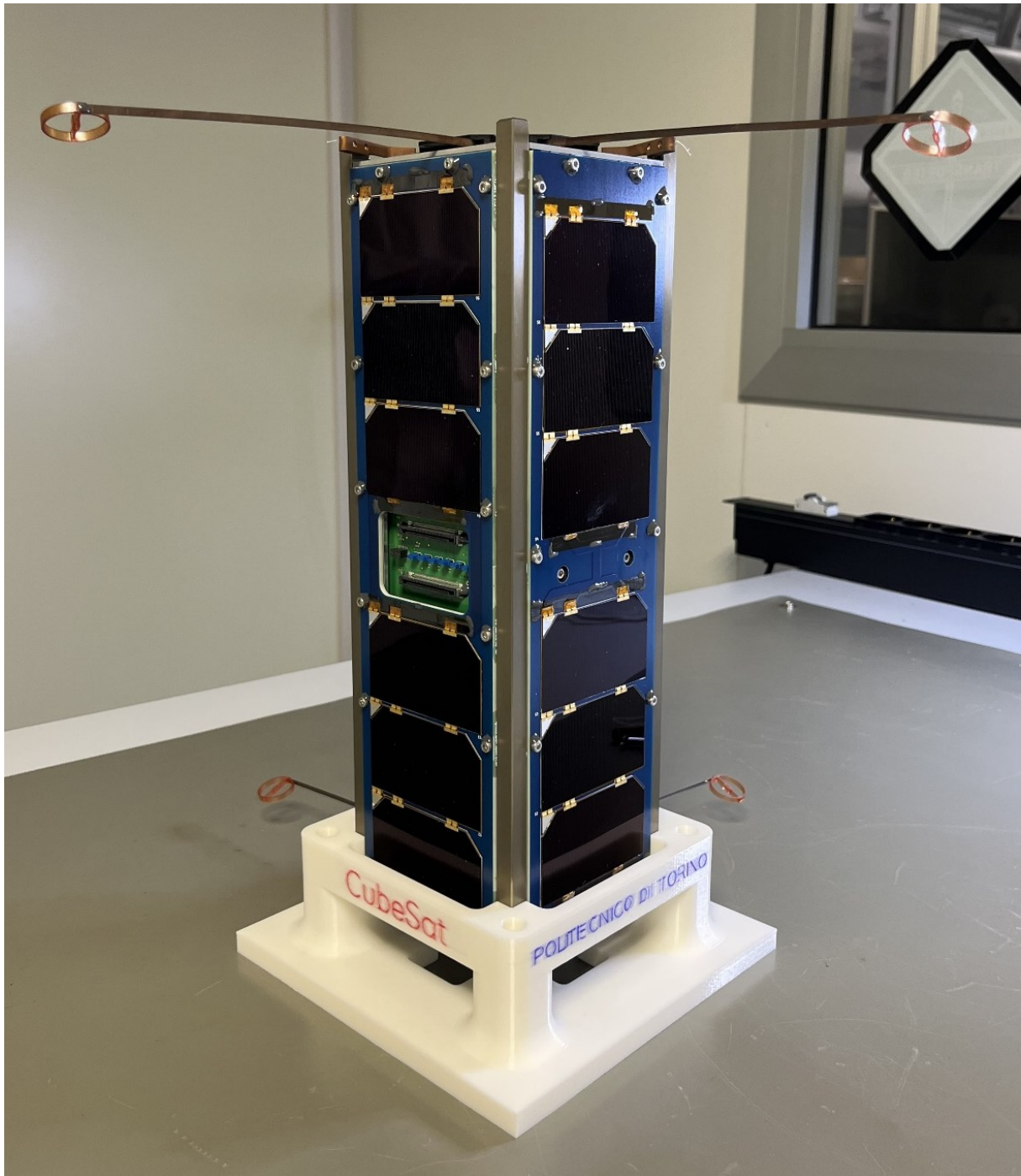
Figure 3.63 SPEISAT completely assembled

4 Structural Analyses

The following chapter sets out the FEA conducted to validate the model realized in the design phase, evaluating the spacecraft response in the launch environment. Moreover, this allowed to have a first glance at results that could be expected to obtain during the environmental testing.

4.1 Model creation

As it was mentioned in 2.2.1 there are two different way of developing the Finite Element model. In this paragraph the creation of the mathematical model will be discussed, analysing the various steps leading to the final product.

4.1.1 Geometrical model

The FEA were devised using *MSC Apex* as the pre-processing environment. This software was deemed as the best for this goal, especially considering that the analyses were to be conducted with *MSC Patran & Nastran*, therefore it was considered best to work with software part of the same suite.

Therefore, the general workflow can be summarised as follows.

Figure 4.1 FEA workflow

Moreover, in order to avoid extremely complicated meshes that would have greatly increased the computational cost, it was necessary to recreate the various subsystems using mock-up models realized with simple geometries.

Therefore, from the final configuration model, only the structure was exported to be further worked on, producing representations of the subsystems.
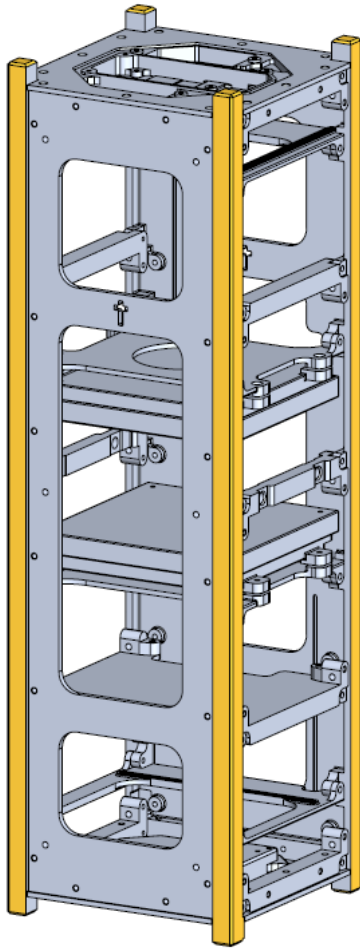
Figure 4.2 Structural model
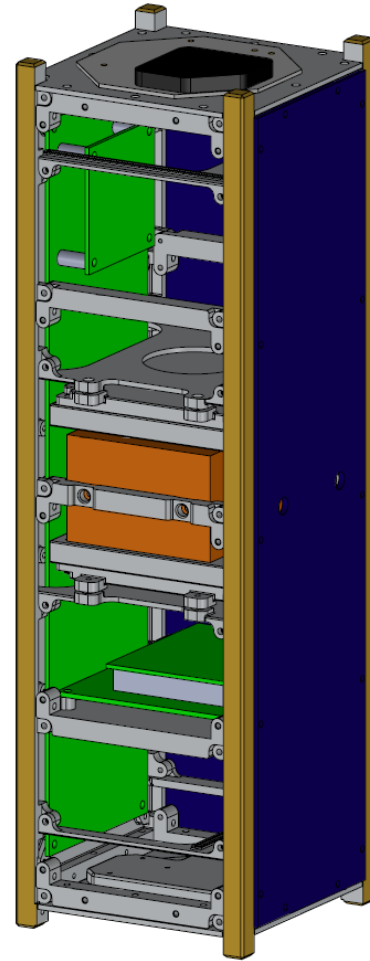
Figure 4.3 Structural model with mock-ups

It needs to be noted that all the screws have not been exported due to the fact that they'll be directly generated in the Finite Element Model using rigid connectors, as it will be later seen.

4.1.2   Finite Element Model creation

The creation of the Parasolid model generated in the *Solidworks* environment leads to the possibility of importing it into *MSC Apex* to proceed with the assignation of the material properties, as well as the realization of the mesh and the creation of the connectors. The activity of pre-processing was mainly carried out using the abovementioned software, while the analyses were set up in *MSC Patran* to use *MSC Nastran* as the solver.

Therefore, the allocation of the material properties plays a major role in the FEM as it will greatly affect the results obtained, and it the first task that needs to be performed in the *MSC Apex* environment.
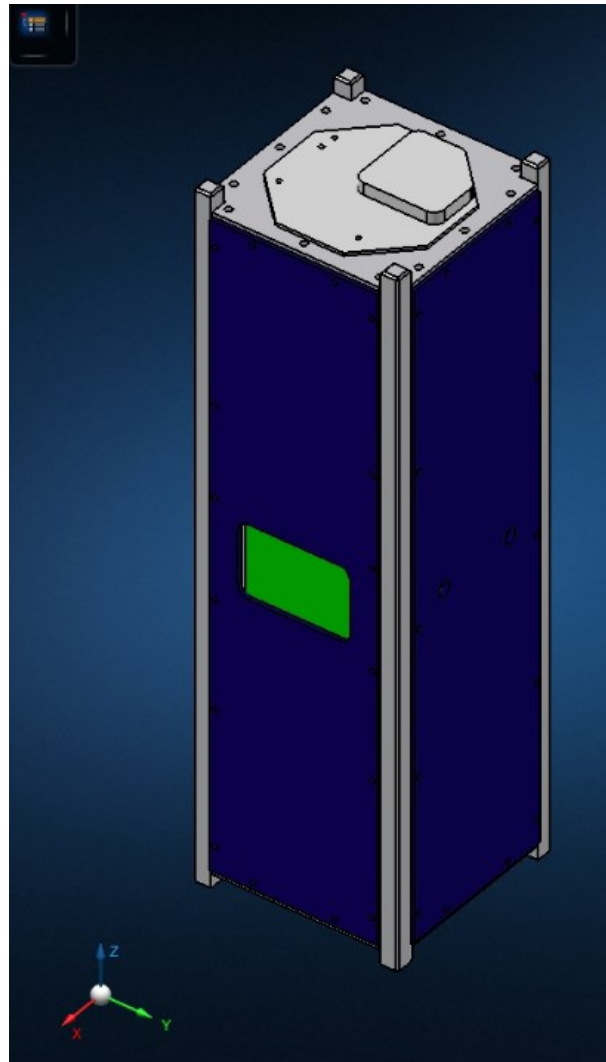
Figure 4.4 Geometrical model in MSC Apex

The first material to be created is the aluminium 7075 of the structure with the following properties:

Aluminium 7075	
Constitutive model	Isotropic (MAT1)
E	71.7 GPa
G	26.9 GPa
ν	0.33
ρ	2810 kg/m^3

Table 4.1 Al-7075 properties in model

Secondly, it needs to be created an appropriate material to correctly simulate the various boards contained in the spacecraft, as well as the boards of the solar panel. For this purpose, it was decided to use the FR4, a composite material made of a woven pre-preg fiberglass cloth with an epoxy resin matrix widely used for printed circuits.

FR4	
Constitutive model	Isotropic (MAT1)
E	24.6 GPa
G	10.83 GPa
ν	0.136
ρ	1900 kg/m^3

Table 4.2 FR4 properties in model

Moreover, it's necessary to define the PTFE to correctly reproduce the washers used to distance the C&DHs' cases from the dedicated cross-members.

PTFE	
Constitutive model	Isotropic (MAT1)
E	0.5 GPa
G	0.17 GPa
ν	0.45
ρ	2140 kg/m^3

Table 4.3 PTFE properties in model

Lastly, the material of the antennae's case needs to be defined, which is Delrin.

Delrin	
Constitutive model	Isotropic (MAT1)
E	9.35 GPa
G	3.45 GPa
ν	0.355
ρ	1400 kg/m^3

Table 4.4 Delrin properties in model

At this, point the only component whose material has not been defined is the battery pack. Due to its mechanical properties, it certainly doesn't have natural frequencies lower than those of a board, and it's neither particularly subjected to deformations. Due to these aspects, it was decided to reproduce the battery pack as a mere mock-up model, using a fictitious material to simulate its mass, while maintaining the body incredibly stiff. Therefore, the mechanical properties have been considered as equal to those of the aluminium but with a different density, calculated keeping in account the mass of the component and the volume of the mock-up counterpart.

Battery pack material	
Constitutive model	Isotropic (MAT1)
E	71.7 GPa
G	26.9 GPa
ν	0.33
ρ	2000 kg/m^3

Table 4.5 Battery pack material properties in model

The realization of the mesh has been done using a solid mesh automatically generated by the program composed of TET4 elements. In order to maintain a good quality of the mesh without compromising the analyses with an excessively dense mesh, it was decided to realize elements of 4 mm, resulting in 198876 nodes and 742407 elements. Such output was obtained after a series of iterations with the trial-and-error method in order to obtain a model compatible with the hardware available.

In fact in several cases the model resulted to the require an excessive computational costs, causing either the solver to crash or to close the process due to memory termination. A third failure which occurred was a resulting .xdb file too big therefore impossible to produce without an adequate system. For the last problem a series of *Nastran* commands had been tried to force the production of a bigger file without encountering any success.

Table 4.6 shows the resulting mesh quality based on the process run inside the *MSC Apex* environment.

Method / Quality	Jacobian	Aspect Ratio
INVALID	0	0
BAD	0	3253
POOR	0	77938
GOOD	742407	661216

Table 4.6 Mesh quality

The Jacobian check evaluates the deviation of the element shape from an ideally shaped element, calculated as if it had straight edges with equal length. An ideally shaped element has a Jacobian ratio of 1, with a value below 40 being generally accepted, and the mid-side nodes are located exactly at the middle of the straight edge.

On the other hand the aspect ratio evaluates the mesh quality through the length of the element's sides, which need to have the same value.

The following pictures shows the resulting mesh.
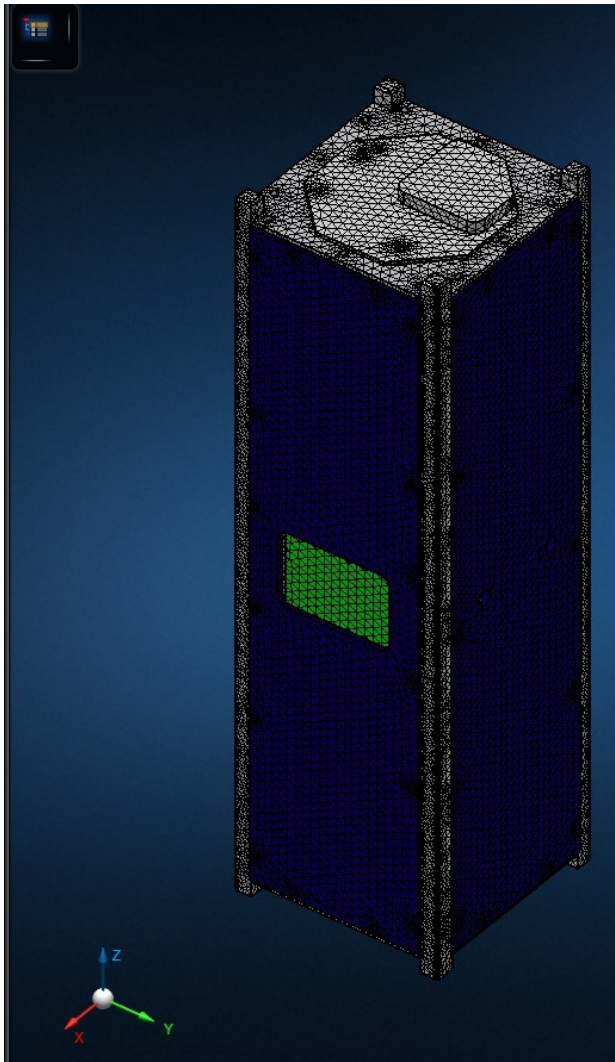
Figure 4.5 Model's mesh
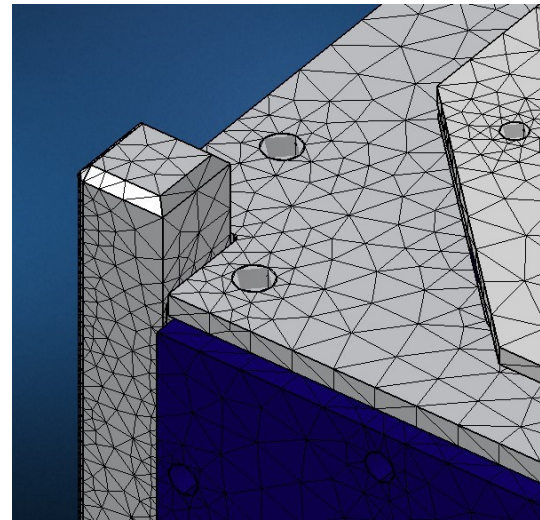
Figure 4.6 Model's mesh zoom

Moreover, as mentioned before, the modelling of the screws was done through the generation of connectors using the mesh nodes as its edges. Such connections have been later translated into RBAR elements to pass the file to *MSC Patran*.
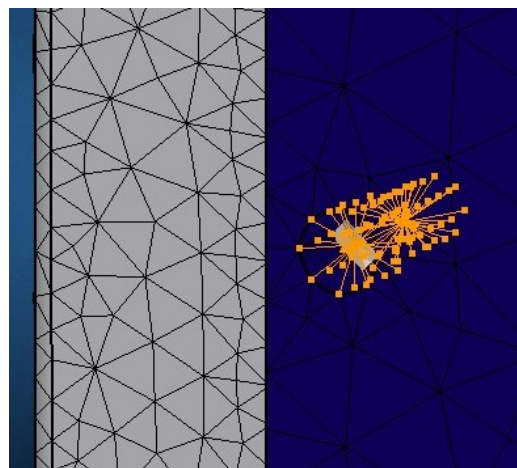
Figure 4.7 Connectors example

The allocation of the properties has been done through the assignation of the materials to the various components of the spacecraft.

Finally, in the *MSC Apex* environment the last thing modelled are the boundary conditions, in particular the constraints, which have been modelled through a fixture located at the end of the rails standoffs. Those on the $-Z$ face were used to model the plate positioned above the spring used to push the spacecraft outside the deployer, while the others were supposed to represent the plate in charge of closing the deployer.
The contacts between the rails and the test-pod, or deployer, weren't modelled for a mere aspect of state-of-the-art as there has been a tendency of modelling only the contacts at the ends of the rails standoffs.

Finally, the external loads weren't modelled inside this environment as the analyses setup was to be completed in *MSC Patran* and the loads themselves characterize the type of analysis performed. Moreover, a specific analysis can only be modelled in the latter software, therefore for the sake of consistency, all analyses have been setup in it.
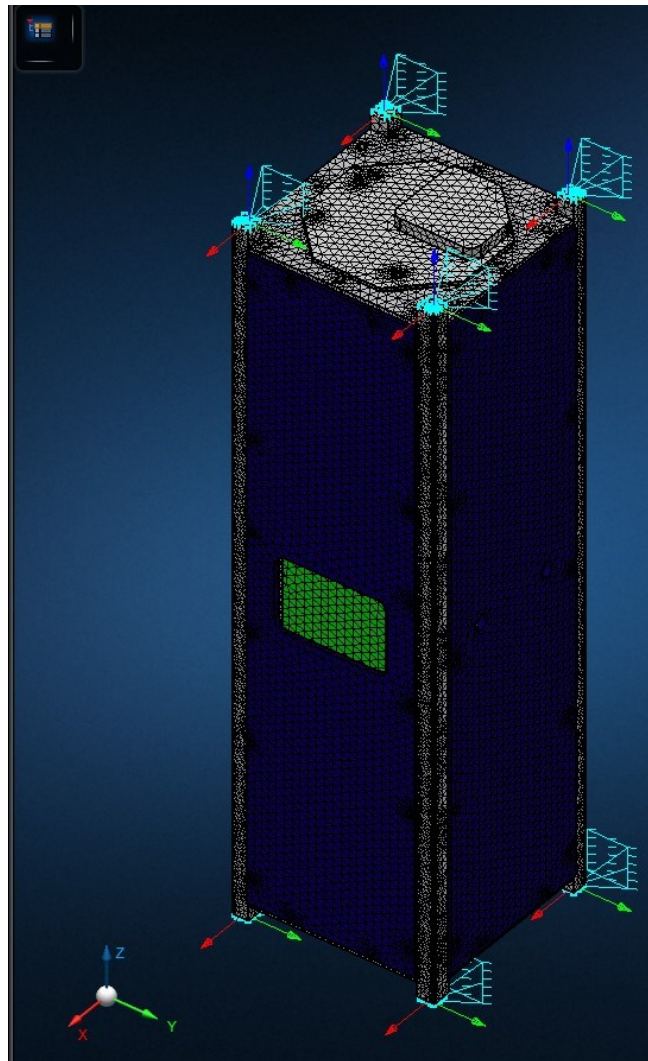
Figure 4.8 Model with constraints

The completion of the model in *MSC Apex* allow to proceed with the importing of the mathematical model in the *MSC Patran* environment through the generation of a *Nastran* input file (.bdf).

In the new software the main activity involved the characterization of the loads, as well as the definition of the solution type from the analyses and the output requested.
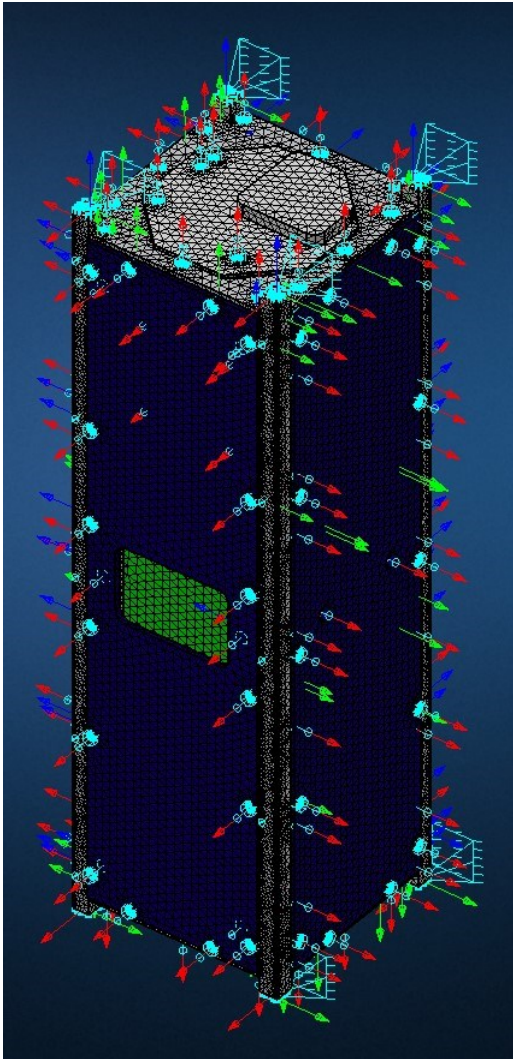
Figure 4.9 Model in MSC Apex
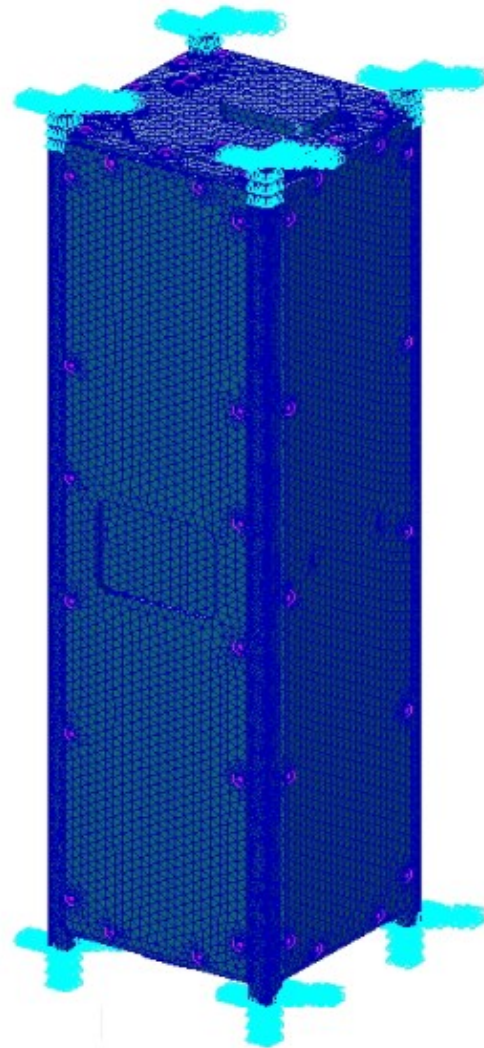
Figure 4.10 Model in MSC Patran

4.2   Analyses performed

The switch to *MSC Patran* allowed to proceed with the competition of the definition of the boundary conditions, making it possible to start the FEA described below.

4.2.1 Static analysis

The static analysis wasn't mandatory, but it was decided to perform it anyway as it provides a first overview of the spacecraft response to the launch environment.

In this case the environment was simulated using an inertial load, using the values provided in the *Rideshare Payload User's Guide*, already reported in Table 3.2.

It needs to be noted that these load factors could only be applied one at a time, not simultaneously. Therefore, three different scenarios could be modelled keeping in account the values provided.

Scenario	Axial X_{PL}	Lateral Y_{PL}	Lateral Z_{PL}
1	7.4	0.0	0.0
2	0.0	12.9	0.0
3	0.0	0.0	12.9

Table 4.7 Static analysis scenario

The loads where simulated through the implementation of three different inertial loads, used in different loads cases to distinguish the various scenario.

As it can be seen from Table 4.7 the axes doesn't refer necessarily to the ones of the spacecraft, therefore, it's necessary to convert the reference frame in order to pass from the launcher to the satellite one.
To better understand this problem it's necessary to introduce the various reference frames, already seen in 3.2.2.

1. **LV integration axes:** Refers to the launch vehicle reference frame, in particular it's defined corresponding with the O-ring, to which the carrier was to be integrated.
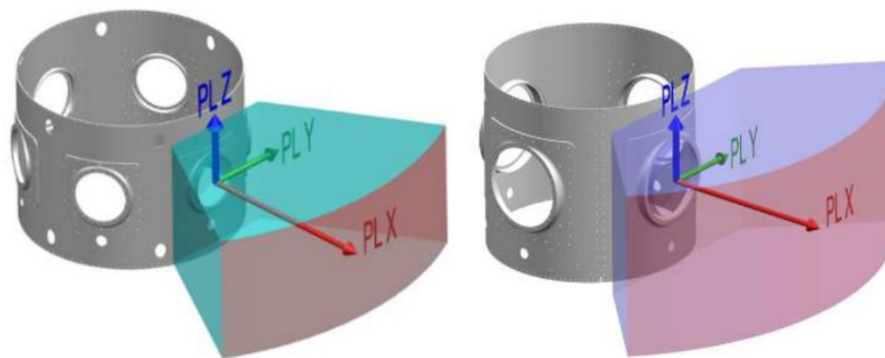

Figure 4.11 LV integration axes

2. **ION axes:** This system refers to the D-Orbit's carrier.
3. **Astrofein axes:** This system refers to the deployer mounted on the carrier.
4. **CubeSat axes:** The last system refers to the CubeSat.

Being the relationship between the reference frame fixed it's possible to perform a conversion to determine which spacecraft axes will correspond to the LV ones.

LV integration axis		ION-mk02 axis		Deployer		SPEISAT
PL Z	--->	X AXIS	--->	X AXIS	--->	X AXIS
PL Y	--->	Y AXIS	--->	Y AXIS	--->	Y AXIS
PL X	--->	Z AXIS	--->	Z AXIS	--->	Z AXIS

Table 4.8 Reference frames conversion

Moreover, to further increase the models' validity, it was decided to integrate the simulation of the contacts between the CommSys board and the relative support, as to prevent the generation of interference.

The following images represent the results achieved from these analyses in terms of displacement and stress tensor using the Von Mises method. It has been produced a graph to represent the distribution of the stress intensity in terms of the number of nodes using the production of a report.

It shall be noted that the deformation is represented using a scale factor to make the results clearer.
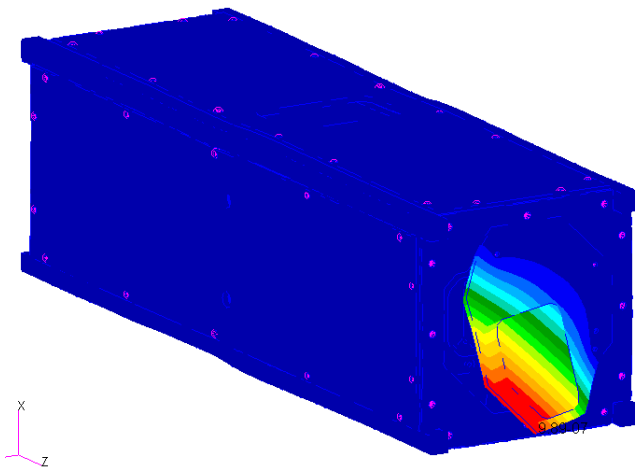
Figure 4.12 X_{pl} scenario displacement

Figure 4.13 X_{pl} scenario stress intensity distribution

Max. displacement	9.89e-07 m

105

Figure 4.14 Y_{pl} scenario displacement
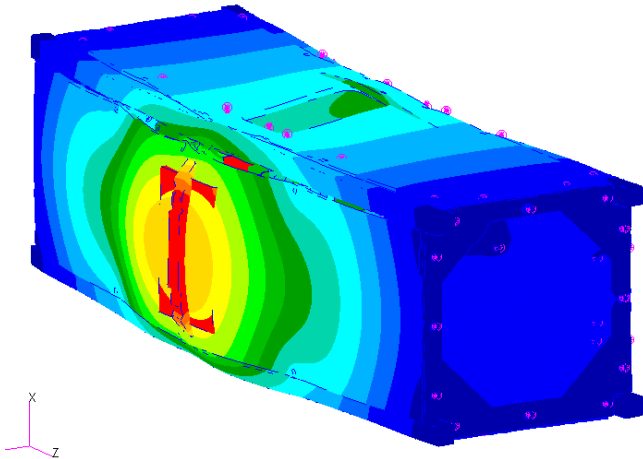
Figure 4.15 Y_{pl} scenario stress intensity distribution

Max. displacement	1.13e-06 m
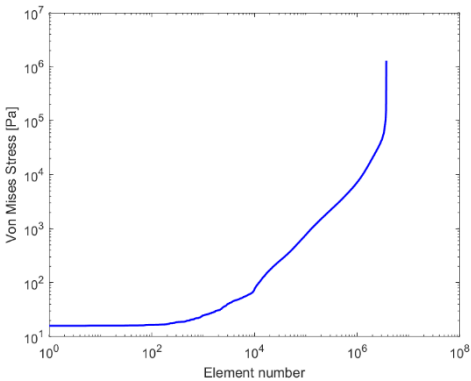
Figure 4.16 Z_{pl} scenario displacement
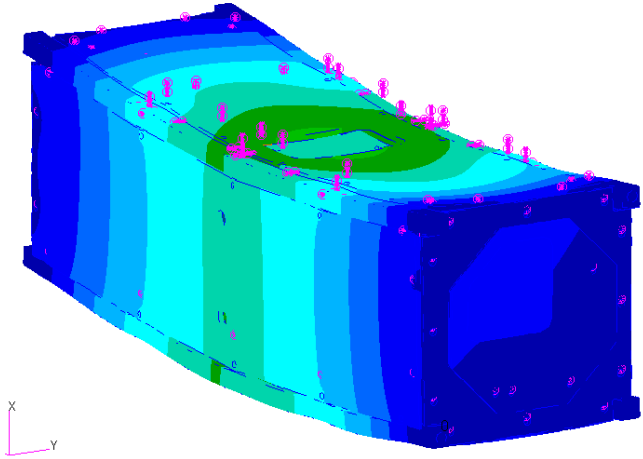
Figure 4.17 Z_{pl} scenario stress intensity distribution

Max. displacement	1.95e-06 m
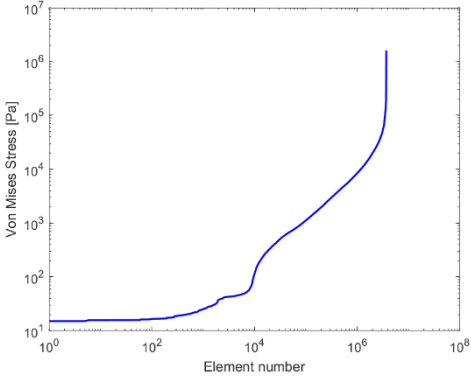
It's also possible to compare the different stress intensity distributions as to determine the most challenging scenario which resulted to be the Z_{pl} one from Figure 4.18.
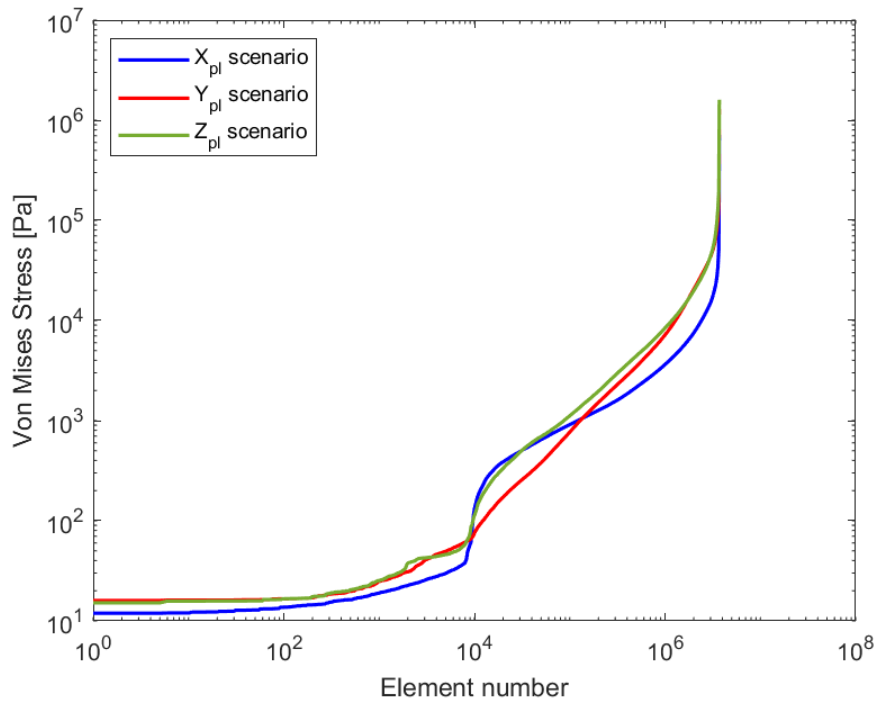
Figure 4.18 The three scenarios stress intensity distributions

As it can be seen both from the maximum displacement registered in the three scenarios and the stress intensity distributions, it's safe to assume that the spacecraft should be safe from damages caused by the quasi-static launch loads.

4.2.2   Modal analysis

The modal analysis is performed imposing a null load as it requires only the boundary conditions, already discussed in the previous paragraph.

In the modal analysis it's good practice to assess the correctness of the analysis performed through the evaluation of the Total Effective Mass Fraction. Such value indicates the amount of mass considered in the modal base, thus the combination of the calculated modes. This allow to assess the correctness of the analysis performed as a higher value indicates a bigger part of the system participating in the modes. As it's possible to understand from what has been said a higher number of desired modes leads to a bigger modal base, and an increase in the TEMF.
Through a series of iterations, it came to the conclusion that the solver requires a number of modes equal to 80 in order to obtain a TEMF higher than 90%.

Such task was performed through the addition of the command in the subcase section of the .bdf file.

107

> *$*
> *MEFFMASS(ALL) = YES*
> *$*

Moreover, through the same command it's possible to obtain the Modal Effective Weight which indicates the amount of mass participating in every mode. It's presented as divided in components and the most relevant in this case are the three translational ones as they allow to partially predict how the mode shape will appear.
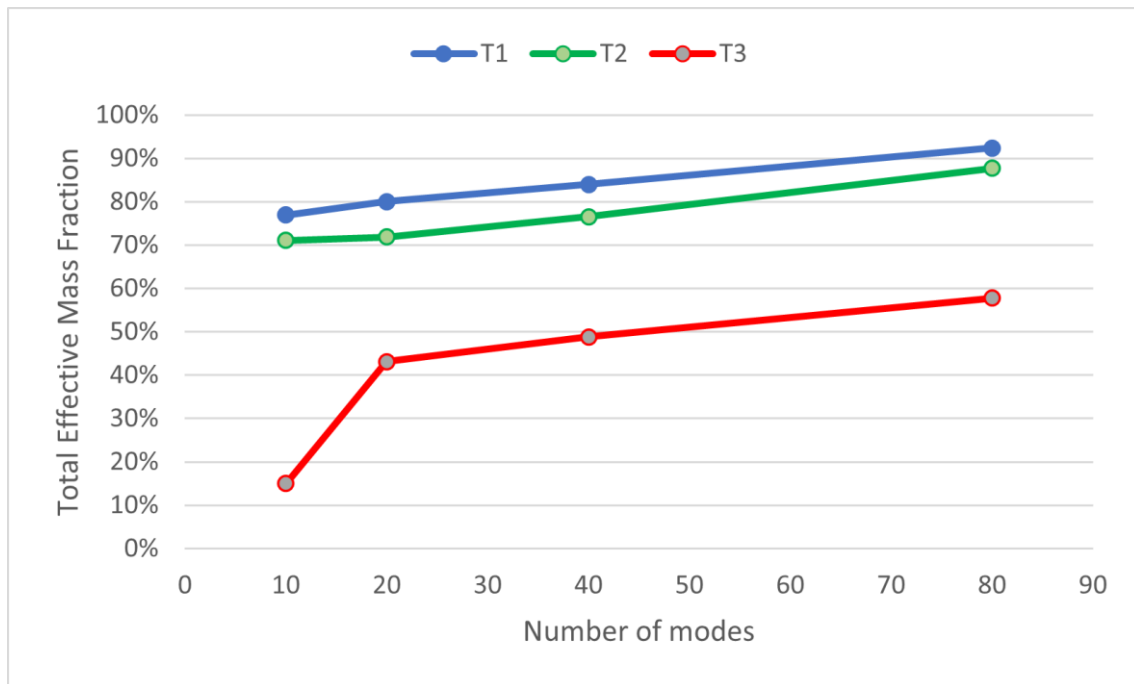
Figure 4.19 TEMF trend

As it can be seen from Figure 4.19 the TEMF shows a steady growth when it concerns the T1 and T2 components, while the T3 presents a sharp increase in its value with a minor increase in the modal base.

The following pictures represent the results from the modal analysis. In particular the modes shown are the first three, as to provide an overview of the modal shape. In Table 4.9, it will be possible to assess the frequencies of the first 10 modes as to obtain a general overview of the spacecraft behaviour.
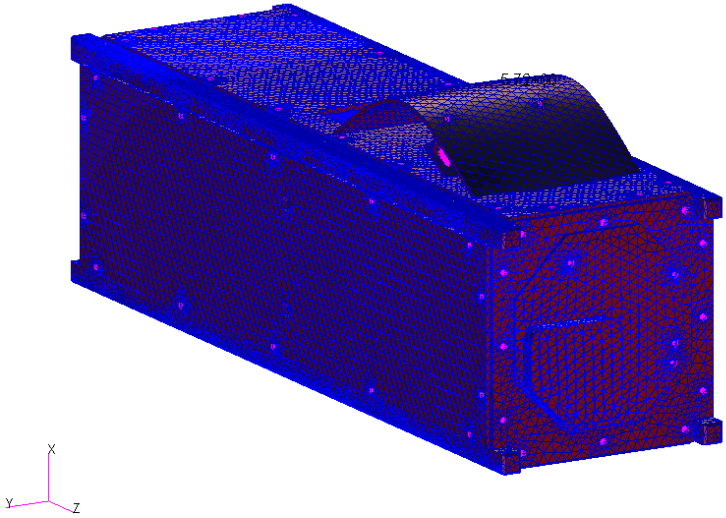
Figure 4.20 1st mode
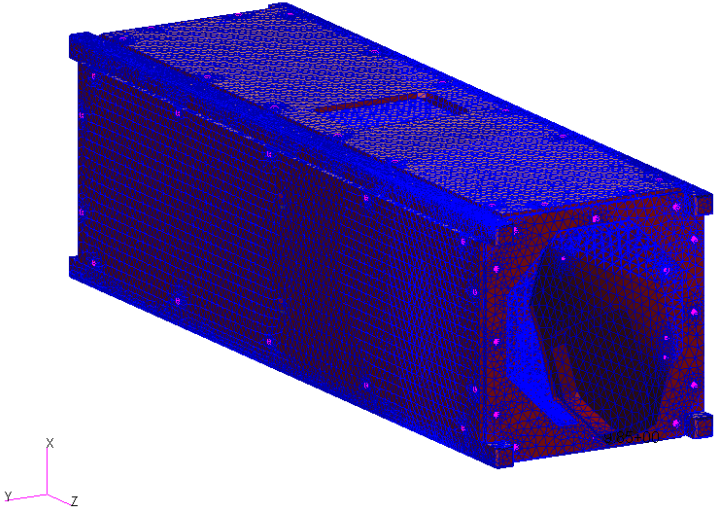
Figure 4.21 2nd mode
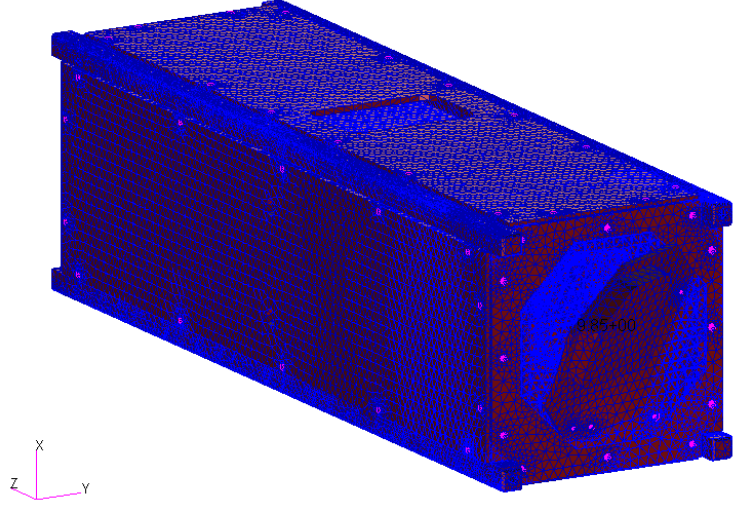
Figure 4.22 3rd mode

As it can be seen from Table 4.9 the first 10 modes have a natural frequency with a value much higher than 40 Hz, 503 Hz, requirement from the *Rideshare Payload User's Guide*. This is the most important validation of the model as it determines that it's compatible with the launcher itself. However it's still necessary to determine the entity of the spacecraft response generated by the launch loads, evaluation done in the following section.

Mode	Frequency
1	5.030613E+02
2	5.124989E+02
3	5.135229E+02
4	5.935405E+02
5	6.204787E+02
6	7.246175E+02
7	1.147564E+03
8	1.174540E+03
9	1.175953E+03
10	1.224169E+03

Table 4.9 Spacecraft's first 10 modes

4.2.3   Random vibration analysis

The random vibration analysis uses the modal one as an input to evaluate the spacecraft response to the dynamic loads generated by the launcher.

In this case the source of the loads is not the *Rideshare Payload User's Guide* but the document provided by D-Orbit which allowed to determine the environment to which the spacecraft was to be subjected considering the coupling between the launcher and the carrier.

The analysis was conducted identifying the two different scenarios, defined in the document as "longitudinal" and "lateral", respectively indicating a load applied along the Z and Y axes. Such information has been obtained following the same process described in 4.2.1.

Frequency [Hz]	ASD [g^2/Hz]
20	0.01800
45	0.06000
130	0.06000
230	0.01800
700	0.01800
800	0.03600
925	0.03600
2000	0.00773

Table 4.10 Y load case

Frequency [Hz]	ASD [g^2/Hz]
20	0.012
50	0.022
210	0.022
330	0.048
400	0.048
500	0.024
700	0.024
800	0.036
925	0.036
2000	0.008

Table 4.11 Z load case

The analyses were performed through the utilization of the random analysis tool "Patran random" provided by the software itself. In particular, the "enforced motion" method was applied as it allowed to define the input direction as well as the input nodes. Moreover, this method requires the selection of the additional displacement sets, in this case the single point constraints used to model the test-pod.

It's also necessary to define the modal damping, used to perform the analysis and to advert the possibility of causing an infinite response, as already seen in 2.2.2.2. In particular, it was decided to use a damping factor of 5%, chosen based on the state-of-the-art.

The input nodes have been decided according to the analysis performed as it was necessary to simulate the load applied. In the Y load case the nodes on the $+Y$ face of the rail have been chosen, while in the other analysis the face of the $-Z$ rails standoffs have been used.
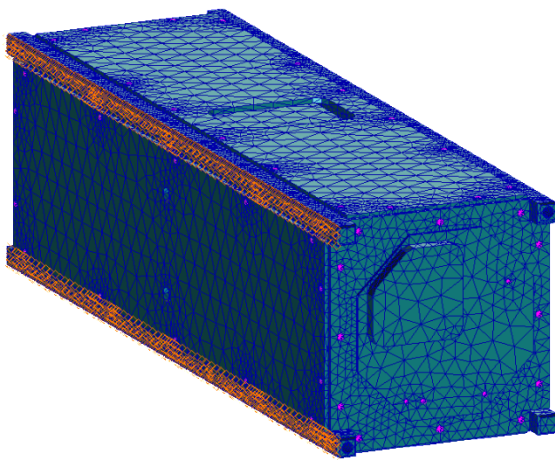
Figure 4.23 Y load case input nodes
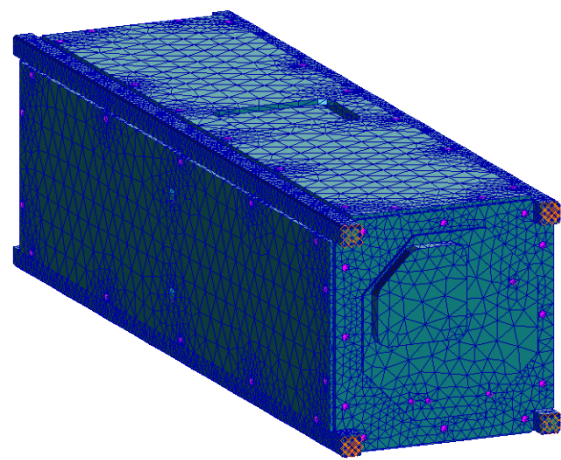
Figure 4.24 Z load case input nodes

Such decision has been taken taking into account the test configuration that will have to be performed, as described in 5.1.

Moreover, as an input the software generates a time dependent acceleration directed in the direction provided in the random analysis section, described by a non-spatial, frequency-based field.

With the definition of the analysis parameters the software performs a frequency response analysis with the modal formulation (SOL 111).

The resulting .xdb file needs to be used in the "Patran random" environment to perform an RMS analysis which allows to obtain the desired result, in this particular case the acceleration.

With the completion of the analyses it's possible to assess the results using XY graphs.

4.2.3.1 Y load case results

The following pictures depict the results registered from specific nodes on the $+X$ and $+Y$ solar panels, on the $-Z$ CommSys board support and the $+Z$ CommSys board itself. The reasons for such positioning will be discussed in 5.2.

In this case the component analysed is the 2nd DOF, representing the translation along Y.
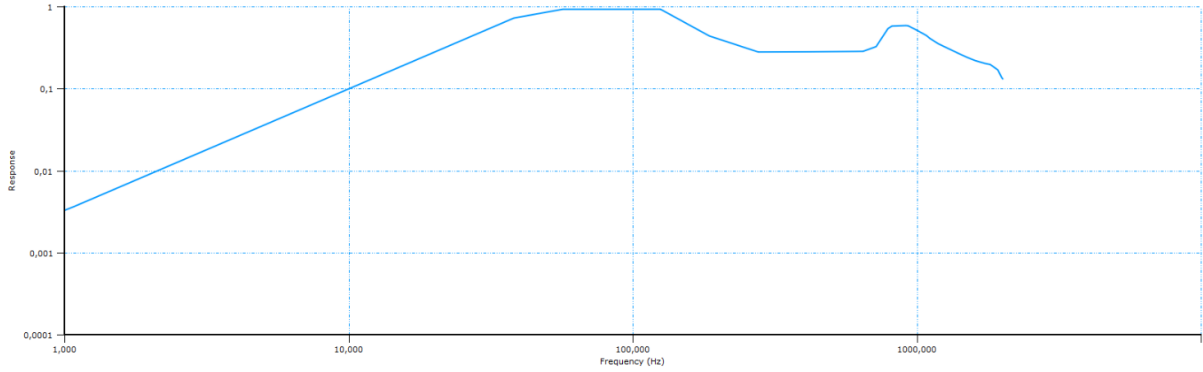
Figure 4.25 Y *load case +X solar panel response*
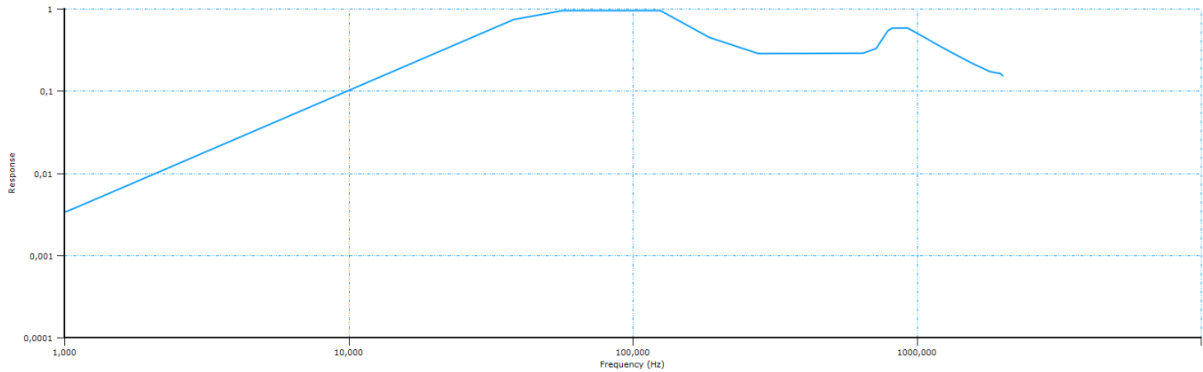
Figure 4.26 Y *load case -Y solar panel response*
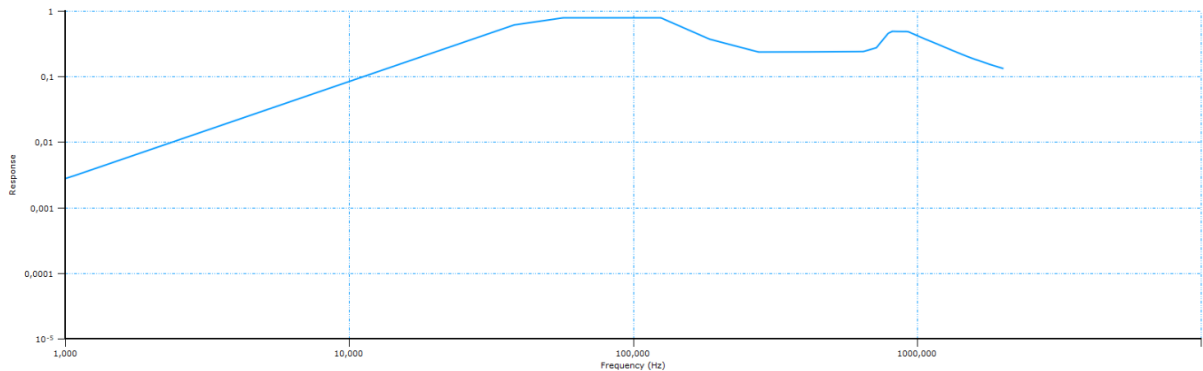
Figure 4.27 Y *load case -Z CommSys board support response*
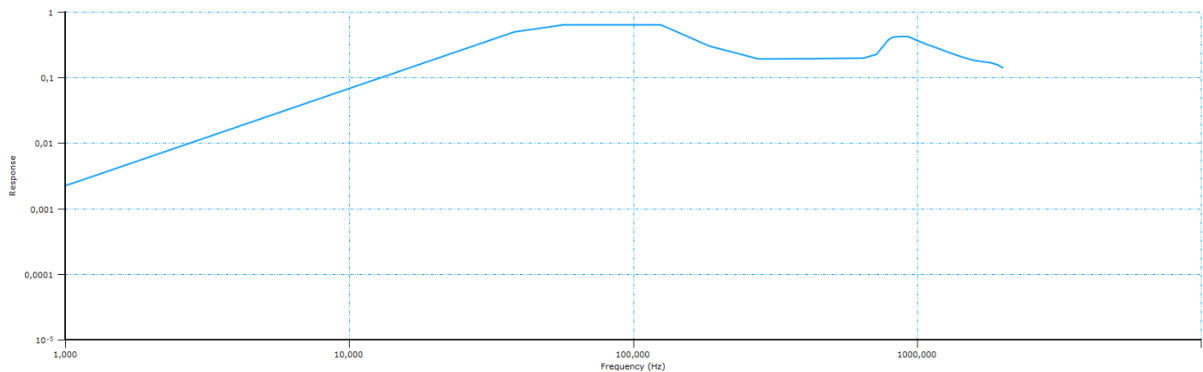
Figure 4.28 Y *load case +Z CommSys board response*

112

It's possible to calculate the RMS of the acceleration as a way to evaluate the system, or in this case the component, response in terms of acceleration.

Component	RMS
$+X$ solar panel	26.63
$-Y$ solar panel	26.60
$-Z$ CommSys board support	24.43
$+Z$ CommSys board	22.90

Table 4.12 Y *load case acceleration response RMS*

The evaluation of the graphs allows to have a general idea regarding the spacecraft response to lateral component of the launch environment vibrations. In these cases, the responses don't reach the value of 1, remaining nonetheless quite relevant. However, it's important to stress the fact that this model doesn't keep into account the presence of the screws themselves as they have been modelled using rigid connectors, thus making the response of the spacecraft more significant as it absorbs less energy.

4.2.3.2 Z load case results

In this case as well, the responses are evaluated as it's been done in the previous one with the main difference being the component analysed, in this case the 3rd DOF, representing the translation along Z.

Moreover, for the sake of consistency, the nodes analysed are the same as the one studied in the previous analysis case.
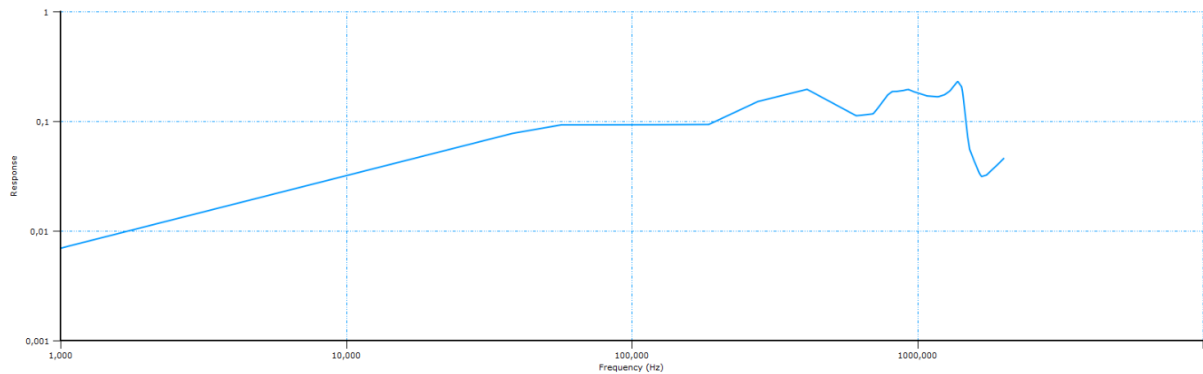
Figure 4.29 Z *load case* $+$X *solar panel response*
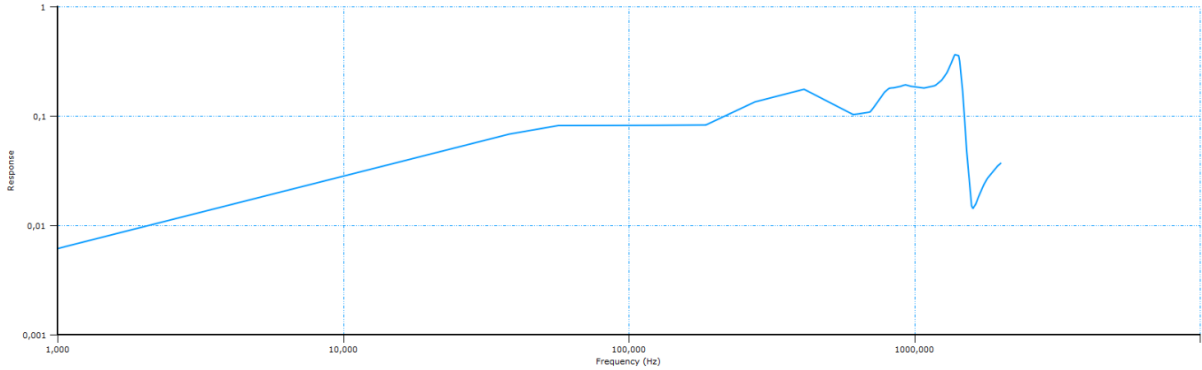
Figure 4.30 Z load case -Y solar panel response
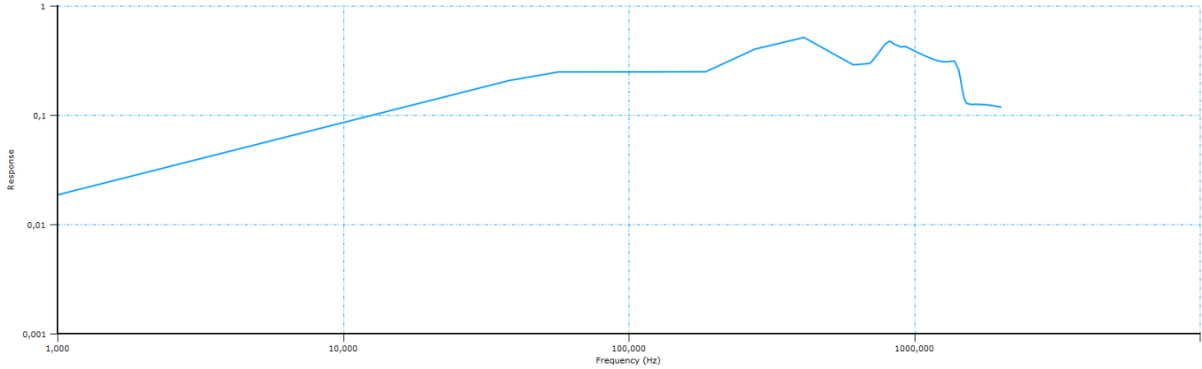
Figure 4.31 Z load case -Z CommSys board support
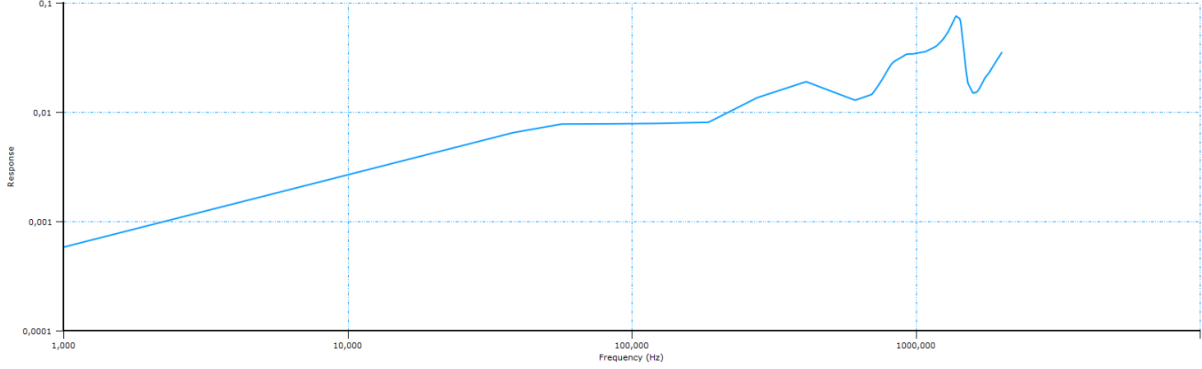
Figure 4.32 Z load case +Z CommSys board response

As in the previous case, the RMS of the acceleration response has been calculated.

Component	RMS
$+X$ solar panel	15.85
$-Y$ solar panel	16.17
$-Z$ CommSys board support	23.97
$+Z$ CommSys board	7.246

Table 4.13 Z load case acceleration response RMS

As it can be seen from the results above, in this case there is much bigger difference in terms of the acceleration response RMS between the various components. In particular the $+Z$ CommSys board has a very low response, result that was to be expected as it was the component least connected among those that have been studied. Moreover, this could be anticipated from the graph shown in Figure 4.32 as it presents a response much lower than the others.

All in all, the results obtained from this analysis have proven that the spacecraft should be able to resist to the launch vibration loads, even though the final confirmation will be provided by the environmental test, later discusses.

5   Environmental testing

With the successful completion of the FEA, the spacecraft was deemed to be eligible to be manufactured, assembled, integrated and tested. The last step, in particular, is the main subject of such chapter.

5.1   Testing platform

In order to create an environment as close as possible to that of the launch, it was necessary not only to provide the same loads, in this case vibration ones, but also to accurately represent the boundary conditions that it will have to face.

To reach such a goal, a test-pod was provided by D-Orbit representing the Astrofein deployer that will be mounted on the ION spacecraft. This was to be used during the testing phase as the vibration environment, provided as the requirement levels, are already generated by the system composed of the carrier and the launch vehicle, as already explained in 3.2.2. Therefore, the tested system is only made up by the test-pod and SPEISAT.
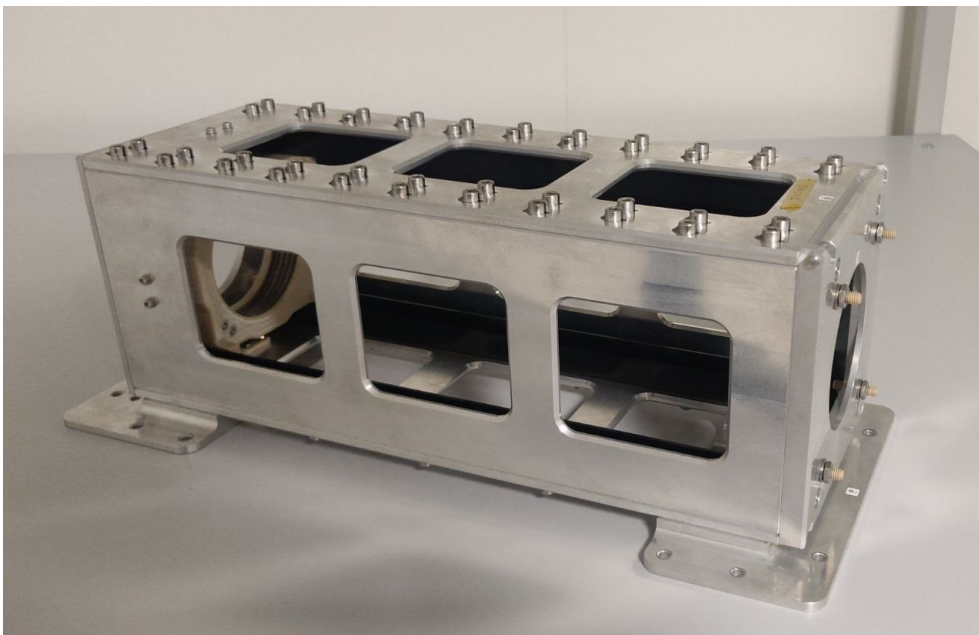
Figure 5.1 The test-pod

The test-pod is composed of a main frame in which the satellite is to be inserted, with the pusher plate mounted on a spring that needs to be released once the spacecraft has been safely positioned and the top plate closed.
The spring is fundamental to correctly represent the conditions that the spacecraft will have to face during the launch, as it will be mounted in the deployer ready to push it outside. Moreover, the presence of the spring causes a general drop of the system stiffness, causing the natural frequencies to get lower, as already seen in 2.2.2.2.

Moreover, to prevent even the slightest rattle, caused by the loss of contact between the spacecraft and the test-pod's rails due to the vibrations, the points of contact between the two

bodies have been covered with Kapton. This allowed also to avoid damages to the rails which would have caused an increase in the surface roughness, causing a non-compliance with the requirement SPEI-SYS-037.

Furthermore, it was necessary to provide an interface between the test-pod and the shaker that wouldn't affect the vibration loads to which the spacecraft was supposed to be tested with. Therefore, it was essential to guarantee a connection as stiff as possible.

This was done through a thick aluminium plate, that was supposed to be mounted on the shaker and the system test-pod – spacecraft would have been later integrated onto it. This would have guaranteed both the required stiffness and the simplicity during the test set-up phase.
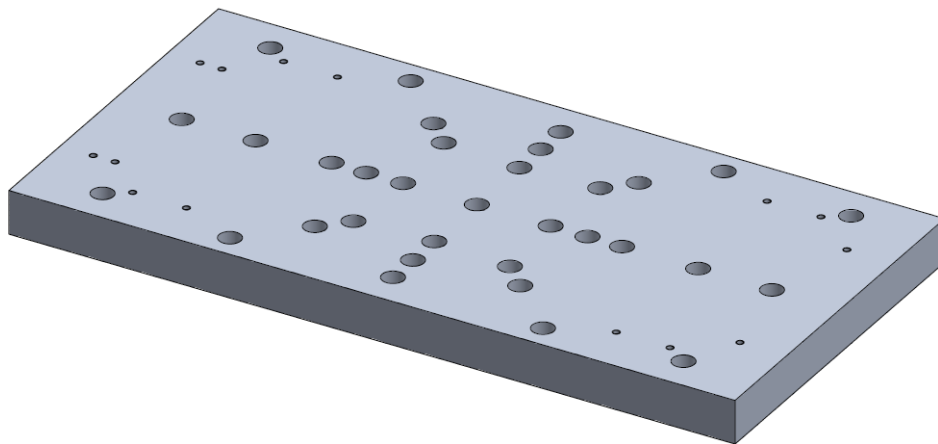
Figure 5.2 Interface plate

The resulting set-up is displayed in Figure 5.3.
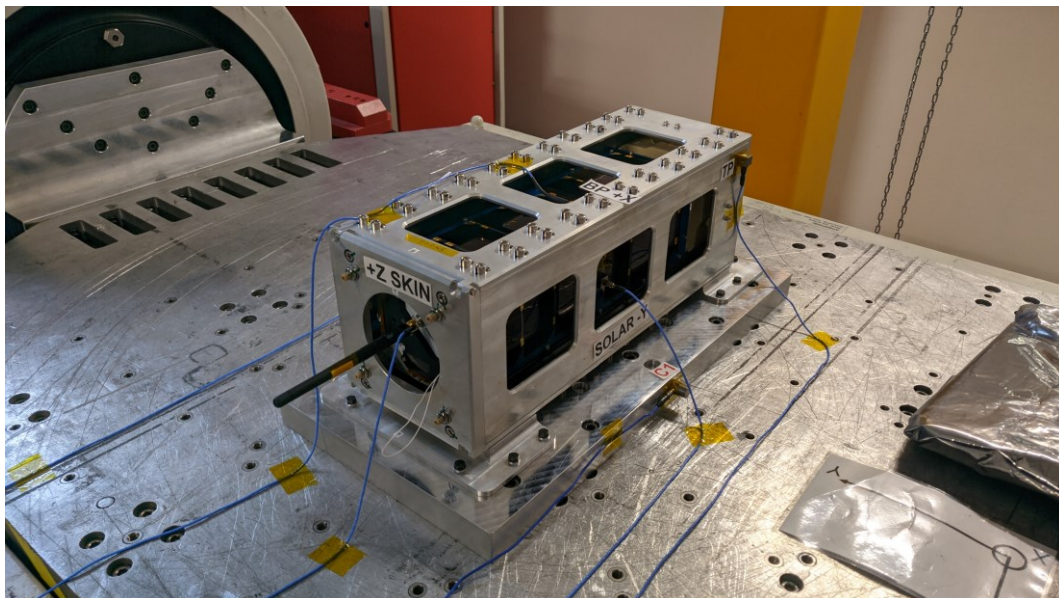
Figure 5.3 Test set-up

5.2   Accelerometers location

The sensors used in these tests were 3 axis accelerometers, capable of evaluating the response from the spacecraft or test-pod. Since the shaker had 16 channels available, including one occupied by the control accelerometer, it was possible to install up to 5 test accelerometers, as each monitored axis required a channel.

Therefore, it was necessary to determine where it was the most useful to install the sensors as to obtain the best data.

The control accelerometer was to be installed on a stiff point, as its role was to monitor the shaker output, making sure that it wouldn't diverge excessively from the environment provided as an input, remaining within the required limits. Because of this necessity, the best location was deemed to be on the interface plate, on the face whose normal was parallel with the vibration axis.
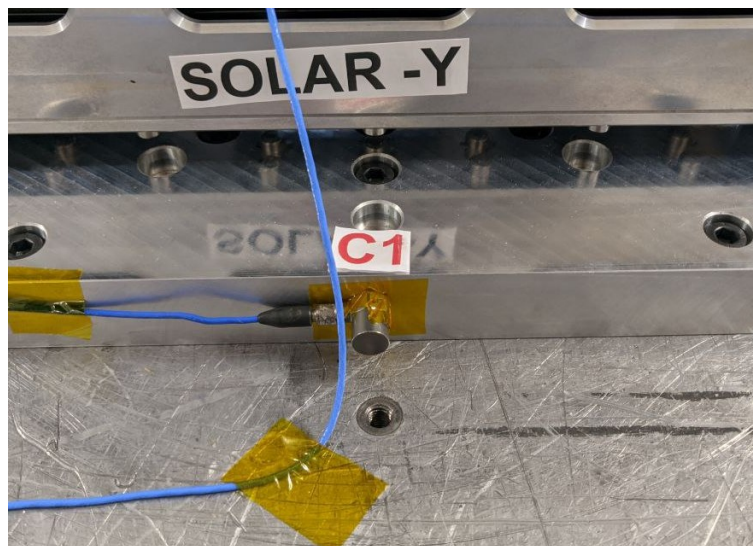
Figure 5.4 Control accelerometer

On the other hand, the test accelerometer had to be placed on relevant locations, capable of providing powerful insight into the system response. Obviously, the same spots used for the data collection after the random analyses were chosen for a matter of coherence and as to grant the possibility of assessing the differences between the two results data set. The motivations for such choices will be now presented:

1. $+Z$ **skin:** This one was placed on the CommSys board, located on the $+Z$ end. It was decided in order to evaluate the board response to the vibration loads.

Figure 5.5 +Z skin accelerometer

2. **−Z skin:** This accelerometer was located on the −Z face, directly on the aluminium support. In this way it could have been possible to determine the differences between the board and the support responses.
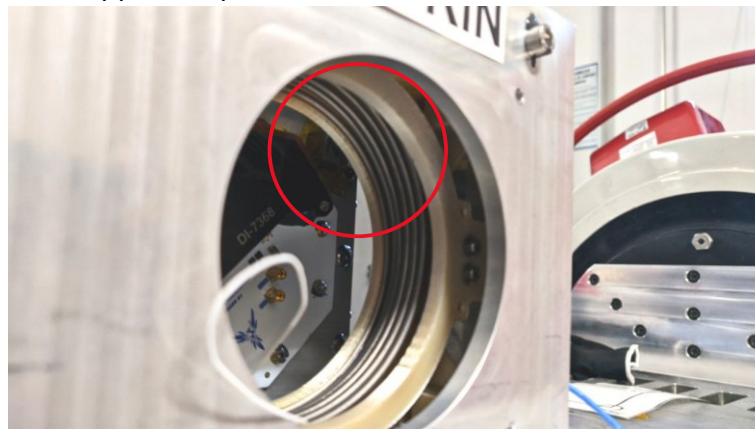
Figure 5.6 -Z skin accelerometer

3. **Solar −Y:** This sensor allowed the characterization of the response of the solar panel located on the −Y face of the spacecraft.
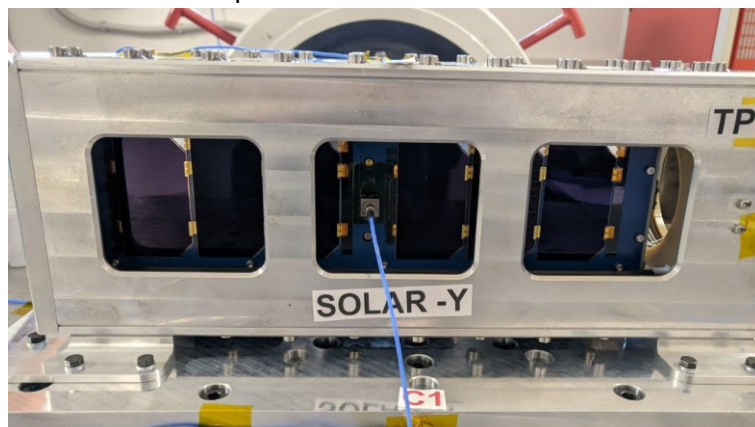
Figure 5.7 Solar -Y accelerometer

4. **BP +X:** Similarly to the previous accelerometer, this one was located on the solar panel placed on the +X face. In this way it would have been possible to evaluate the differences between the responses of two different solar panels, characterized by a different structure, due to the necessity of providing an access port on the +X one.
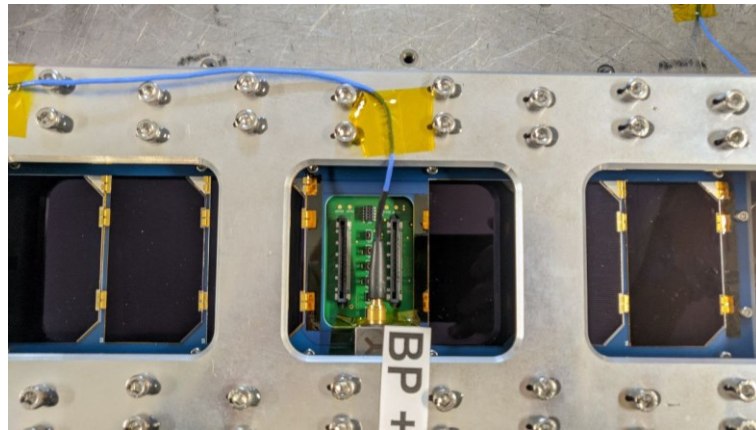
Figure 5.8 BP +X accelerometer

5. **TP:** The last accelerometer was placed on the test-pod as a mean to evaluate the response from the whole frame. This point in particular wasn't evaluated during the random analyses as the test-pod wasn't modelled.
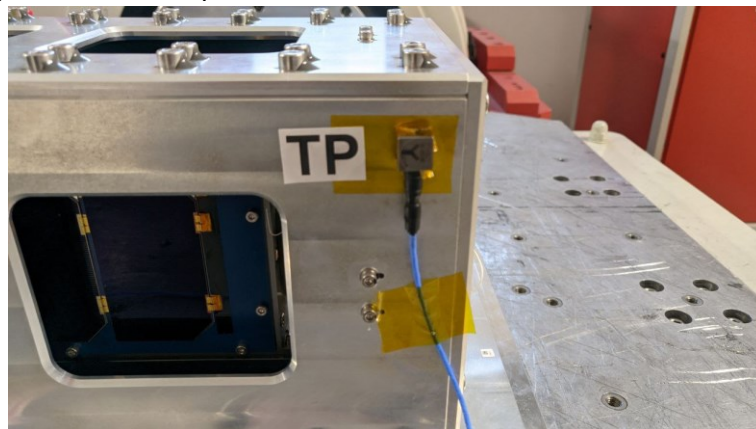
Figure 5.9 TP accelerometer

5.3   Vibration loads

The testing loads were provided by D-Orbit as a document to complete with the ASD registered during the test for certain frequencies, thus obtaining a test level profile that was supposed to be higher than the one of the system composed of ION and the launch vehicle.

Frequency [Hz]	ASD [g²/Hz]
20	0.01800
45	0.06000
130	0.06000
230	0.01800
700	0.01800
800	0.03600
925	0.03600
2000	0.00773
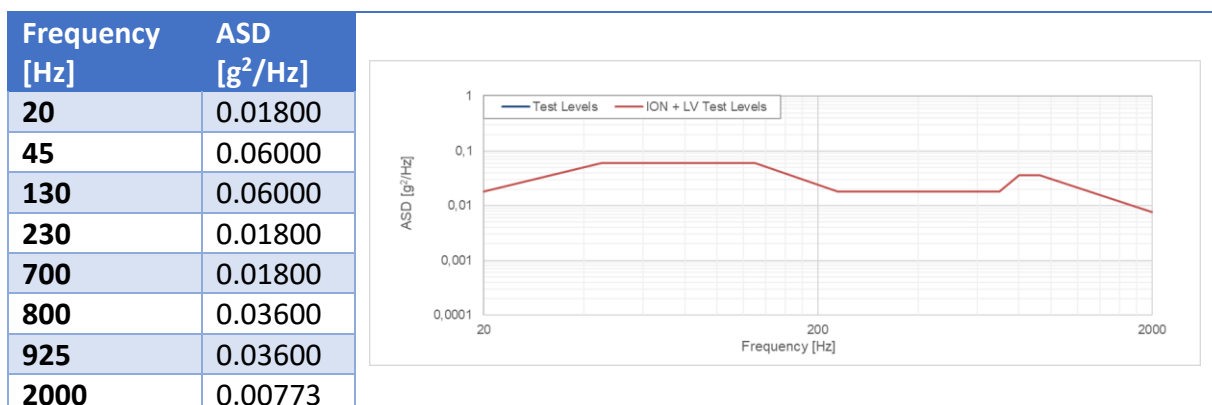
Table 5.1 Lateral vibrations testing levels

Frequency [Hz]	ASD [g²/Hz]	
20	0.012	
50	0.022	
210	0.022	
330	0.048	
400	0.048	
500	0.024	
700	0.024	
800	0.036	
925	0.036	
2000	0.008	
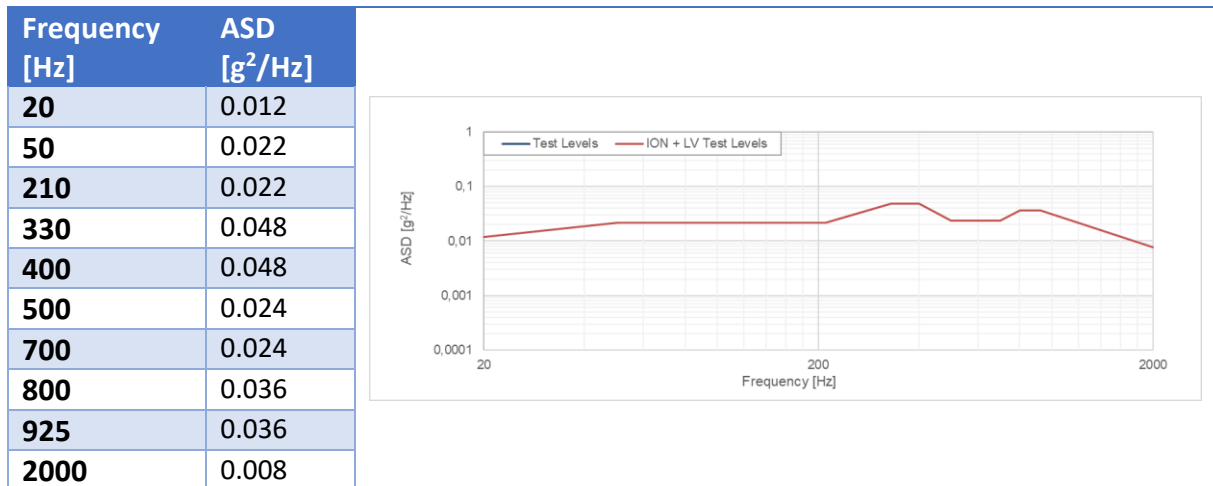
Table 5.2 Longitudinal vibrations testing levels

At this point the most delicate thing to assess is the correct position of the spacecraft inside the test-pod and the orientation of the whole system on the shaker. An incorrect orientation would compromise the testing as there wouldn't be an accurate representation of the launch environment.

Figure 5.10 depicts the fairing of the Transporter 8 mission, in red is highlighted the Astrofein deployer containing SPEISAT. This represents the configuration that it's necessary to replicate in the testing phase as to gauge the spacecraft response to the vibration loads.

Figure 5.10 Transporter 8's fairing

The orientation of the spacecraft has been obtained using the information already used during the analyses phase, as it was necessary to determine how the loads were to be applied.

In this was it was possible determine the testing orientation for the spacecraft. Being the shaker mono-axis it was required to turn all the testing platform in order to perform both tests. The following pictures depict the two set-up.
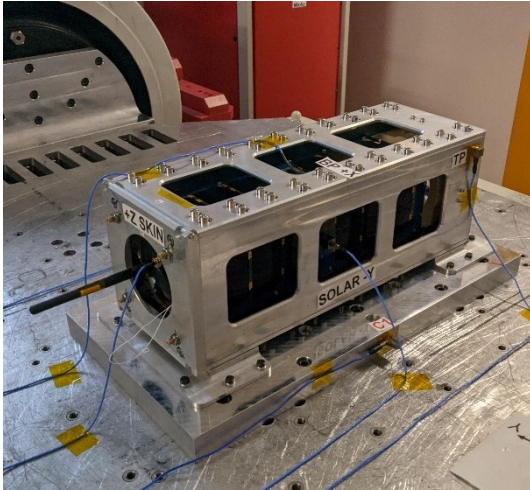
Figure 5.11 Lateral test configuration
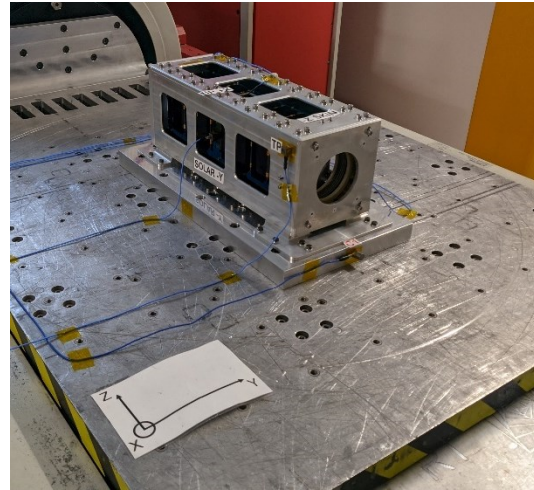
Figure 5.12 Longitudinal test configuration

At this point it's necessary to introduce the tests performed in their entirety.

From the requirements provided by D-Orbit it was necessary to simply test the spacecraft at the given levels to verify its compliance.

However, to guarantee the safety of the CubeSat, as well as to verify the occurrence of any changes in the internal configuration, several extra testing phases were devised before reaching the final one.

In particular, before the first and after the last test with each configuration, a sine sweep test was conducted. This allowed to perform a general assessment of the internal status of the spacecraft without having to open it.

Moreover, with the effective test having a duration of 60 seconds, 3 more were planned characterized by the same vibration profile but shifted of a certain amount, making the vibration loads less intense. This would have allowed to interrupt the test in case of anomalies.

Therefore, the final testing procedure can be described as below.

1. Sine sweep with a constant acceleration of 0.5 g with a range of frequencies between 10 Hz and 2000 Hz and with the duration of 30 seconds.
2. Random vibration with ASD as defined in Table 5.3 under the column "ASD [g^2/Hz] – 12 dB" with the duration of 30 seconds.
3. Random vibration with ASD as defined in Table 5.3 under the column "ASD [g^2/Hz] – 6 dB" with the duration of 30 seconds.
4. Random vibration with ASD as defined in Table 5.3 under the column "ASD [g^2/Hz] – 3 dB" with the duration of 10 seconds.
5. Random vibration with ASD as defined in Table 5.3 under the column "ASD [g^2/Hz]" with the duration of 60 seconds.
6. Sine sweep with a constant acceleration of 0.5 g with a range of frequencies between 10 Hz and 2000 Hz and with the duration of 30 seconds.

Random lateral vibrations				
PFM Levels				
Frequency [Hz]	ASD [g^2/Hz]	ASD [g^2/Hz] - 12dB	ASD [g^2/Hz] - 6dB	ASD [g^2/Hz] - 3dB
20	0.01800	0.001136	0.004521	0.00902
45	0.06000	0.003786	0.015071	0.03007
130	0.06000	0.003786	0.015071	0.03007
230	0.01800	0.001136	0.004521	0.00902
700	0.01800	0.001136	0.004521	0.00902
800	0.03600	0.002271	0.009043	0.01804
925	0.03600	0.002271	0.009043	0.01804
2000	0.00773	0.000488	0.001942	0.00387

Table 5.3 Random lateral testing vibrations values
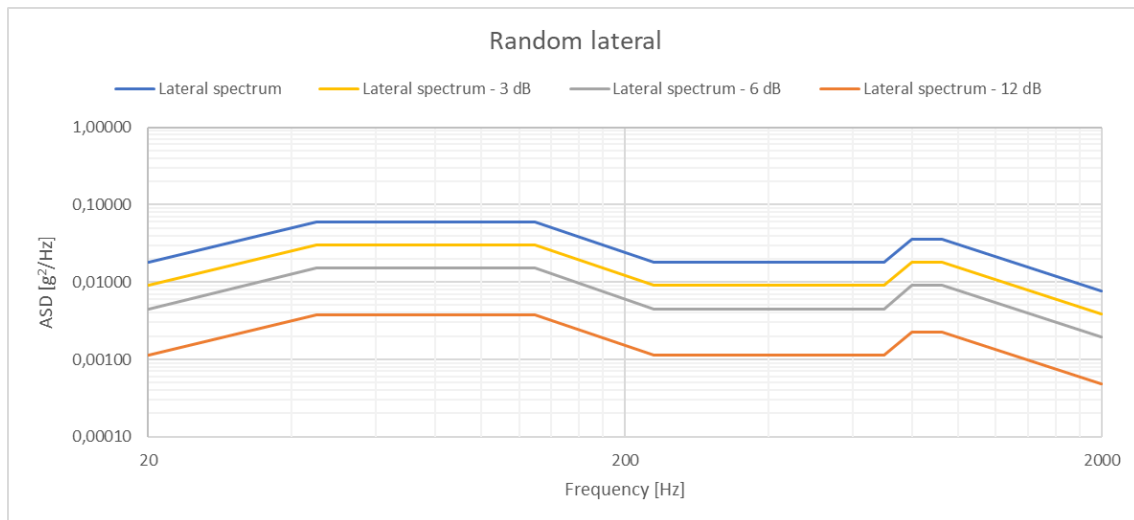
Figure 5.13 Random lateral tests level profiles

After the disassembly of the testing platform from the shaker, and its remounting in the new configuration, the test was to be repeated with the same steps, using the values provided in Table 5.4.

It needs to be noted that between the first and second set of tests, as well as at the end of the second, a functional test was performed to assess the correct functioning of the spacecraft. While the sine sweep was capable of only providing a general insight regarding the mechanical status of the system, this would allow to verify that there weren't any failures of smaller scale (on a mechanical aspect) such as the detachment of cables which could cause the impossibility of turning on the spacecraft or transmitting data packets.

Random longitudinal vibrations				
PFM Levels				
Frequency [Hz]	ASD [g²/Hz]	ASD [g²/Hz] - 12dB	ASD [g²/Hz] - 6dB	ASD [g²/Hz] - 3dB
20	0.012	0.000757	0.003014	0.006014
50	0.022	0.001363	0.005426	0.010826
210	0.022	0.001363	0.005426	0.010826
330	0.048	0.003029	0.012057	0.024057
400	0.048	0.003029	0.012057	0.024057
500	0.024	0.001514	0.006029	0.012028
700	0.024	0.001514	0.006029	0.012028
800	0.036	0.002271	0.009043	0.018043
925	0.036	0.002271	0.009043	0.018043
2000	0.008	0.000488	0.001941	0.003873

Table 5.4 Random longitudinal testing vibrations values
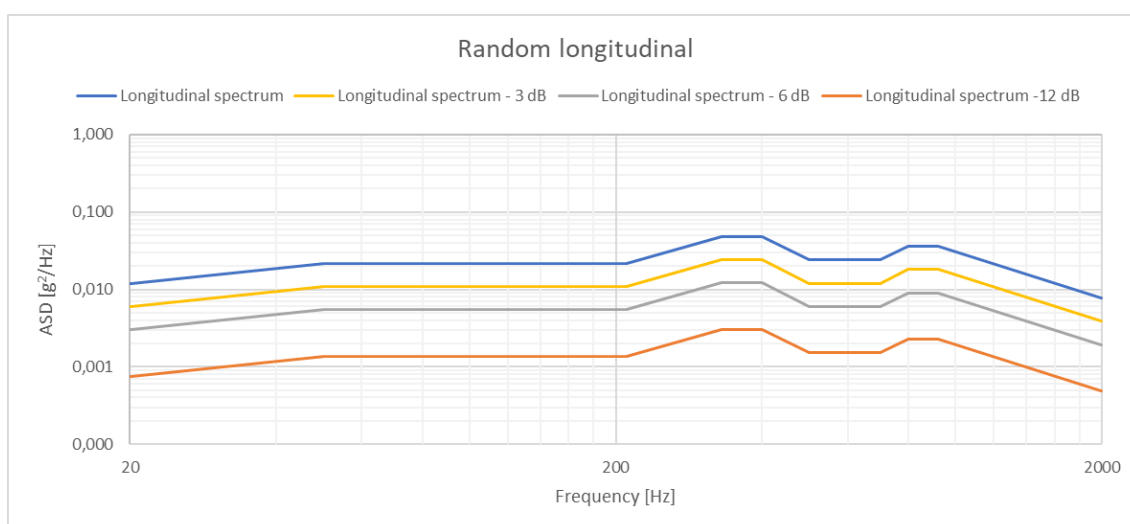
Figure 5.14 Random longitudinal tests level profiles

The choice of conducting the lateral test first, was dictated by the higher ASD of the longitudinal one. Therefore, in order to gradually arrive at the most stressful test, it was decided to conduct them in this order, as if the spacecraft hadn't been able to survive to the lateral vibration loads, then it most likely wouldn't have been able to resist to the higher ones.

5.4   Tests results

The graphs that will be presented in this section represent the data collected from the accelerometers during the vibrational tests conducted in each configuration.
For simplicity's sake, only the sine sweep and the test at full spectrum will be discussed, taking into account only the axis of interest measured by the accelerometers.

5.4.1   Lateral vibrations

The first tests analysed are those conducted in the lateral configuration. Therefore, the most relevant component is the Y one.

5.4.1.1   Random vibrations

The full spectrum test excited the spacecraft for a total of 60 seconds, with a frequency spectrum between 20 and 2000 Hz.
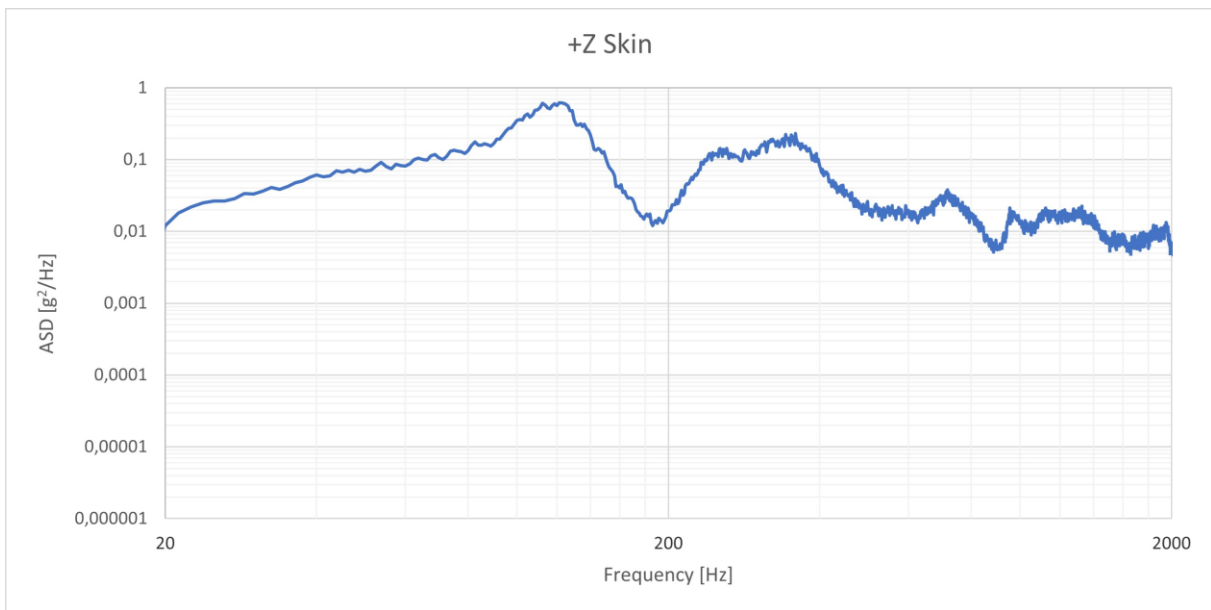
Figure 5.15 +Z skin lateral random vibrations results
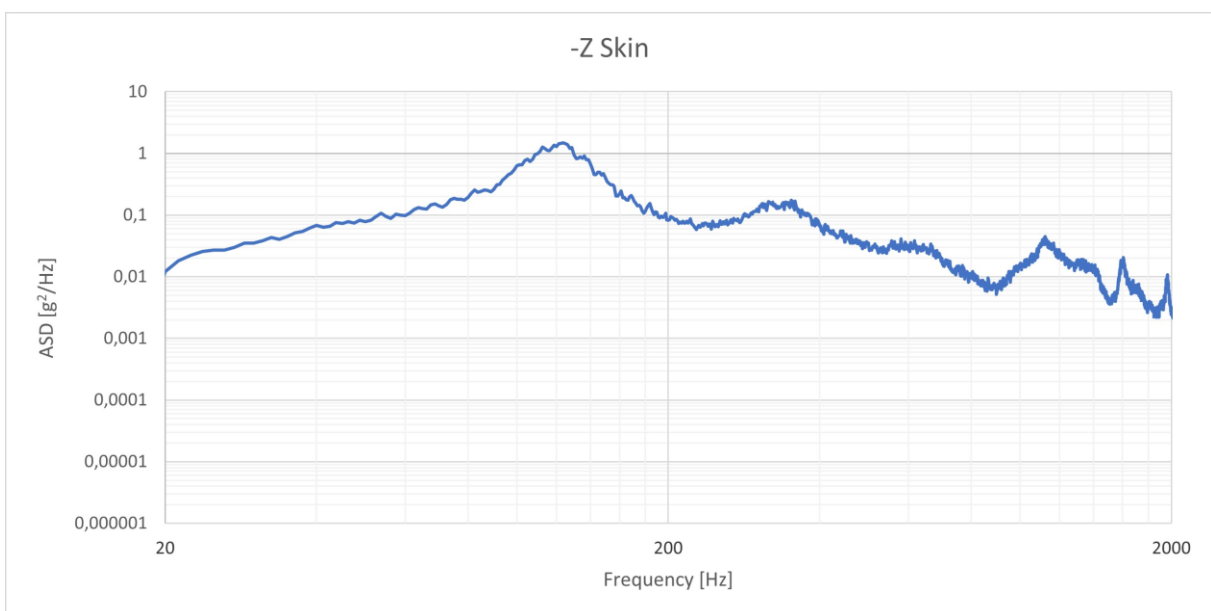
Figure 5.16 -Z skin lateral random vibrations results
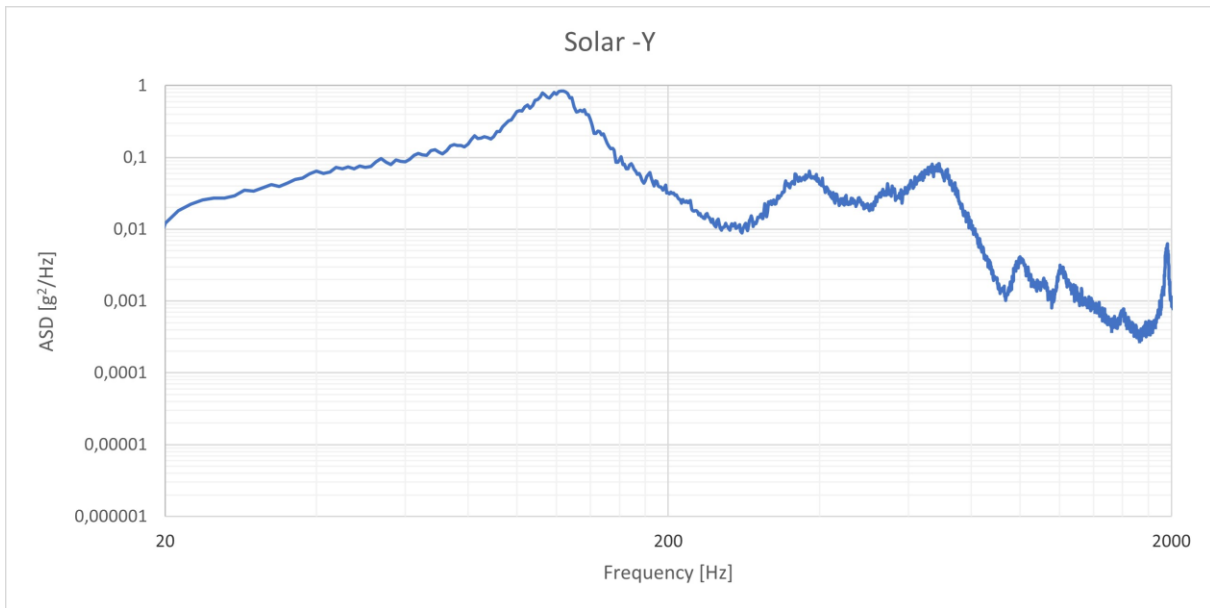
Figure 5.17 Solar -Y random lateral vibrations results
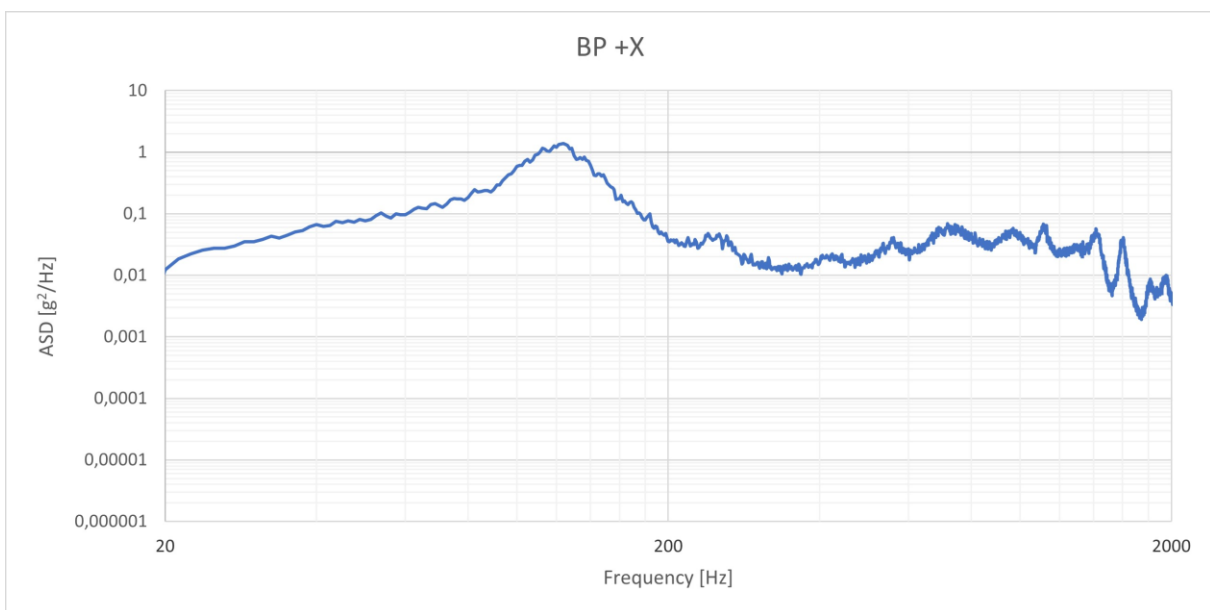
Figure 5.18 BP +X random lateral vibrations results

As it can be observed in the four images above, there is a tendency of having a first maximum in the ASD, corresponding to a frequency of 130 Hz, caused by the resonance phenomenon which occurs when a system is excited at its natural frequency. Such value is much lower than the one encountered during the FEA, however, during the analyses, the presence of the cables have not been kept into account. These were tried to be kept as stiff as possible, however, as this wasn't completely feasible, a small freedom of movement remained, causing them to vibrate while being connected to the various components which supported their masses. The same case can be applied to other elements attached to the various components.

Moreover, due to the modelling of the screws as rigid connectors, there has been a general

increase in the system stiffness. As it was seen in 2.2.2.2, this leads to higher natural frequencies, modifying the system response.

After the maximum, there is a decrease in the ASD, due to both a decrease in the ASD applied (note that it lowers from 0.06 at 130 Hz to 0.018 at 230 Hz, as seen in Table 5.3) and the distancing from the natural frequency of the spacecraft. However, it's possible to observe that there's a second tendency to higher values in the ASD at higher frequencies. In these cases this is mainly caused by the higher value of the loads applied, which excited the spacecraft causing a stronger response.

The remaining result that has yet to be seen is the one regarding the accelerometer located on the test-pod, which is presented below.
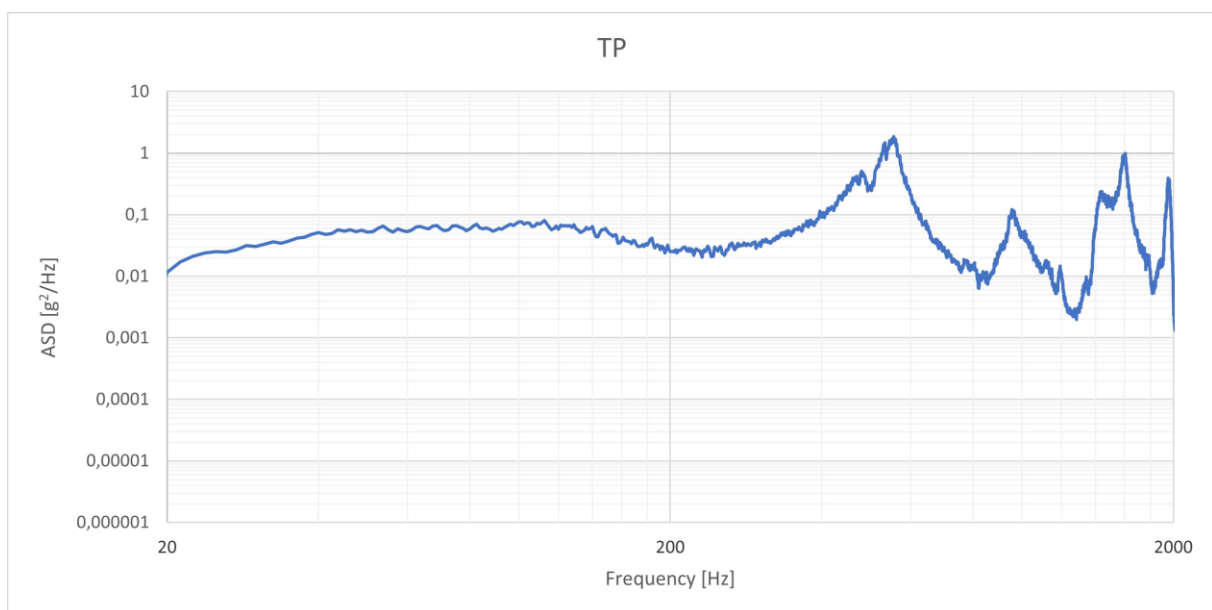
Figure 5.19 TP lateral random vibrations results

The test-pod, unlike the spacecraft, doesn't present the same pattern regarding its response. In fact, as it can be seen from Figure 5.19, the first peak is reach only at 600 Hz, followed by a rapid successions of maxima and minima in the ASD values.

Such difference can be simply imputed to the fact the test-pod isn't part of the spacecraft system and behaves as a stiffer body. As it was seen in 2.2.2.2, an increase in stiffness leads to an increase in the natural frequencies value. In the test-pod case these weren't determined, however, it's safe to assume that the first mode presents itself at a frequency of 600 Hz, corresponding to the first peak.

The maximum observed in the spacecraft case, in the test-pod ones is translated simply in a mild increase due to the raise of the vibration loads corresponding to those frequencies.

5.4.1.2 Sine sweep tests

This section serves to compare the sine sweep tests conducted before and after the random vibrations. The comparison between the two allowed to rapidly assess the status of the spacecraft.

Figure 5.20 +Z skin lateral sine sweep comparison

Figure 5.21 -Z skin lateral sine sweep comparison

The first considerations can be carried out through the evaluation of the differences between the $+Z$ and $-Z$ skin accelerometers' data. The former, whose results are shown in Figure 5.20 and Figure 5.21, presents more pronounced differences between the two tests, despite being qualitatively similar. This can be justified by noticing the differences between the placement of the two accelerometers. In 5.2 it was explained that the $+Z$ one was located on the

CommSys board, while the $-Z$ one on the aluminium support itself. While this may appear as a minor detail, it's actually extremely relevant as the support presents a much higher stiffness than the board, generally realized in FR4. Moreover, the board has the antennae case attached, which adds further variability to the subsystem, which can be affected to minor changes, still nothing to be wary of, causing slight fluctuations in the sine sweep test. On the other hand, the $-Z$ skin dataset is more conservative and less subject to change thanks to the stiffness of the component and of those which it's fastened to.
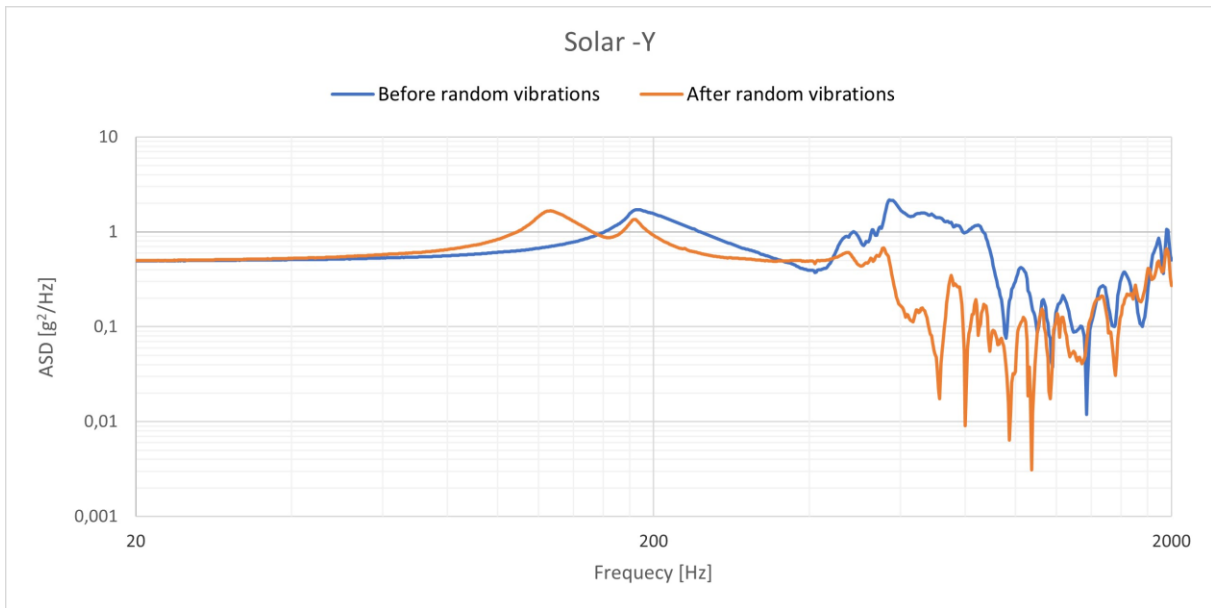
Figure 5.22 Solar -Y lateral sine sweep comparison
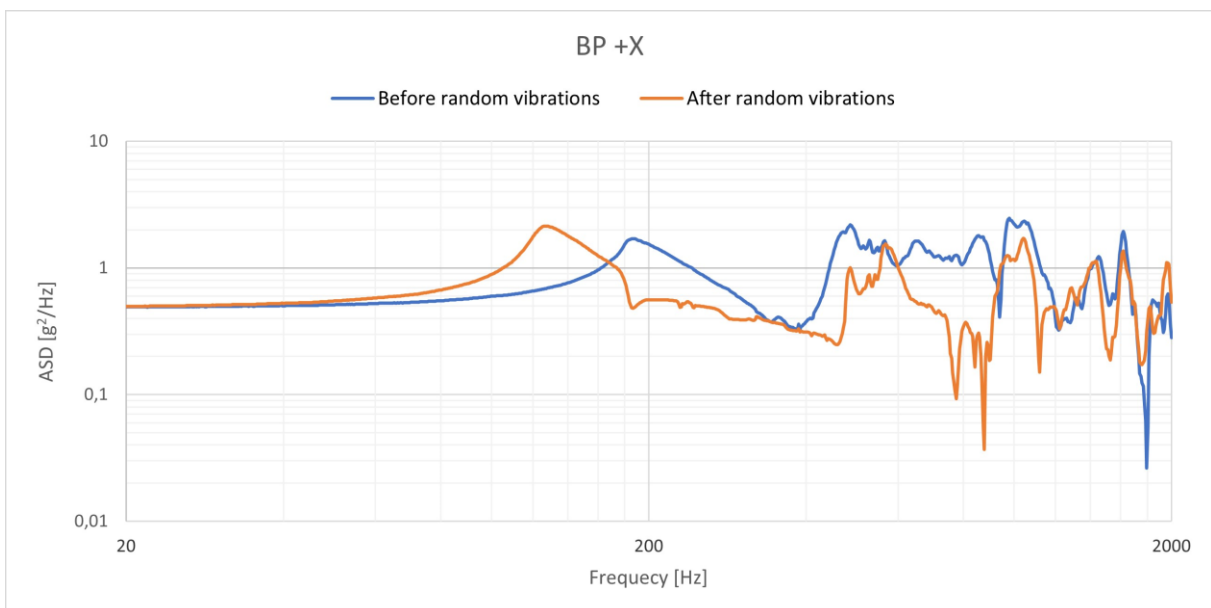
Figure 5.23 BP +X lateral sine sweep comparison

The data collected by the Solar $-Y$ and BP $+X$ accelerometers, highlight how the system hasn't

been subjected to changes. On a qualitative view, the pattern of the response remains the same, without anything to be noted.

Moreover, in all previous measurements, there has been a shift from the first peak to a lower frequency. At first glance, this may seem to indicate a loosening of the screws holding the various components of the spacecraft, thus causing a fall of the first natural frequency due to the reduction of the whole system's stiffness. However, this wasn't the case, as the various screws' position was marked once they were tightened and secured with the Epoxy Adhesive 2216, as shown in Figure 5.25. Therefore it was possible to verify that they hadn't been subjected to any undoing.

The most exhaustive explanation that was possible to provide was that the spacecraft has been subjected to a small rattling phenomenon, causing a slight change in the results collected during the test.

Obviously, the interior of the satellite was deeply examined once brought back to STARlab, without detecting any anomaly.
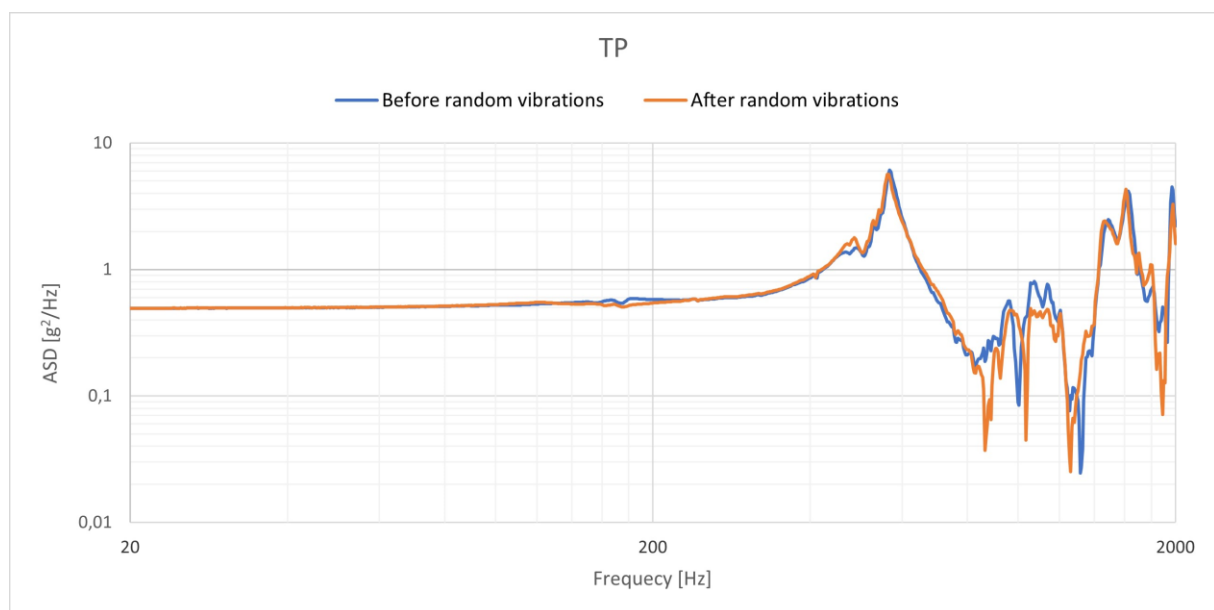
Figure 5.24 TP lateral sine sweep comparison

The discussion brought up for the $-Z$ Skin can be resumed regarding the data collected by the last accelerometer, located on the test-pod. As it can be seen the two curves are almost completely coinciding, with only a few, small fluctuations. This can be attributed to the extremely higher stiffness of the test-pod, already address in the previous section 5.4.1.1. Thanks to it, the system has been subjected to almost no alterations and the response provided by the mock-up deployer didn't suffer any changes.

131
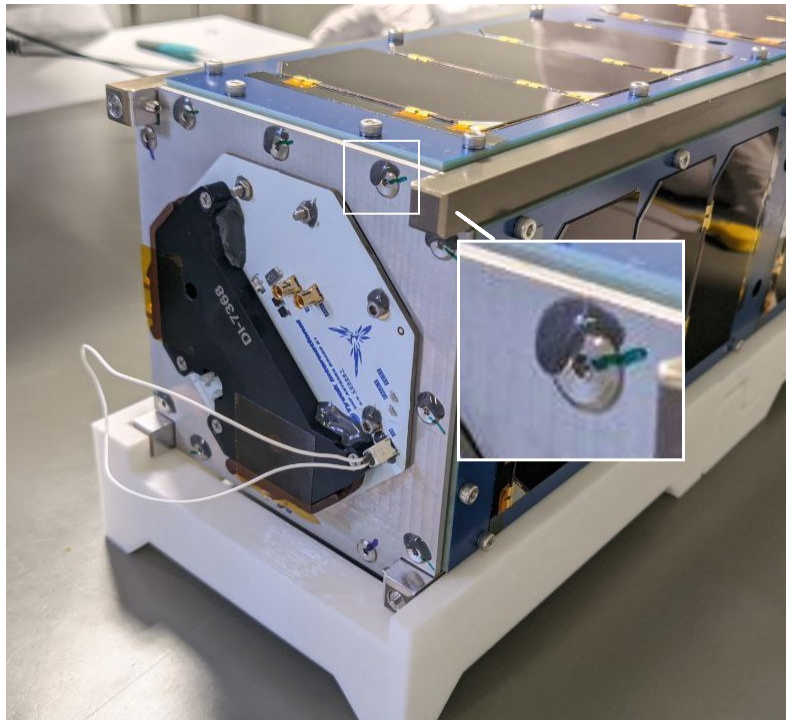
Figure 5.25 Tightened screws' marks

5.4.1.3 FEA and vibration test comparison

The response can be confronted with the one registered during the FEA as to assess the correctness of the analyses. This can be done by calculating the RMS of the acceleration response and confronting it with the one obtained through the analyses.

The following table compares the two RMS registered for each component studied, both through the FEA and the vibration test. In particular, the latter have been calculated through a simple *MatLab* code as the square root of the area underlying the curve described by the component response.

Component	FEA RMS	Test RMS
$+X$ solar panel	26.63	10.31
$-Y$ solar panel	26.60	7.877
$-Z$ CommSys board support	24.43	10.63
$+Z$ CommSys board	22.90	8.824

Table 5.5 Lateral case acceleration response RMS comparison

As it can be seen from Table 5.5, the FEA resulted in a much more striking response that could be deduced by several factors. First of all, as already explained before, the modelling of the screws through the rigid connectors, as the screws provide a damping of the energy transmission leading to a softer response.

Moreover, the presence of several components not modelled in the Finite Element Model leads to a further decrease in the intensity of the acceleration response.

Further impact on the results is the different natural frequencies, which appear to be lower than those expected. Such event has already been described and analysed however for the

sake of completeness it was taken up again as one potential cause of the difference between the results.

Furthermore, the rattling phenomenon cannot be ignored whatsoever as it could have potentially led to a further divergence of the results from what was to be expected.

However, the comparison between the responses registered during the testing and those obtained during the FEA highlights a qualitative coherence, especially considering all the events that led to a variation of the results.

5.4.2 Longitudinal vibrations

The completion of the considerations regarding the lateral tests, allows the introduction of the longitudinal ones, presented in like manner.

5.4.2.1 Random vibrations
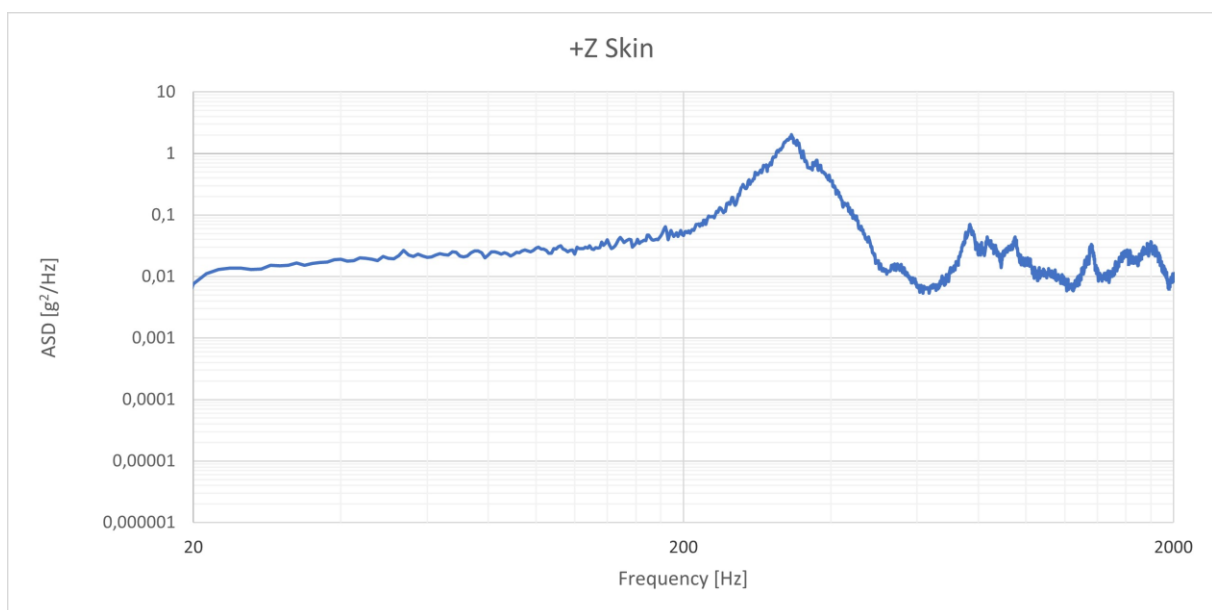
Figure 5.26 +Z skin random longitudinal vibrations results
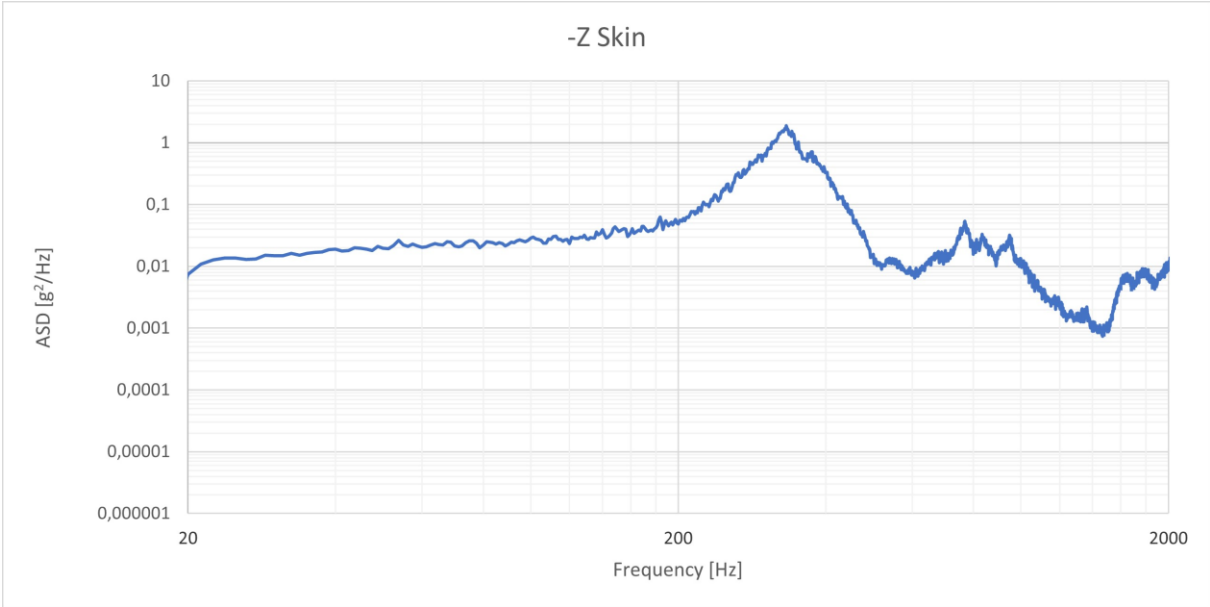
Figure 5.27 -Z skin random longitudinal vibrations results
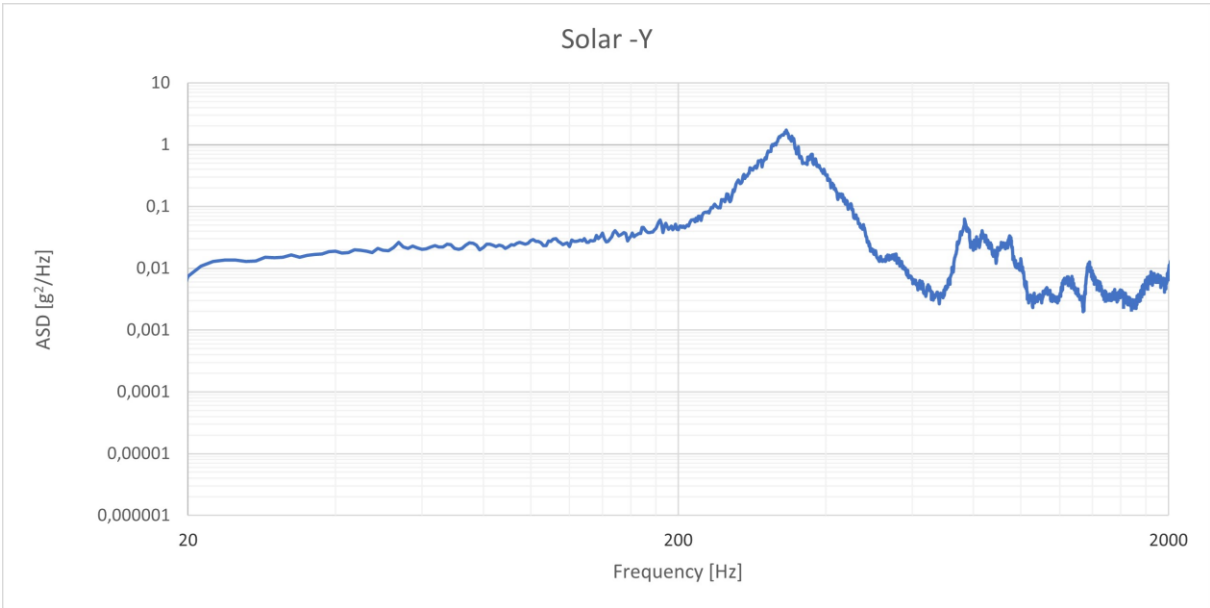
Figure 5.28 Solar -Y random longitudinal vibrations results
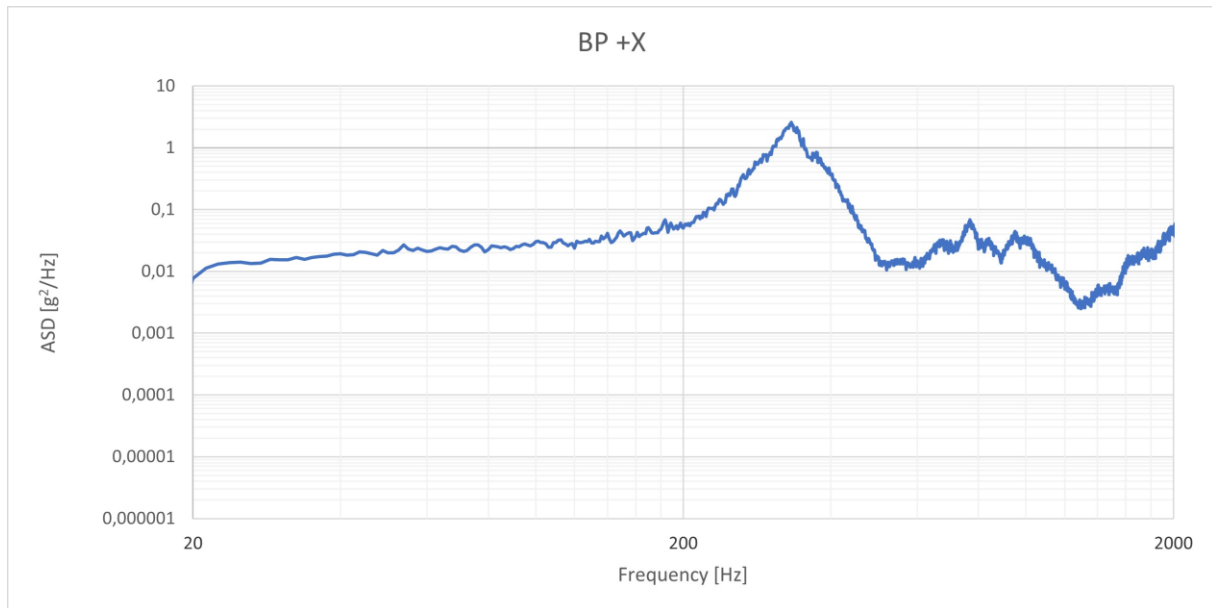
Figure 5.29 BP +X random longitudinal vibrations results

Similarly to the lateral vibration loads case, in this one as well there is a first peak achieved at a higher frequency than before, followed by a rapid drop in the ASD of the response and several smaller local maxima.

The difference in the peak's frequency may be attributed to the main component of the mode. Each of them is characterized by a shape presenting an X, Y and Z components. The excitation of the system through loads with a certain primary component, whether X, Y or Z, will cause a response in the system leading to the formation of the mode shape presenting the same component as the load as its main one.

As a result, from what can be observed through the above pictures, it is safe to assume that the mode exhibiting the Z as its main component, is characterized by a natural frequency higher than the mode having the Y as the main one.

Another possible explanation for this event can be related to the geometry of the components themselves which, due to their shape, and physical properties appear to be responsive at lower frequencies in the lateral configuration.

The study of the analyses responses leave only the test-pod to be discussed even if it's already possible to suppose the type of response it would present.
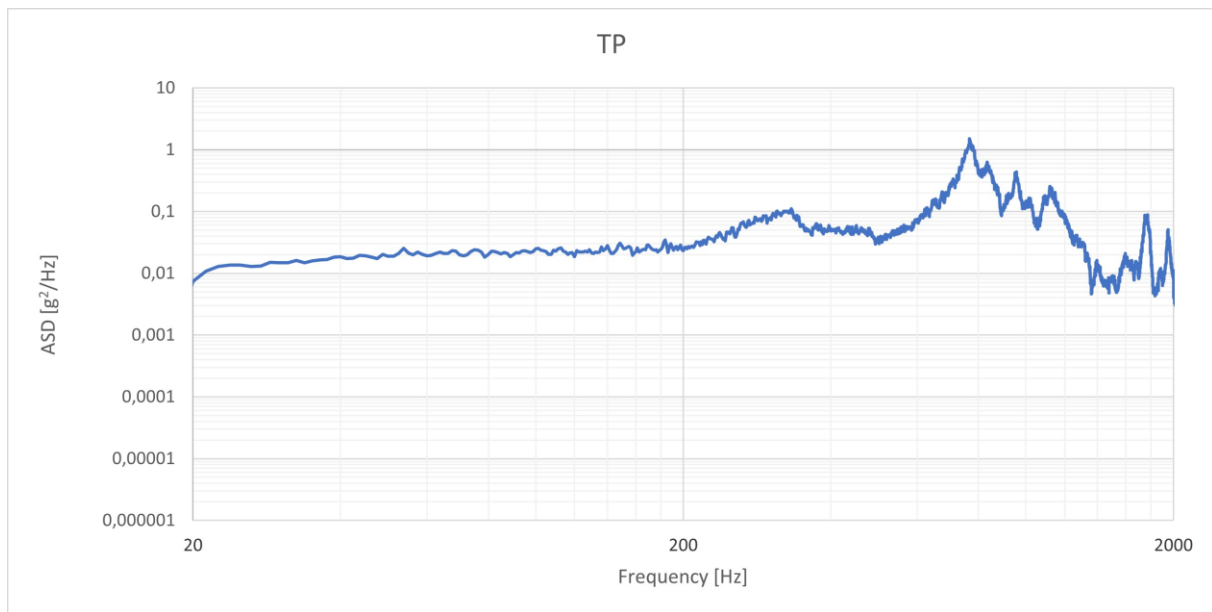
Figure 5.30 TP random longitudinal vibrations results

As it was possible to image, the response happened to be qualitatively similar to the one encountered in the previous tests set. In fact, the test-pod presents a response different from the rest of the system, for the same reasons previously described.

The evaluation of the ASD leaves only to determine whether the system has been subject to changes or not through the sine sweep test.

5.4.2.2 Sine sweep tests
As in the previous section, the data collected are divided by the accelerometer which gathered them and compared between the "before random" and "after random" sets.
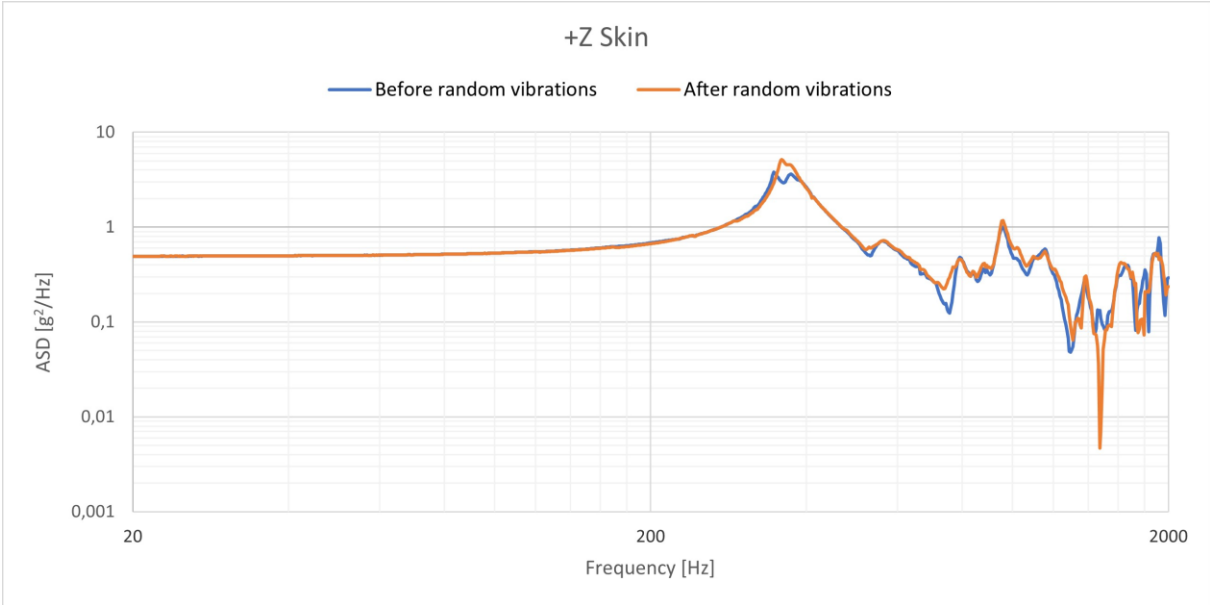
Figure 5.31 +Z skin longitudinal sine sweep comparison
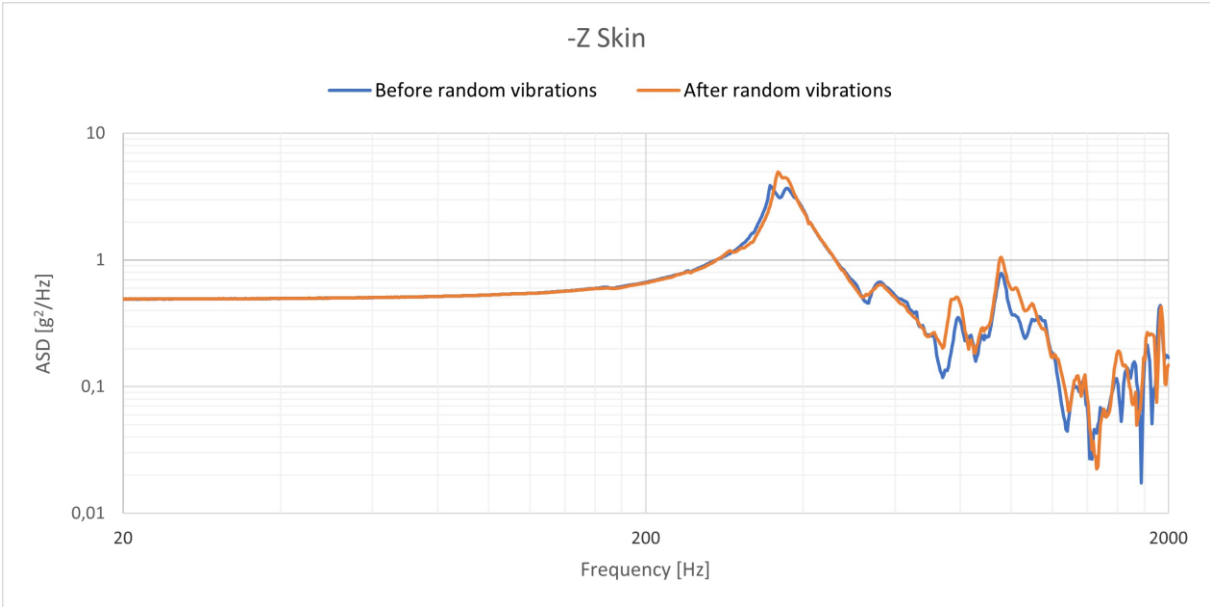
Figure 5.32 -Z skin longitudinal sine sweep comparison
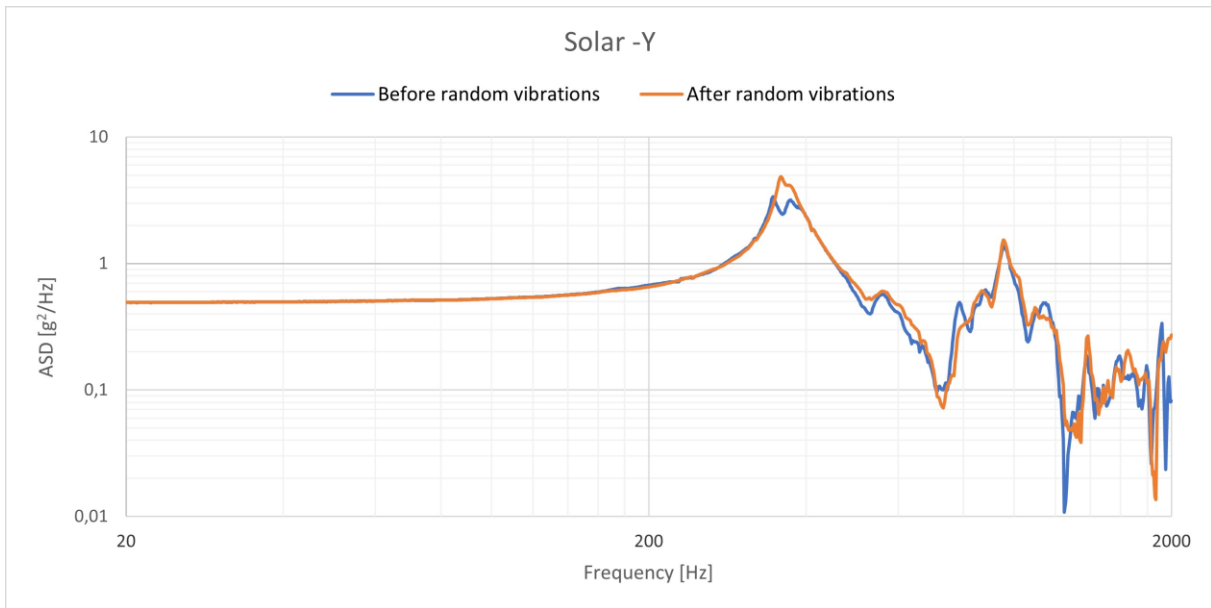
Figure 5.33 Solar -Y longitudinal sine sweep comparison
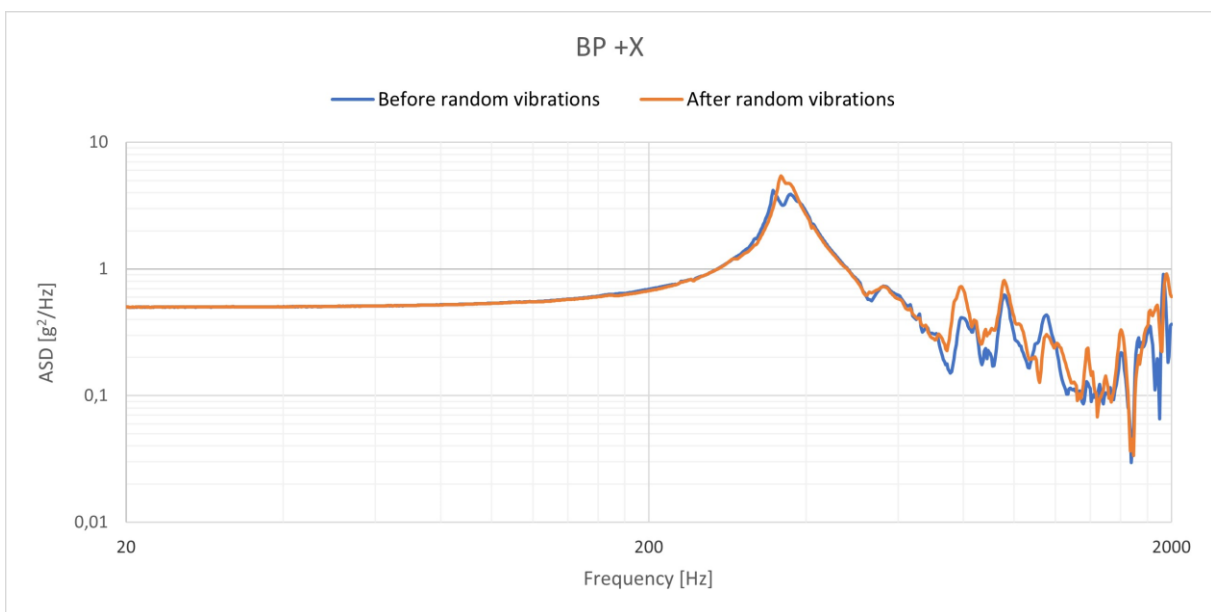
Figure 5.34 BP +X longitudinal sine sweep comparison

The results obtained from the longitudinal sine sweep tests are particularly relevant as there is almost no difference between the one conducted before the random vibrations tests and the one performed after them, unlike what has been observed during the lateral configuration vibration test.

This was to be expected as the new test configuration excited the spacecraft along its longitudinal axis, which presented much less freedom than the lateral one. As a matter of fact, it was possible to regulate the fixtures using the adjustable pins of the top plate. On the other hand, as mentioned in 5.1, between the spacecraft and the test-pod's rails there was a small

clearance which was filled as well as possible using the Kapton, clearly not fully due to the small fluctuations observed with the lateral sine sweep comparison.
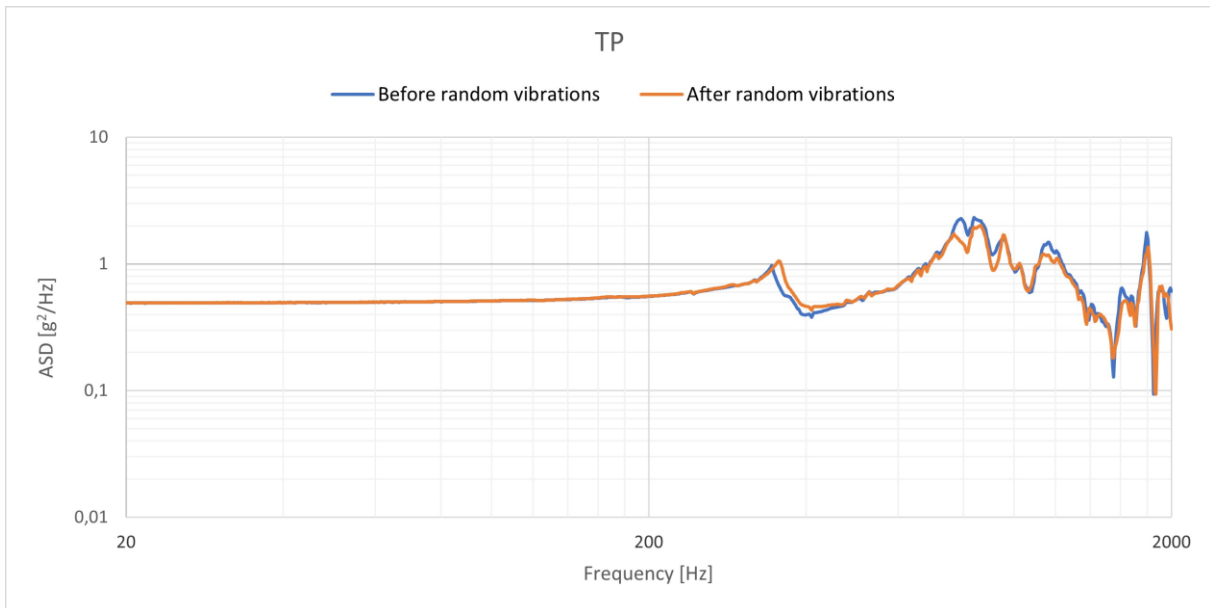
Figure 5.35 TP longitudinal sine sweep comparison

As in the previous set of tests, performed in the lateral vibration environment, the test-pod presents the most consistent data, with only minor fluctuations between the two outputs. Moreover, in this case as well, it's possible to observe the differences in the response from the rest of the system due to the different properties of the body.

All in all, the results collected allow to determine that there hasn't been any change within the spacecraft, at least not on a measurable scale through the sine sweep test. All in all, the functional test conducted after the vibration ones confirmed the health status of the spacecraft.

5.4.2.3 FEA and vibration test comparison

As in the previous test, for this one as well it's possible to assess the correctness of the FEA through the evaluation of the acceleration response RMS registered during the vibration test.

Component	FEA RMS	Test RMS
$+X$ solar panel	15.85	13.70
$-Y$ solar panel	16.17	11.54
$-Z$ CommSys board support	23.97	11.86
$+Z$ CommSys board	7.246	12.72

Table 5.6 Longitudinal case acceleration response RMS comparison

As in can be seen from Table 5.6, the RMS values tend to be more similar between each other than what has been observed in the previous test. Obviously, the main FEA RMS presents values generally greater than the one registered during the test. However, this is not the case for the $+Z$ CommSys board as the acceleration response is lower in the digital model. The reason for this is probably because of the resulting stiffness in the Z direction is lower than the

one in the physical model. As a matter of fact, a component missing in the Finite Element Model is the CommSys radio which was supposed to be connected to the board and the aluminium support, further stiffening the subsystem and leading to a higher RMS.

All in all in this case as well the results are successful as they do not differ excessively between the two models.

6   Design assessment

The effectiveness of the internal configuration chosen can be proven through several points. The most relevant ones being the AIV&T activities and the data collected in-orbit.

6.1   AIV&T activities

A major part of the project has been covered by the AIV&T activities and in the matter of this thesis it was deemed appropriate to cover an event regarding such topic as to highlight the effectiveness of the design choices.

The case to be studied involves the replacement of the sensing suite in the spacecraft completely assembled and integrated due to a short circuit which caused the impairment of the board. The event occurred during one of the last flashes of the on-board software. In particular, the sensing suite was being monitored before it was turned off to proceed with the maintenance. However, after the reboot, the operators noticed irregularities in the board activity as shown in the figure below. This led to further investigation which brought to light the short circuit of the board.

```
<initTasks> Current RTC timestamp: 3155766773 , Date: 2070-01-01, 01:52:53
<memoryTask_function> Current MRAM table:
<memoryTask_function>---------------------------------
<memoryTask_function> Packet counter:        1484
<memoryTask_function> Memory error counter: 0
<memoryTask_function> Reboot counter:        22
<memoryTask_function>---------------------------------
<sensorsTask_function> IMU correctly configured
<parrotTask_function> Received timestamp from cdh 1 : 6778 Date: 2070-01-01, 01:52:58
<parrotTask_function> Timestamp updated
<parrotTask_function> Requested telemetry from 9a9a with id c770
<memoryTask_function> Reading single packet telemetry for cdh 1
<parrotTask_function> Sending last packet, current singer packet counter 1484
<sensorsTask_function> New sample triggered
<sensorsTask_function> Timestamp: 3155766784 Date: 2070-01-01, 01:53:04
<sensorsTask_function> received IMU packet
<sensorsTask_function> all ADC channel sampled
<sensorsTask_function> Parrot sensors acquired
<sensorsTask_function> Sampling completed, write requested
<memoryTask_function> Written packet 1484
```

Figure 6.1 Sensing suite normal output

```
a5 26 ab 4ya ab a1 ab 15
a9 29 ac de a9 99 a4 77
aa ab ab 37 ac 3b ab 6a
ac e8 aa 68 ac 60 4b 10
4b cc 0a cc 0a 00 02 e0
3f

<encodeDataByteStuff> message encoded, length 115
<sendSerMsg> sending message ID 20912 on serial interface
à ̧ ͬ ūñ ! þ ̀ ày( àǔ ̧ ͬ (àà|à(ū
```

Figure 6.2 Sensing suite error output

Moreover, there was a time issue as well because of the fact that the board suffered this

damage just a week before the vibration tests, thus it was necessary to change the board and perform all the functional tests to assess the correctness of the operation performed.

One of the major issues, besides the short time available, was the presence of Epoxy Adhesive 2216 on every single screw, placed to prevent them from losing, as well as on every couple of connectors male-female to keep them fixed together. The latter was a particularly critical matter as the sensing suite had 7 different connectors, 2 of which were critical for the correct functioning of the board as they allowed the board to interface with the backplane.
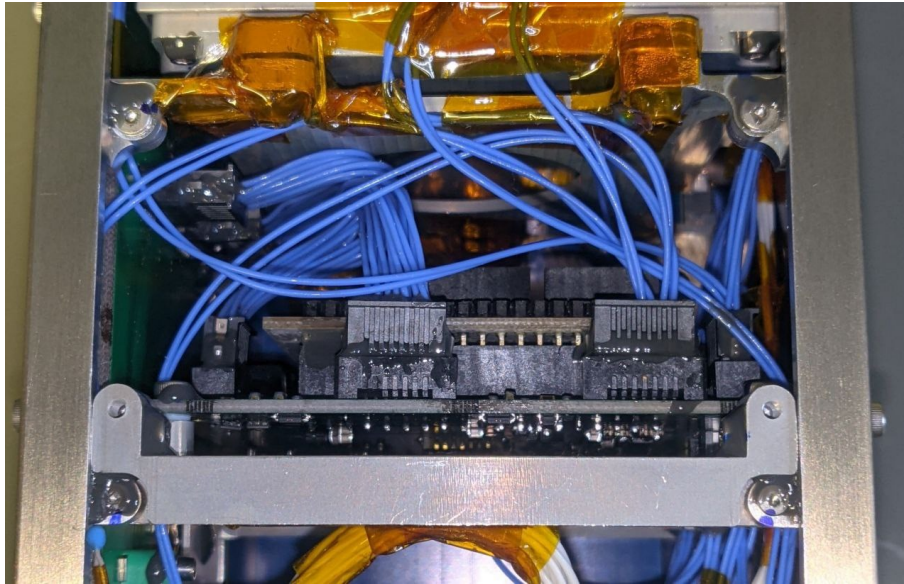

Figure 6.3 The sensing suite fully integrated

To proceed with the replacement it was decided to firstly remove the solar panels located on the $\pm Y$ faces, to obtain a clear view of the interior of the spacecraft. This was done by carefully removing the adhesive on the external screws using IPA as it's a solvent of this type of glue. Obviously, since some time had passed from the application of it, every single screw required several minutes as to avoid damages to the solar panels. Moreover, a critical aspect was the presence of the power cable, used to connect the panels with the backplane. These were fixed together using the epoxy adhesive; therefore it was necessary to remove all of it using a very small clearance. In fact, to prevent excessive cables vibrations, these were fixed in several points preventing them to move too freely. In this case as well it was necessary to proceed with the softening of the glue and to later extract the connectors without damaging them.

The access to the interior of the spacecraft allowed to proceed with the rest of the sensing suite removal procedure. Due to the nature of the connectors it was impossible to detach the two connectors by dissolving the epoxy adhesive using the IPA. In fact, there were several clearances between the two of them, which caused the glue to flow in these spaces making it impossible to dissolve it.
Therefore, after a careful assessment of the situation, it was decided to mechanically remove the connectors from the PCB itself and to later extract the males connectors from the females by carefully dismantling the latter while softening as much as possible the epoxy adhesive using the IPA.

The removal of the connectors left only the screws to take out. The procedure followed was the same as for those located on the solar panels, with the cleaning of the glue and the loosening of the screws.

Finally, it was possible to extract the board by making it pass in the window shown in Figure 6.3, without having to disassemble any component.

The procedure followed to integrate the new sensing suite starts with the connection of the connectors to the new board. After a careful examination of the board and the whole system through a series of functional tests, it was deemed to be ready to be assembled again. Therefore it proceeded with the tightening of the screws and the application of the Epoxy Adhesive as to maintain the final system identical to the one before the replacement activity.

After the reintegration of the solar panels through the connection of the dedicated power cables and their assembly, the glue was applied again, ending the replacement activity.

6.2 In-orbit data

The spacecraft, operates in a radio-amateur frequency, transmitting packets containing the phrases stored in the on-board memory, as well as telemetry data, every two minutes. Moreover, it's possible to send requests of transmission of bigger dataset, stored inside the sensing suite, through the utilization of a specific command. This functionality is named "beacon" and it has proven to be particularly useful as it allowed to obtain multiple data from a wide timeframe transmitting everything during a single passage. In this specific case, the packets collected allowed to represent the trend of the temperatures during the 18th of July.

The operation activities have been generally conducted using the radio-amateur station of BRA, managed the local section of ARI.

Figure 6.4 ARI.-Bra radio-station

Among the several data, the collection of temperature data through the set of thermistors place all around the spacecraft allows to determine the quality of the choices made regarding the thermal aspects, in particular the transmission of heat by conduction between the C&DH and the battery pack and the successful creation of a heat bubble, insulating the three components from the rest of the system.

Keeping in account Table 3.13, the thermistors that are going to be used in this evaluation are:

- Thermistor 14, located on the C&DH 1's cross-member
- Thermistor 15, located on the C&DH 1's case
- Thermistor 16, located on the battery pack stiffener
- Thermistor 17, located on the C&DH 2's case
- Thermistor 18, located on the C&DH 2's cross-member

Moreover, it's possible to include measures taken by the sensors placed directly on the C&DH boards and on the battery pack. In particular, the latter is the most important as it allows to evaluate the battery pack temperature and to compare it with the one of the stiffener, evaluating the quality of the insulation method.

Starting from the temperatures of the structural elements, the temperatures registered are depicted in the following pictures.
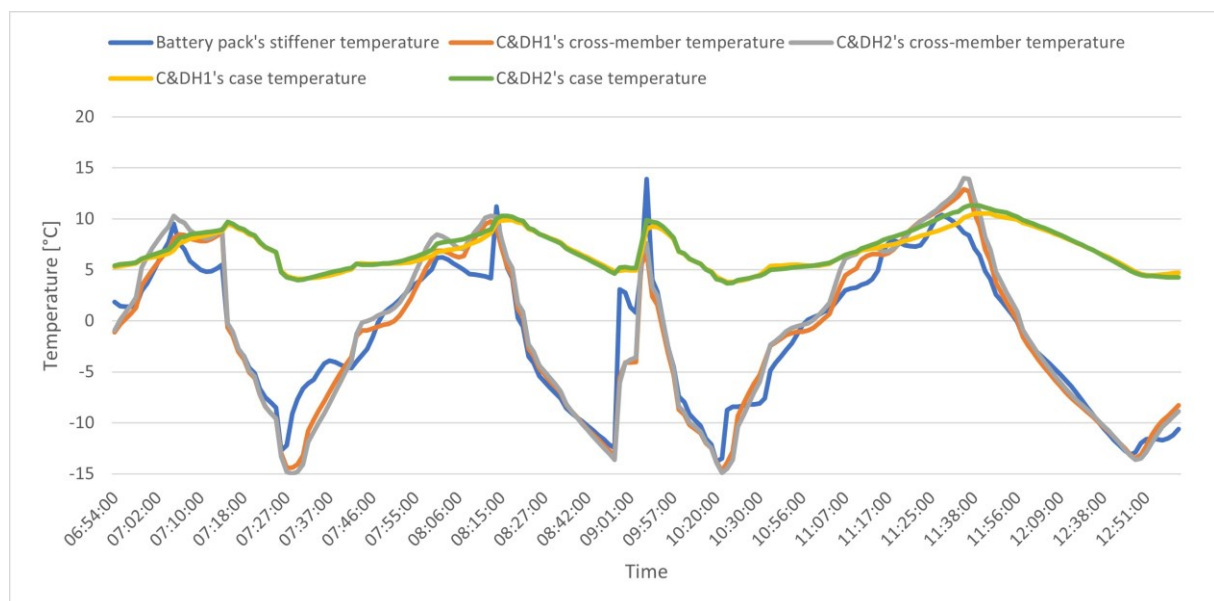
Figure 6.5 Structural elements temperatures

As it can be seen from Figure 6.5, the battery pack's stiffeners and the C&DH's cross-members present the same temperature trend, reaching values below the -10°C. On the other hand, the C&DHs' cases tend to remain within the range of 5-10°C, without particularly swift fluctuations. This can be attributed to the thermal insulation system, designed and described in 3.5.2 and 3.5.3, which prevents heat transfers from the warmer components to the rest of the structure.

At this point it's useful to evaluate the status of the battery pack and the C&DHs themselves, assessing effectiveness in generating the desired "heat bubble".
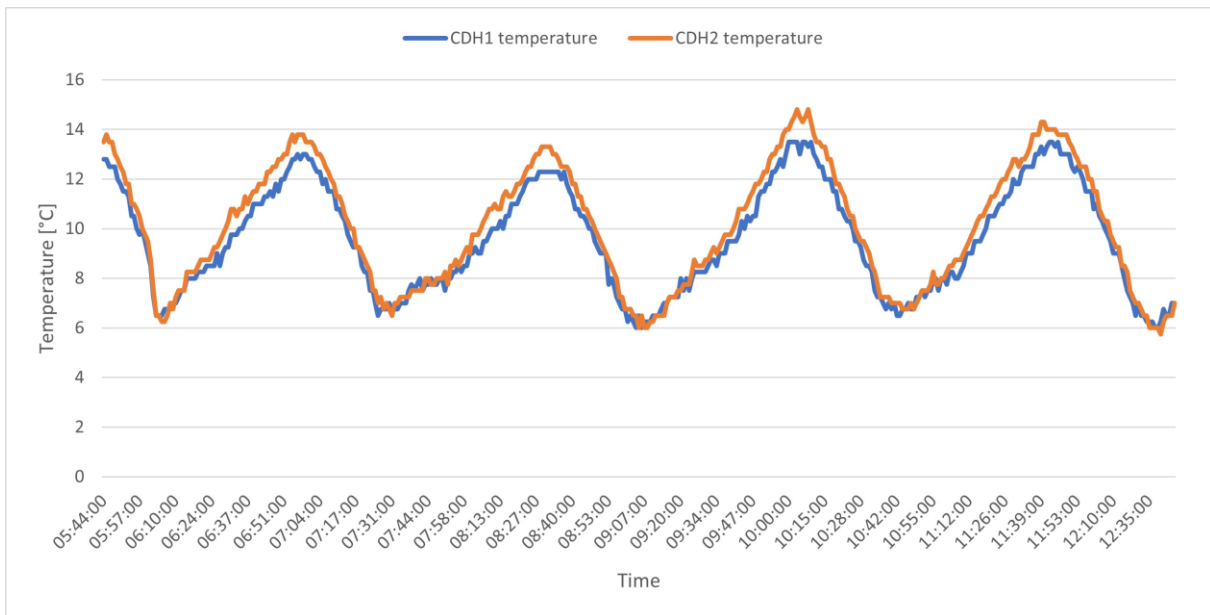
Figure 6.6 C&DHs temperatures
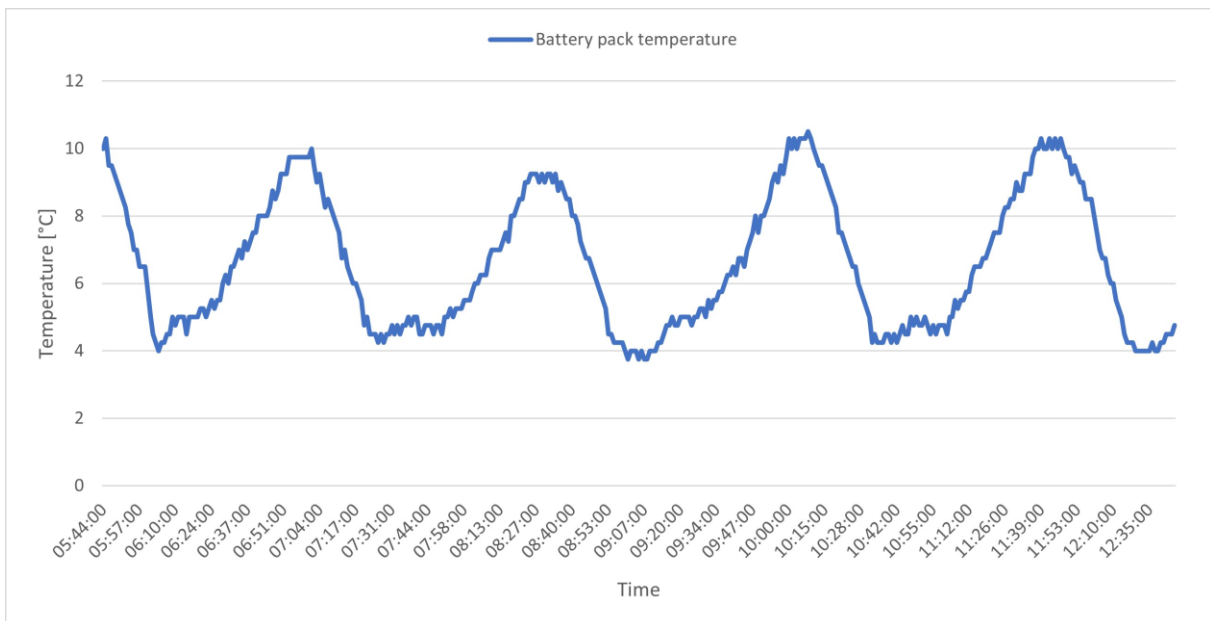
Figure 6.7 Battery pack temperature

Starting with the C&DHs, Figure 6.6 allows to observe the fluctuations of the boards temperature, which is kept between 6°C and 12°C, much higher than those registered on the cross-members, as to further support the system devised to insulate the components.

Moreover the battery, whose trend is shown in Figure 6.7, presents temperatures characterized by a lower and upper limit well defined, 4°C and 10°C. Such information allows

145

to assess the health status of the component as it was design to operate at a temperature within the range of 5°C, without falling to the critically low temperature of the stiffeners supporting the pack, which reaches even -15°C. Furthermore, this allows to evaluate the behaviour of the thermal conduction performed by the thermal pads, placed between the C&DHs' case and the battery pack, as to maintain the latter at a higher temperature without the need for the heathers to activate consuming more energy.

To sum up, the data collected during the several passages of the spacecraft allowed to assess its health status which appears to be optimal. Among the several solutions implemented to reach such result the thermal insulation and conduction system certainly covered a major role, allowing the components to operate in the best environment possible, without the risk of degradation.

7 Conclusions

This thesis provided an overview of the path followed to develop in an extraordinary short period of time part of the spacecraft for the Spei Satelles space mission.

Initially a description of the design drivers and the requirements was given, allowing to determine what the spacecraft, in particular the structural subsystem, and its internal configuration were expected to achieve.

Later, the design phase was presented providing the results of three different iterations through the *Solidworks* environment. Several design steps were not discussed as they only provided minor changes to the structure and/or configuration, thus deemed less relevant and kept aside to focus on the most impactful iterations. Moreover, the description of the problems faced alongside the design phase allowed to better justify the choices taken.

With the FEA it was possible to validate the model realized, making it acceptable to passing to the production phase through its procurement. Such analyses were conducted using multiple software in order to maximize the efficiency by getting the best out each of them. First the CAD model was exported in an acceptable format to be used as the base for the analyses, then *MSC Apex* was deemed to be the best one for the pre-processing modelling of some FEM elements, while *MSC Patran* allowed a better setting of the problem. All to proceed with the resolution through *MSC Nastran* and the results discussion through *MSC Patran*.

The environmental tests, specifically the vibrational ones, reproduced the launch conditions through a shaker, allowing the characterization of the spacecraft response to the launch environment. Such tests were deemed to be the most critical ones, as they marked the end of the assembly and integration phases, making it possible to proceed only with the final functional tests. The response were within the expectations, with only slight variations due to the rattling, which was promptly identified.

Finally, an assessment of the design was conducted presenting an AIV&T activity and some in-orbit data collected by the sensing suite. The former supported the modularization of the spacecraft, verifying several requirements. The latter was used to verify the effectiveness of the insulation system devised and implemented on-board. In particular, the temperatures of several thermistors and sensors were presented which allowed to determine the thermic behaviour of the spacecraft, specifically the conductivity of its components, dampened or strengthened.

Bibliography

[1]   California Polytechnic State University, *CubeSat Design Specification (REV 14.1),* San Luis Obispo, CA., 2022.

[2]   T. Villela, C. A. Costa, A. M. Brandão, F. T. Bueno and R. Leonardi, *Towards the Thousandth CubeSat: A Statistical Overview,* 2019.

[3]   R. Walker, "Technology CubeSats," [Online]. Available: https://www.esa.int/Enabling_Support/Space_Engineering_Technology/Technology_CubeSats.

[4]   "Technique; Nano-book," 2023. [Online]. Available: https://www.speisatelles.org/en/site/tecnica.

[5]   S. Bollattino, *Development of a versatile on board computer for small satellites,* 2023.

[6]   S. Corpino, S. Chiesa, F. Stesina and N. Viola, "CubeSats development at Politecnico di Torino: The e-st@r program," in *61st International Astronautical Congress*, 2010.

[7]   S. Corpino and F. Stesina, "In orbit operations of an educational CubeSat: The e-st@r-II experience," *International Review of Aerospace Engineering,* vol. 13, pp. 40-50, 2020.

[8]   J. Frudiger and S. Gunnink, "Redefining the CubeSat, a structure for mass production," *Jec Composites Magazine,* pp. 50-51, June 2019.

[9]   Hexagon AB, *MSC Nastran 2022.4 Reference Guide,* 2022.

[10]   Arianespace, *Vega's User Manual Issue 4 Revision 0,* 2014.

[11]   Hexagon AB, *MSC Nastran 2022.4 Linear Static Analysis User's Guide,* 2022.

[12]   A. Pagani, *Strutture Spaziali,* 2022.

[13]   ESA, "Requirements and Standard," [Online]. Available: https://www.esa.int/Enabling_Support/Space_Engineering_Technology/Requirements_and_standards.

[14]   Astrofein, *Interface Control Document Pico-Satellite Launcher Pack (PSL12U).*

[15]   "Spacematb database," [Online]. Available: https://www.spacematdb.com/spacemat/.

[16]   SpaceX, *Rideshare Payload User's Guide,* 2022.

[17]   D-Orbit, *IRD_Annex 4.*

[18]   ESA Requirements and Standards Division, *ECSS System, Glossary of terms,* 2012.

[19]   F. Lucia, *Development of a tool for thermal analysis of small spacecrafts,* 2023.

[20] D. Cosenza, *Development of a Tool for the Design and Verification of Thermal Control Systems of Small Sats,* 2023.

[21] ESA, *ECSS-Q-ST-70-02C, Space Product Assurance, Thermal vacuum outgassing test for the screening of space materials,* 2008.

[22] U.S. Deparment of Defense, *Military Specifications - Anodic coatings for aluminum and aluminum alloys.*